UNIVERSITÀ DELLA CALABRIA

Dipartimento di Fisica

Dottorato di Ricerca in
Scienze e Tecnologie Fisiche, Chimiche e dei Materiali
in convenzione con il CNR

CICLO XXXIII

STUDY OF PHYSICAL, MECHANICAL AND TRANSPORT PROPERTIES OF POLYMERIC MEMBRANES FOR GAS SEPARATION

Settore Scientifico Disciplinare CHIM/05 Scienza e Tecnologia Dei Materiali Polimerici

Coordinatore: Ch.ma Prof. ssa Gabriella Cipparrone

Firma _ Firma oscurata in base alle linee guida del Garante della privacy .

Supervisori: Dott.ssa Lidietta Giorno, Dott. Johannes Carolus Jansen

Firma_ Firma oscurata in base alle linee guida del Garante della privacy

Firma__ Firma oscurata in base alle linee guida del Garante della privacy

Dottoranda: Dott.ssa Mariagiulia Longo

Firma_ Firma oscurata in base alle linee guida del Garante della privacy .

Alla mia famiglia

Contents

List of figures

Contents

List of tables

Abstract Italiano

La separazione di miscele di gas e vapori è il processo centrale di molte applicazioni industriali, come la separazione di metano da biogas o il recupero della CO_2 da fumi di combustione, operazione molto importante per poter arginare il surriscaldamento globale.[1–3] Numerosi gruppi di ricerca, tra cui l'Istituto per la Tecnologia delle Membrane del CNR, presso cui è stato svolto questo lavoro di tesi, si impegnano nel campo della separazione di miscele gassose mediante tecnologie a membrana. Ed è proprio in questo contesto che si innesta il lavoro svolto durante questo dottorato di ricerca, perseguendo l'obiettivo di creare e caratterizzare membrane polimeriche con le giuste proprietà di trasporto per essere efficaci nella separazione di gas, nonché di studiare le proprietà meccaniche, al fine di comprendere meglio le correlazioni struttura-proprietà-prestazione di un polimero.

Tradizionalmente le proprietà meccaniche sono investigate mediante prove di trazione o caratterizzazione reologica.[4] Tuttavia, queste tecniche necessitano di campioni di grandi dimensioni, di cui non sempre si ha disponibilità. Per piccoli campioni o quando è necessaria un'analisi locale del modulo elastico di Young, un'alternativa versatile e ampiamente utilizzata è la spettroscopia di forza.[5] La spettroscopia di forza permette di ottenere analisi quantitative e qualitative, su diverse scale di grandezza, delle proprietà meccaniche e viscoelastiche di campioni che altrimenti non potrebbero essere testate come nel caso di polimeri di nuova sintesi.

Negli anni, particolare attenzione è stata concentrata sulle membrane polimeriche a matrice mista (*MMMs*), in cui un additivo o *filler* viene addizionato alla matrice polimerica.[6,7]

[1] D.S. Sholl, R.P. Lively, Seven chemical separations to change the world, Nature. 532 (2016) 435–437. https://doi.org/10.1038/532435a.

[2] R.W. Baker et al., 50th Anniversary Perspective : Polymers and Mixed Matrix Membranes for Gas and Vapor Separation: A Review and Prospective Opportunities, Macromolecules. 50 (2017) 7809–7843. https://doi.org/10.1021/acs.macromol.7b01718.

[3] E. Esposito et al., Simultaneous production of biomethane and food grade CO2 from biogas: An industrial case study, Energy Environ. Sci. 12 (2019) 281–289. https://doi.org/10.1039/

[4] Z. Sedláková et al., Pebax®/PAN hollow fiber membranes for CO2/CH4 separation, Chem. Eng. Process. - Process Intensif. 94 (2015) 53–61. https://doi.org/10.1016/j.cep.2015.03.016.

[5] M. Longo et al, Force spectroscopy determination of Young's modulus in mixed matrix membranes, Polymer (Guildf). 156 (2018) 22–29. https://doi.org/10.1016/J.POLYMER.2018.09.043.

[6] R.D. Noble, Perspectives on mixed matrix membranes, J. Memb. Sci. 378 (2011) 393–397. https://doi.org/10.1016/j.memsci.2011.05.031.

[7] M. VinobaM et al., Recent progress of fillers in mixed matrix membranes for CO2 separation: A review, Sep. Purif. Technol. 188 (2017) 431–450. https://doi.org/10.1016/j.seppur.2017.07.051.

Generalmente, l'idea è quella di combinare la buona lavorabilità e la stabilità meccanica del polimero, con le proprietà di trasporto dei *filler*, come nel caso dei liquidi ionici (*Ionic Liquids*).[8–10] I liquidi ionici sono sali che si presentano allo stato liquido a temperatura ambiente, non sono infiammabili ed hanno tensioni di vapore molto basse, difficili da misurare. I liquidi ionici sono utilizzati nella separazione dei gas poiché generalmente interagiscono con la CO_2 mostrando un'elevata solubilità.[11] Inoltre, la possibilità di combinare un elevato numero di anioni e cationi rende questi materiali attrattivi per innumerevoli scopi.[12] Accanto alla preparazione di *MMMs* un incentivo all'uso della tecnologia a membrana è quello di sviluppare nuovi materiali aventi una migliore permeabilità (produttività) e selettività (purezza dei prodotti) rispetto ai materiali esistenti.[13] Per ottenere una migliore permeabilità e selettività, la sintesi di nuovi polimeri, come suggerito da Freeman *et al.*, deve mirare ad un aumento simultaneo della rigidità e della separazione tra le catene.[14] Questa strategia di progettazione, utilizzata nella sintesi dei polimeri a microporosità intrinseca (*PIM*), ha permesso lo sviluppo di polimeri aventi un'elevata permeabilità, un buon fattore di separazione e delle ottime proprietà meccaniche.[15,16] Negli ultimi decenni sono stati sintetizzati numerosi nuovi polimeri. Tuttavia, molti studi sono limitati ad una singola coppia di gas.[17,18] Sarebbe, dunque, vantaggioso poter eseguire uno screening rapido delle proprietà di trasporto di polimeri, per valutarne a pieno il potenziale riducendo i tempi necessari ai test sperimentali. Metodi di apprendimento automatico (*Machine Learning* model) sono stati

[8]   S. Meshkat at al., Mixed matrix membranes based on amine and non-amine MIL-53(Al) in Pebax® MH-1657 for CO2separation, Sep. Purif. Technol. 200 (2018) 177–190. https://doi.org/10.1016/j.seppur.2018.02.038.

[9]   A. Bandyopadhyay, Amine versus ammonia absorption of CO2 as a measure of reducing ghg emission: A critical analysis, Carbon Capture Storage CO2 Manag. Technol. (2014) 1–54. https://doi.org/10.1201/b16845.

[10] Z. Dai et al. Combination of ionic liquids with membrane technology: A new approach for CO2 separation, J. Memb. Sci. 497 (2016) 1–20. https://doi.org/10.1016/j.memsci.2015.08.060.

[11] P. Bernardo et al., G. Clarizia, Gas transport properties of Pebax®/room temperature ionic liquid gel membranes, Sep. Purif. Technol. 97 (2012) 73–82. https://doi.org/10.1016/J.SEPPUR.2012.02.041.

[12] M. Kohoutová et al., Influence of ionic liquid content on properties of dense polymer membranes, Eur. Polym. J. 45 (2009) 813–819. https://doi.org/10.1016/j.eurpolymj.2008.11.043.

[13] R.W. Baker, B.T. Low, Gas separation membrane materials: A perspective, Macromolecules. 47 (2014) 6999–7013. https://doi.org/10.1021/ma501488s.

[14] B.D. Freeman, Basis of permeability/selectivity tradeoff relations in polymeric gas separation membranes, Macromolecules. 32 (1999) 375–380. https://doi.org/10.1021/ma9814548.

[15] P.M. Budd et al., Polymers of intrinsic microporosity (PIMs): robust, solution-processable, organic nanoporous materials, Chem. Commun. 4 (2004) 230–231. https://doi.org/10.1039/b311764b.

[16] C. Ma, J.J. Urban, Polymers of Intrinsic Microporosity (PIMs) Gas Separation Membranes: A mini Review, Proc. Nat. Res. Soc. 2 (2018). https://doi.org/10.11605/j.pnrs.201802002.

[17] Z.P. Smith et al., Influence of Diffusivity and Sorption on Helium and Hydrogen Separations in Hydrocarbon, Silicon, and Fluorocarbon-Based Polymers, Macromolecules. 47 (2014) 3170–3184. https://doi.org/10.1021/ma402521h.

[18] J. Duan et al., High CO2/N2/O2/CO separation in a chemically robust porous coordination polymer with low binding energy, Chem. Sci. 5 (2014) 660–666. https://doi.org/10.1039/C3SC52177J.

sviluppati e applicati alle membrane polimeriche per la previsione di parametri di trasporto di gas sconosciuti sulla base di dati noti.

Il lavoro in questa tesi è suddiviso nei seguenti temi principali:

Dopo un'introduzione degli aspetti teorici e delle membrane in generale, la prima parte è dedicata alla spettroscopia di forza. Sono state confrontate le misurazioni del modulo di Young ottenute su scala macroscopica, mediante prove di trazione con quelle ottenute su scale nano e micrometriche mediante spettroscopia di forza. Le misurazioni sono state eseguite su membrane del puro copolimero di *Pebax®1657* e su *MMMs* di *Pebax®1657* additivate con liquido ionico 1-butil-3-metilimidazolio tetrafluoroborato, [*BMIM*][*BF₄*]. L'analisi AFM su scala nanometrica ha consentito la determinazione del modulo dei singoli domini del copolimero, mentre l'analisi su scala micrometrica ha permesso di ottenere valori medi dell'intero polimero. Ciò offre buone prospettive per le future analisi buone prospettive per l'analisi di campioni in cui non è possibile utilizzare i test di trazione tradizionali.

La seconda parte è incentrata sull'analisi delle proprietà di trasporto in PIM ultrapermeabili e la loro correlazione con il modulo di Young. Le proprietà di trasporto di *PIM-TMN-Trip* e *PIM-BTri*p sono state analizzate in funzione di un intervallo di temperatura da 25 °C a 55 °C. Ciò ha evidenziato come queste siano influenzate dalla temperatura e dalla dimensione del gas penetrante.[19] Il lavoro si è poi concentrato sulle correlazioni trasporto-modulo di Young, durante l'invecchiamento fisico (*aging*) delle membrane. Come tutti i polimeri vetrosi ad alto volume libero, i *PIM* soffrono di *aging*, che porta ad un lento rilassamento ed al riarrangiamento della struttura molecolare in funzione del tempo.[20] L'eccellente accordo del modulo di Young misurato per il *PIM-1*, il primo PIM ad essere sintetizzato, con i valori ottenuti da altre tecniche in letteratura, ha confermato l'idoneità della spettroscopia di forza *AF*M per la rapida valutazione delle proprietà meccaniche. I risultati di diversi polimeri, tra cui il *PIM-2* e cinque *PIM* ultrapermeabili, hanno fornito la prova

[19] A. Fuoco et al., Temperature Dependence of Gas Permeation and Diffusion in Triptycene-Based Ultrapermeable Polymers of Intrinsic Microporosity, ACS Appl. Mater. Interfaces. 10 (2018) 36475–36482. https://doi.org/10.1021/acsami.8b13634.
[20] CH. Lau et al., Ending aging in super glassy polymer membranes, Angew. Chemie - Int. Ed. 53 (2014) 5322–5326. https://doi.org/10.1002/anie.201402234.

diretta che la selettività sulla base delle dimensioni molecolari dei gas penetranti è fortemente correlata al modulo di Young.[21]

Ulteriori ricerche si sono concentrate sullo studio delle proprietà meccaniche dei copolimeri con l'archetipo PIM-1 e due nuovi, ed inediti *PIM: PIM-DBzMP* e P*IM-SBI-Trip*. Per entrambi i copolimeri sono stati valutati i moduli di Young in considerazione al diverso rapporto tra i monomeri e l'effetto dell'invecchiamento fisico. Inoltre, sono state studiate le proprietà di trasporto in miscele polimeriche. Il vantaggio della miscelazione risiede nella possibilità di ottenere materiali con specifiche proprietà mediante il mescolamento di polimeri diversi, in questo caso un polimero vetroso commerciale *Matrimid®5218* e l'*AO-PIM-1*.

In fine, l'ultima parte è dedicata al *Machine Learning* e allo sviluppo di un database in cui sono state riportate le strutture, i dati di trasporto, i dati delle proprietà meccaniche e fisiche di ~ 300 *PIM* risultati di 67 strutture diverse. Il set di dati è stato ampliato utilizzando il *Gas Separation Membrane Database della Membrane Society of Australasia* (*MSA*) che raccoglie permeabilità di diversi gas per un grande numero di polimeri pubblicati in letteratura, ed è stato utilizzato per la previsione computazionale dei valori mancanti di permeabilità a partire dai dati sperimentali catalogati per altri polimeri.[22] I dati, stimati mediante modelli di Machine Learning, permetteranno di accelerare l'identificazione di membrane polimeriche performanti.

[21]   M. Longo et al., Correlating Gas Permeability and Young's Modulus during the Physical Aging of Polymers of Intrinsic Microporosity Using Atomic Force Microscopy, Ind. Eng. Chem. Res. 59 (2020) 5381–5391. https://doi.org/10.1021/acs.iecr.9b04881.

[22]   L.M. Thornton et al., Polymer Gas Separation Membrane Database, (2012). https://membrane-australasia.org/msa-activities/polymer-gas-separation-membrane-database/.

Abstract
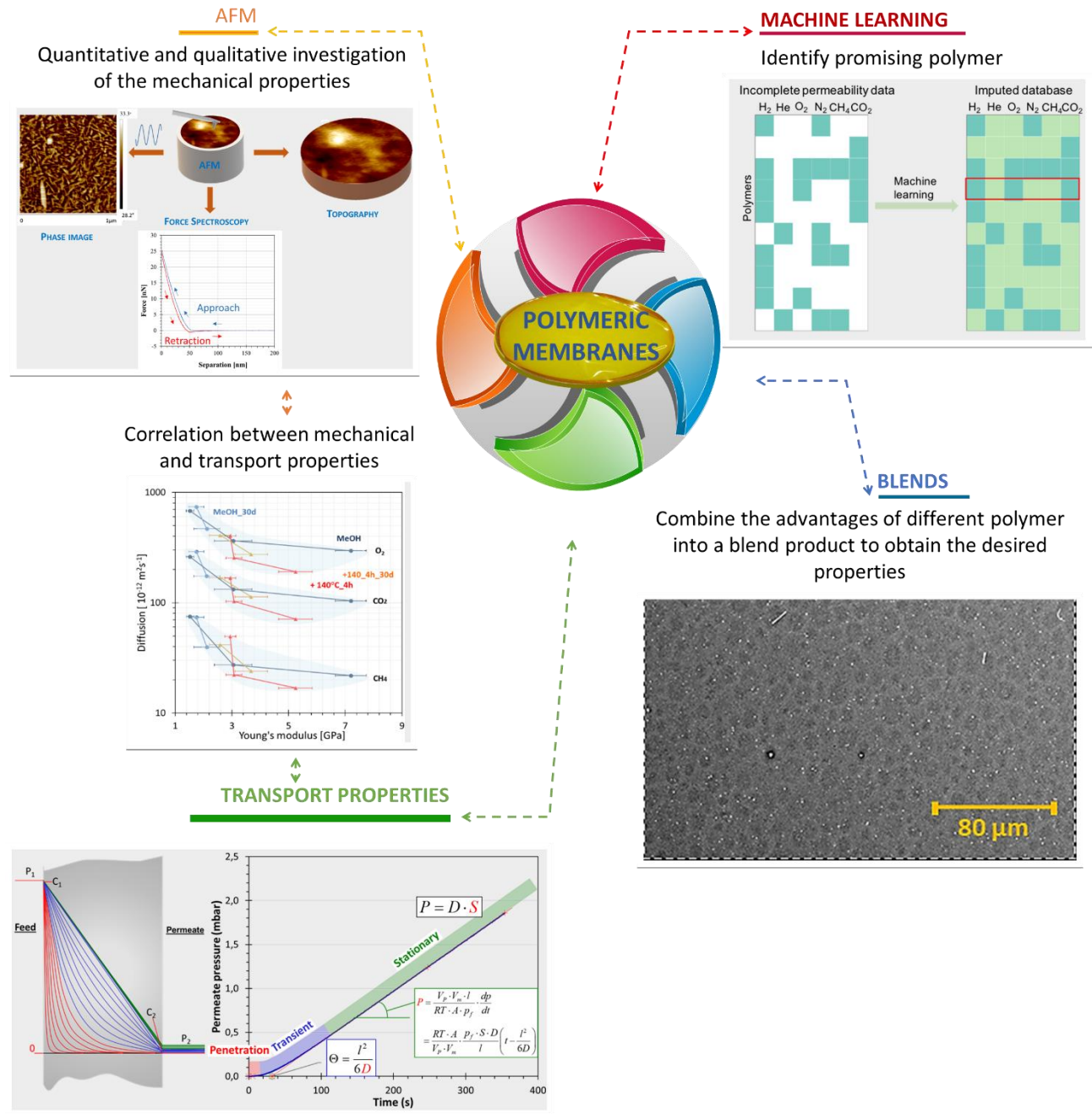
The work in this thesis is organised in different main topics. The first part is devoted to present Atomic Force Microscopy (AFM), carried out in force spectroscopy mode, as a powerful alternative to the more commonly used tensile tests for the analysis of the mechanical properties of polymers, and MMMs in particular. AFM force spectroscopy measurements are carried out with nanometric

and micrometric tips on dense membranes of neat Pebax®1657 and on mixed matrix membranes of Pebax®1657 with different concentrations of an ionic liquid. This offers good perspectives for the analysis of samples where traditional tensile tests cannot be used, for instance composite membranes or particularly small samples.

The second part of the research is focused on the relationship, between the transport properties and Young's modulus for films of polymers of intrinsic microporosity (PIM) and on the effect of physical aging, investigated using pure gas permeability and atomic force microscopy (AFM) measurements in force spectroscopy mode.

In the third part, the transport properties of polymer blend membranes are evaluated.

In the last part, using a computational approach, it is possible to predict missing values for permeability starting with a collection of existing permeability values for other polymers. The data are estimated by means of machine learning models that correlate the behaviour of different gases.

Thus, this thesis is structured as follows:

Chapter 1 and Chapter 2 provide a general introduction on membrane technology and characterization methods used in this thesis, as well as the theoretical background and the description of all experimental techniques used;

Chapter 3 describes the mechanical study on MMMs of blends of Pebax® and the ionic liquid ([BMIM][BF$_4$]);

Chapter 4 describes mechanical and gas transport studies on PIMs;

Chapter 5 presents the gas transport analysis on Matrimid®5218/AO-PIM blend membranes;

Chapter 6 discusses the results of the machine learning model.

Chapter 7 presents the overall conclusions of the work and gives a brief future outlook of possible and desired developments in the field.

Chapter 1

Introduction

The separation and purification of large quantities of chemical products accounts for 10-15% of the world's energy consumption, with the treatment of gas and vapour mixtures being the central process of many industrial applications.[1] The development of membrane technology plays an important role in several large-scale gas separation applications, including CO_2 capture, natural gas treatment and biogas upgrading.[2,3] The key to boost the use of membrane technology in these large-scale applications is the development of novel performing materials with improved permeability (productivity) and selectivity (purity of the products).[13]

1.1 Membrane materials development

The development of novel materials with superior gas transport properties is needed for the successful exploitation of polymer gas separation membrane technology in new markets or for the replacement of traditional technologies.[2] To achieve a higher permeability and selectivity, the synthesis of novel polymers, as suggested by Freeman in his theoretical analysis, has to aim at a simultaneous increase of chain stiffness and interchain separation.[14] This design strategy is consistent with the structure of the first Polymer of Intrinsic Microporosity (PIM-1) in 2004.[15] PIMs demonstrate attractive properties for membranes with a combination of very high permeability, good separation factor, good mechanical properties and capability to be solution-processed.[16] Like all glassy polymers with high fractional free volume, PIMs suffer from physical aging as a consequence of the non-equilibrium nature of their glassy state, leading to a slow relaxation and rearrangement of the molecular structure as a function of time.[20] Aging strongly depends on the previous processing and thermal history of the samples,[23] and widely different treatments are reported in the literature to condition samples before the analysis, which may therefore lead to significant differences in the test results.

Alongside the synthesis of completely new materials, an interesting method to improve the gas separation performance of a material is the preparation of mixed matrix membranes (MMMs), i.e. the incorporation of additives or filler materials in the polymer matrix.[6,7] A widespread idea is to combine the good processability and mechanical stability of the polymer, with the superior gas transport properties of suitable fillers, including ionic liquids (ILs).[8–10] An IL is a salt with melting point below the boiling point of water. Most of them are composed of organic cations and inorganic

anions. Polarity and hydrophilicity/hydrophobicity of ionic liquids can be tuned by suitable combination of the cation and the anion. ILs possess thermal and chemical stability, low vapour pressure and they have a tuneable nature.[12] Their exceptional properties offer interesting perspectives in the field of CO_2 capture, sequestration and utilization, or gas and vapour separation in general. Mass transport in ILs is usually much faster than in polymeric materials, thus allowing higher fluxes through the membrane.[11] High performance membranes must couple superior gas transport properties to mechanical and chemical stability at the working conditions. ILs must therefore be embedded in a suitable porous support, as so-called supported ionic liquid membranes (SILMs), but they can also be covalently bonded to a polymer, or absorbed in a polymer as a gel.[24] Jansen *et al*.[25] have demonstrated that the mechanical properties of IL containing gel membranes may be correlated with their transport properties. As will be discussed later in this thesis, it was shown that a similar relationship also exists between the transport properties and the mechanical properties in PIMs.[21] The analysis of their mechanical properties can be useful for the practical applicability of membranes in industrial modules, because in many processes they are subjected to high pressures. Traditionally these properties are investigated by tensile tests or rheological characterization.[4] However, these techniques require often quite large sample sizes, which are not always available for novel experimental materials. When only small membrane samples are available or when local analysis is necessary, a versatile and widely used alternative is nano-indenting. A second alternative, based on the same principle is force spectroscopy, where the tip of an atomic force microscope (AFM) scans over an area of the sample surface, and the corresponding applied force versus tip displacement (FD curve) is determined.[26,27] FD measurements are macroscopically non-destructive, require millimetre-sized samples and, thus, could potentially allow a large number of tests to be performed even on relatively exotic PIMs where only small samples are available. Atomic Force Microscopy (AFM) allows the quantitative and qualitative investigation of the mechanical properties on different scales,[28–31] besides being a tool for imaging surface topography.[32]

Membranes with high permeability are desired for industrial large-scale industrial gas separation applications. There is a well-known trade-off between gas permeability and the gas selectivity for any gas mixture, with an upper bound for each gas pair quantified by Robeson in 1991 and updated in 2008. [33,34] The PIMs family was used to update the Robeson plots for several gas pairs in 2015 and in 2019. [35,36] These polymers are the most promising candidates for the preparation of the

new generation membranes since their rigidity and physical–chemical requirements leads to highly permselective properties. The Robeson plot provides a good initial screening of the possible membrane performance, although many different aspects determine the real separation performance of a membrane under true operation conditions. The gas pressure can affect the membrane separation performance by saturation of the available sorption sites, plasticization of the polymer, and compression of the membrane or its asymmetric support. The temperature also affects the membrane separation properties: if no phase transition occurs, the solubility decreases with increasing temperature, while the diffusion coefficients increase. The gas composition is of considerable importance, in particular in glassy polymers such as PIMs. These typically exhibit strong competitive sorption of light and heavier gases or vapors, which is responsible for the concentration-dependent permeability of gas mixtures. For the same reasons, the presence of trace impurities can significantly affect the gas transport properties of the membranes, and different contaminants may have various effects on the polymer and/or on the transport properties. In general, water is one of the most common contaminants, which has a negative effect on the separation process for materials like PIMs due to competitive sorption, [37] but may improve selectivity in facilitated transport membranes. A further important aspect is the physical aging that occurs in all glassy polymers. The physical aging involves a reversible polymer chain rearrangement driven toward an unachievable equilibrium state of polymer chain packing. This relaxation of chain conformations leads to densification of the polymer, [23] and generally results in a gradual decrease of the permeability and increase of the (size) selectivity of the polymer.

Numerous new polymers have been reported in Robeson plots over the last few decades. However, since experimental analysis of the transport properties of novel materials can be time consuming, many studies are limited to a single gas pair or to just a few different gases.[17,18] It is likely that there are missed opportunities, where polymers have also promising gas selectivity and permeability for different gas mixtures than those tested. On the other hand, for rapid screening of potentially interesting polymers, it would be advantageous to assess their full potential based on fewer gas permeability measurements. Machine learning (ML) methods have been developed and applied to polymers for predicting properties, including the discovery of novel functional polymers.[38] One of the main models for predicting polymer membrane performance is the group contribution theory, where the chemical structure of a polymer is divided into smaller fragments

and the fragments are used in various ML models as input features.[39–41] An alternative way is to predict the permeability of unknown gases based on data for gases with known permeability.

1.2 Thesis Objective

The main objective of this thesis work is the characterisation of polymeric membranes for gas separation processes and the identification of some of the main parameters affecting their performance. The first goal is to validate AFM force spectroscopy as a possible alternative to tensile tests for the analysis of Young's modulus, even in the case of complex systems such as the blends of an ionic liquid and a multi-block copolymer. The second aim is the investigation of the correlation between the gas transport and structural properties of a series of novel PIMs. This study focuses on how the transport properties depend on the polymer structure and sample history and can be tailored in view of their potential applications. This comprises the blending of a PIM with a commercial glassy polymer in order to reduce costs or obtain properties that are not found in the individual polymers, and aims to study the influence of the blend composition on the membranes transport parameters. The goal of the last part of the thesis is the development of a machine-based learning approach for the prediction of missing gas transport data based on an incomplete set of measurements on existing membranes. This approach is useful with newly designed materials to reduce the investigation time and the cost to determine the transport parameters of a large set of gases.

Membrane technology and characterization methods

The permeability and selectivity are the two most important parameters that define the performance of a gas separation membrane. The studies of their mechanical properties is essential for the basic understanding of the correlation between the structures and the transport properties.[21] Understanding mechanical properties is needed to develop better-performing membranes and also to evaluate the possible practical implementations. This chapter will discuss the transport mechanisms through the membranes and the method and techniques available for the physical and chemical characterisation of membrane properties.

2.1 Gas Transport in dense membranes

A membrane is a selective barrier that can be permeated by different chemical species at different ratios, under the action of a driving force. In membrane separation processes the incoming feed stream is separated into two streams: the permeate, composed in majority by the molecules which are able to penetrate in the membrane fastest, and the retentate composed mostly by the molecules rejected by the membrane (Figure 2.1).
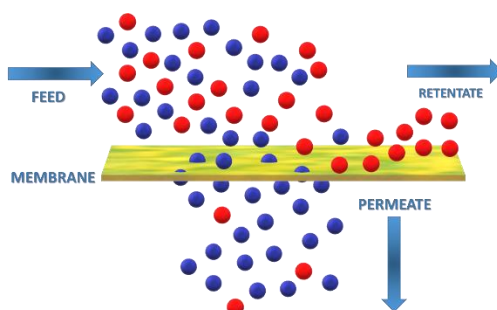
Figure 2.1 Schematic view of the membrane separation process

The separation performance of a membrane is described by two parameters: the permeability and the selectivity. The permeability is an amount of gas, which passes through the membrane with a specific thickness (*l*), area (*A*) in a unit of the time under the influence of a driving force, Eq. 2.1 and it is an indicator of the membrane material productivity. The selectivity is given by the ratio between the permeability of the two species to be separated, Eq. 2.2.

$$Permeability\ (P) = \frac{Quantity\ *\ Lengh(l)}{Area(A)\ *\ Time(t)\ *\ Driving\ force} \qquad \text{Eq. 2.1}$$

$$\alpha_{\frac{a}{b}} = \frac{P_a}{P_b}$$

The gas transport in dense membranes is generally described by the solution-diffusion mechanism. The solution-diffusion model can be reassumed in three steps: the absorption of the gas at the membrane-polymer interface at the feed side, followed by the diffusion of the dissolved species through the membrane bulk, and finally its desorption from the membrane in the permeate side (Figure 2.2a). The penetrant diffusion may be considered as a statistical molecular transport resulting from random molecules motion.
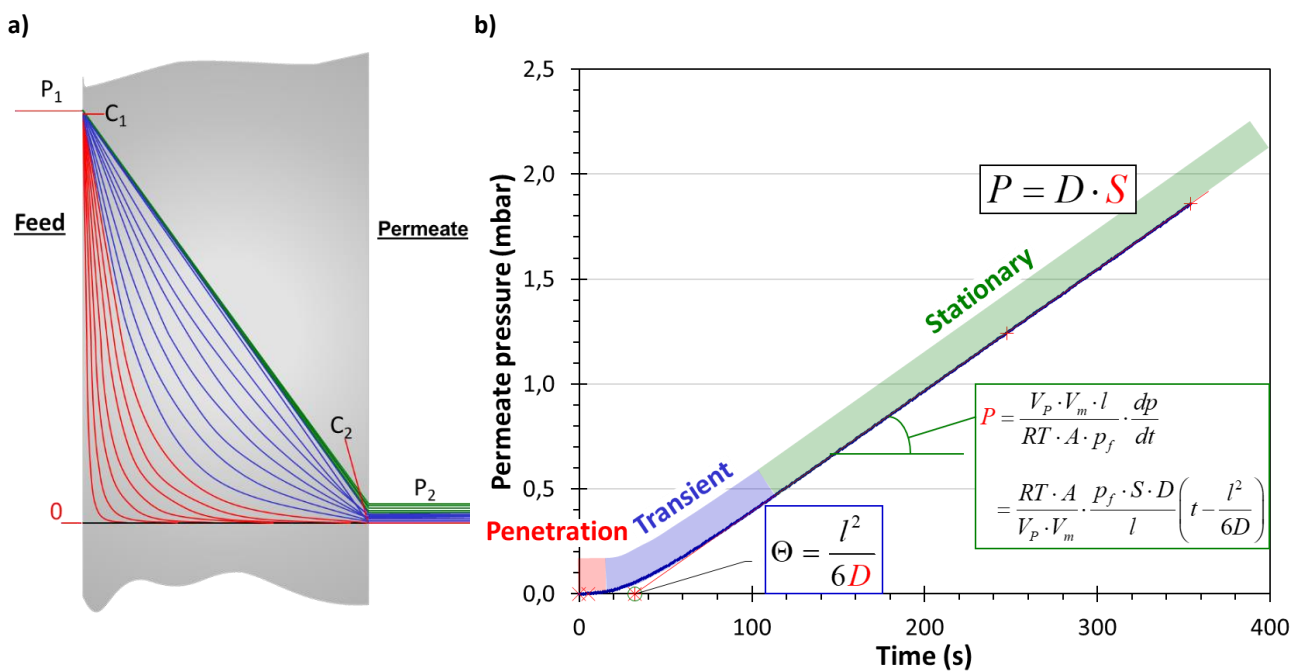
Figure 2.2 (a) Concentration profiles of a gas in a membrnae as a function of time after the first exposure of the membrane to the gas. (b) Example of a curve of the pressure as a function of time of gas in a constant volume set up during a typical time-lag measurement, and equations defining the three fundamental transport properties, *P*, *D* and *S*.

The simplest way to describe the flux of a given gas through a solid media is described by Fick's law:

$$J = \frac{D(C_1 - C_2)}{l} = -D\frac{\partial C}{\partial x}$$

The permeate flux *J* is proportional to the difference between the concentration on the feed side (C_1) and the permeate side (C_2), which represents the driving force, and it is inversely proportional

to the thickness of the membrane *l* (Figure 2.1). The proportionality constant *D* is called *diffusion coefficient*. It is possible rewrite Eq. 2.3 as:

$$J = -D\nabla C \qquad\qquad \text{Eq. 2.4}$$

In simple cases where the unidirectional penetrant flux obeys Fick's law, the permeability is generally expressed as the product of the diffusion coefficient *D* and solubility coefficient *S*:

$$P = D * S \qquad\qquad \text{Eq. 2.5}$$

The diffusion is a kinetic parameter, strongly connected to the membrane free volume and its size distribution and spatial distribution. The presence of interconnected channels in the membrane is favourable for the transport.[42] Generally, the gas diffusivity increases with decreasing kinetic diameter, but different factors could determine deviation from this trend: the chemical nature of the permeating species and molecules shape and dimensions. The solubility, that controls the absorption phenomena, is a thermodynamic parameter that depends on the interactions between the penetrant and the matrix membrane. The solubility of a gas in a membrane can be described by Henry's law, which indicates that a linear relationship exists between the external pressure *p* and the concentration *C* inside the membrane:

$$C = S * p \qquad\qquad \text{Eq. 2.6}$$

2.2 *Time-lag method and determination of the diffusion coefficient*

The time-lag method is the simplest and most commonly used technique to determine the diffusion coefficient of gases in dense membranes.[43,44]

This method is based on the penetration theory. In the most common setup, the membrane is fixed in a permeation cell with two separate compartments (feed and permeate) and after an evacuation of both sides of the membrane for a sufficiently long time to remove all previously absorbed species, it is exposed to a gas at the feed side. From that moment, the pressure is recorded in the permeate side with constant volume. Figure 2.3 shows a scheme of the experimental set up.

A typical time-lag curve, Figure 2.2b, presents an initial penetration region in which the gas absorbed at the feed side of the membrane starts diffusing across the membrane bulk, but it does

not reach the permeate side. In the transient region, the first gas molecules start desorbing from the membrane at the permeate side, and the rate gradually increases until it becomes constant in the final stationary stage. These three phases enable the calculation of the diffusion coefficient, whereas the stationary state is sufficient to determine the permeability coefficient.
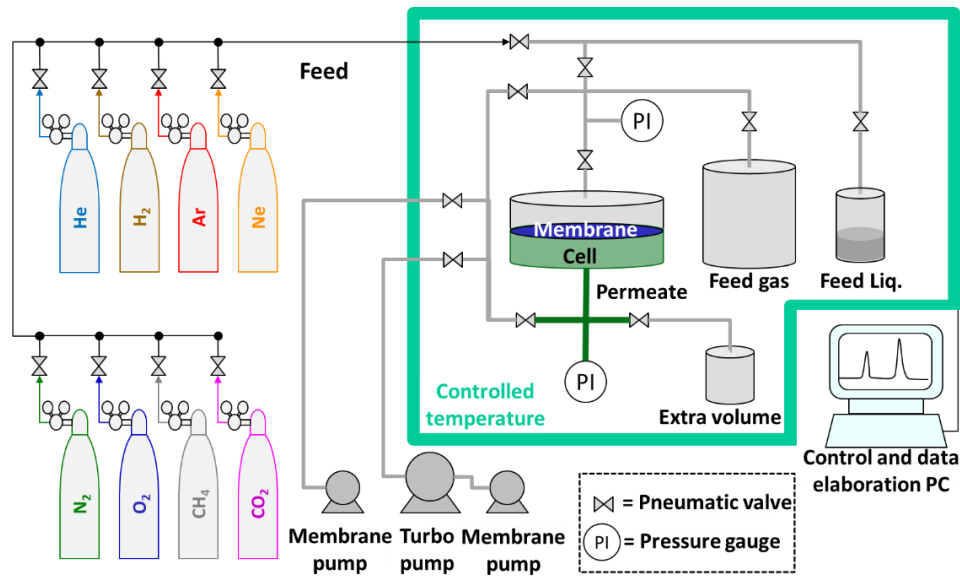
Figure 2.3 Scheme of the constant volume / variable pressure instrument for permeability and time lag measurements with pure gases.

When the solubility of the gas and its diffusion coefficient in the polymer are both constant, the time-lag Θ, defined as the intersection of the tangent to the steady-state permeation curve and the horizontal axis (Figure 2.2), can correlate with the diffusion coefficient:

$$\Theta = \frac{l^2}{6D} \qquad \text{Eq. 2.7}$$

the diffusion coefficient can be obtained by time lag measurements if the membrane thickness is known.

$$D = \frac{l^2}{6\Theta} \qquad \text{Eq. 2.8}$$

The entire permeation curve is expressed by an equation derived from Fick's first and second laws:

$$p_t = p_0 + \left(\frac{dp}{dt}\right)_0 t + \frac{RTA\,l}{V_p V_m} p_f S \left(\frac{Dt}{l^2} - \frac{1}{6} - \frac{2}{\pi} \sum_1^\infty \frac{(-1)^n}{n^2} \, exp\left(-\frac{Dn^2\pi^2 t}{l^2}\right)\right) \qquad \text{Eq. 2.9}$$

Where the derivate p_0 is the starting pressure and $(dp/dt)_0$ the slope of the baseline in the penetration state of the time-lag curve, which is related to the eventual presence of micro-defects in the membrane or leaks in the system. R is the universal gas constant, T is the absolute temperature, A is the exposed surface area of the membrane, l is the thickness, V_p is the permeate volume, V_m is the molar volume of the penetrant gas in standard conditions, p_f is the feed pressure, S is the solubility coefficient, D is the diffusion coefficient.

In the stationary state, the exponential tends to zero and if the baseline slope and the initial pressure is close to zero, Eq. 2.9 can be rearranged as:

$$p_t = \frac{RT \cdot A}{V_P \cdot V_m} \cdot \frac{p_f \cdot P}{l} \cdot \left(t - \frac{l^2}{6D} \right) \qquad \text{Eq. 2.10}$$

Assuming the validity of solution-diffusion model, the permeability can be calculated from the slope of the stationary part of the time-lag curve:

$$P = \frac{V_P V_m l}{RTA p_f} \cdot \frac{dp}{dt} \qquad \text{Eq. 2.11}$$

if there is a membrane with pinhole defects or in the case of minor leaks in the instrument, p_0 and $(dp/dt)_0$ may not be negligible, and Θ must be calculated from the intersection of the tangent to the stationary state and the tangent to the initial part of the permeation curve, which acts as the baseline as shown in Figure 2.4.
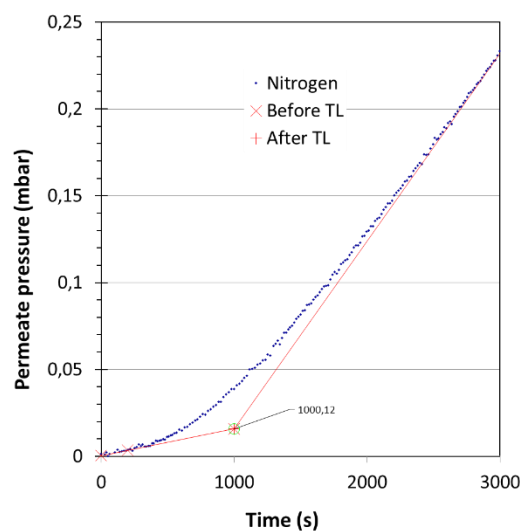
Figure 2.4 Baseline slope in the initial part of a permeation curve.

In case of a non-negligible baseline slope, for instance for membranes with a very low permeability, it should be roughly constant when it is due the leaks flow of the instrument and should be inversely proportional to the square root of the molar mass of the gas, when the baseline slope is due to pinholes in the membrane. The latter gives useful information about the quality of the membrane.

2.3 Temperature Dependence of Gas Permeation and Diffusion

The gas transport through dense membranes is an activated process, which can usually be represented by the Arrhenius-van't Hoff equations. For this reason, the transport rate may be strongly affected by the temperature. The temperature dependence of the permeability of a penetrant is described by following equation: [45]

$$P = P_0 \, exp\left(\frac{-E_p}{RT}\right)$$
<div align="right">Eq. 2.12</div>

where, P_0 is the temperature independent pre-exponential factor, R is the universal gas constant, T is absolute temperature and E_p is the activation energy of the permeation. This equation reflects the respective temperature dependence of the diffusion and sorption coefficients, Eq. 2.13 and Eq. 2.14, on the basis of Eq. 2.5.

$$D = D_0 \, exp\left(\frac{-E_d}{RT}\right)$$
<div align="right">Eq. 2.13</div>

$$S = S_0 \, exp\left(\frac{-H_s}{RT}\right)$$
<div align="right">Eq. 2.14</div>

Diffusion is an activated phenomenon, which usually increases at increasing temperature. Sorption is a thermodynamically based coefficient and decreases with temperature. In the equations D_0, and S_0 are temperature independent pre-exponential factors, E_d is the activation energy of the diffusion and H_s is the heat of sorption. E_d is always positive for all the gases, whereas the activation energy of permeability E_p depends on the relative magnitudes of E_d and H_s, Eq. 2.15.

$$E_p = E_d + H_s$$
<div align="right">Eq. 2.15</div>

The pre-exponential factor D_0, according to the transition theory of diffusion can be expressed as the following equation:

$$D_0 = e\lambda^2 \frac{kT}{h} exp\left(\frac{S^*_d}{R}\right)$$
Eq. 2.16

Where λ is the average diffusive jump length which represent the distance between two neighbouring cavities, S^*_d the activation entropy of diffusion, and h and k are the Planck and the Boltzmann constant, respectively.

The diffusivity selectivity can be described as the product between two terms: the entropic and an energetic selectivity term:

$$\frac{D_x}{D_y} = \frac{\lambda_x^2}{\lambda_y^2} \underbrace{exp\left(\frac{\Delta S^*_{d(x,y)}}{R}\right)}_{entropic\ selectivity} \underbrace{exp\left(-\frac{\Delta E^*_{d(x,y)}}{RT}\right)}_{energetic\ selectivity}$$
Eq. 2.17

In which $\Delta S^*_{d(x,y)}$ called entropic selectivity, is the difference in the activation entropy of diffusion for two gases x and y, and the energetic selectivity $\Delta E^*_{d(x,y)}$ is the difference in the activation energy of diffusion between the same gas pair.

For well-packed dense membranes, the average diffusive jump length is proportional to the effective diameter of the penetrant gas. Thus, even if the effective diffusive jump length is not known, the ratio λ_x^2/λ_y^2 can be approximated as d_x^2/d_y^2 where d is the effective diameter of the two gases.[46,47] In this work, the effective diameters estimated by Teplyakov and Meares are used for the approximation of the jump length, since these give the best correlation with D.[48]

The energetic selectivity refers to the difference of energy needed to open a motion-enabled zone for diffusion for a gas over that required for another one. The energetic selectivity is a size-dependent process that favours the smaller of two penetrants. In a nonporous polymer matrix, a gas diffuses with size-dependent jumps. These jumps depend on the activation energy needed to create transient gaps of sufficient size to enable the jump to occur. Smaller penetrants require the localization of less activation energy.[49–51]

The ability of a material to limit the degree of freedom of one gas molecule relative to a second one is related to the entropic selectivity. The degree of freedom is associated to the vibrational, rotational and translational modes of the molecules. The entropic term of diffusing molecules is related to transition between a normal and activated state. The transition state occurs as the gas molecule passes through the constricted "windows" of molecular dimensions, *i.e.* the region A' in

Figure 2.5, while molecules in the large cavities (region A in Figure 2.5) are referred to as being in the normal state.[49,51]
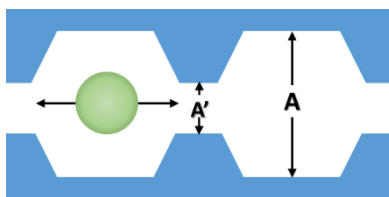
Figure 2.5 Idealized schematic of a constricted "window" of molecular dimensions (region A') referred to as transition state and large cavity (region A) referred to as normal state.

2.4 Mechanical tensile tests

The most commonly used method to study the mechanical properties of polymer films is the uniaxial stress-strain test, also known as tensile test. Tensile testing is a destructive process that it measures the force required to stretch a specimen, which elongates to the breaking point. A test specimen of known dimensions is placed between two grips which clamp the material in aligned way. If the specimen is misaligned, the machine will also exert a bending force on the specimen. In the setup used in the present work, the sample is elongated with a constant and controlled speed and at the same time the required force (or load) is measured. This method allows to determine different characteristics of the material such as mechanical strength (R_m), elastic Young's modulus (E) and elongation percentage (ε). A sample of known dimensions undergoes a monoaxial load, starting with a zero initial deformation that increases in time, with a certain speed, until the break point. Information on the tensile modulus can be obtained from a stress-strain diagram, which relates the deformation at a constant rate and the consequent stress. The tensile modulus, E, is obtained from the initial slopes of the stress-strain curves, as shown in Figure 2.6.

A small force is sufficient to obtain a large deformation in an elastomer, whereas a small deformation in glassy polymers require a large force. Glassy polymers have a high elastic modulus and they usually yield (if tough) or break (if brittle) at small elongation. They can be hard and fragile, but also extremely resistant, such as polycarbonate, which is used for safety glass because of its high impact resistance. The brittleness is influenced by different factors such as molecular weight, crystallinity (in semi-crystalline polymers) and intermolecular forces. Increasing the temperature, glassy polymers generally present a lower modulus and a greater elongation, becoming soft and

tough. Figure 2.6 shows how different stress-strain curve shapes correspond to different sample behaviours and gives some definitions that characterize the different material properties.

The initial linear deformation in the stress-strain curve is the elastic region. The elastic deformation depends on small local "movements" of the polymer chains, related to the change of the bond angles and their stretching. This type of deformation is reversible. Plastic deformation at higher elongation is attributed to the sliding of larger segments of the polymer chains. On the contrary of the elastic zone, this type of deformation is irreversible.
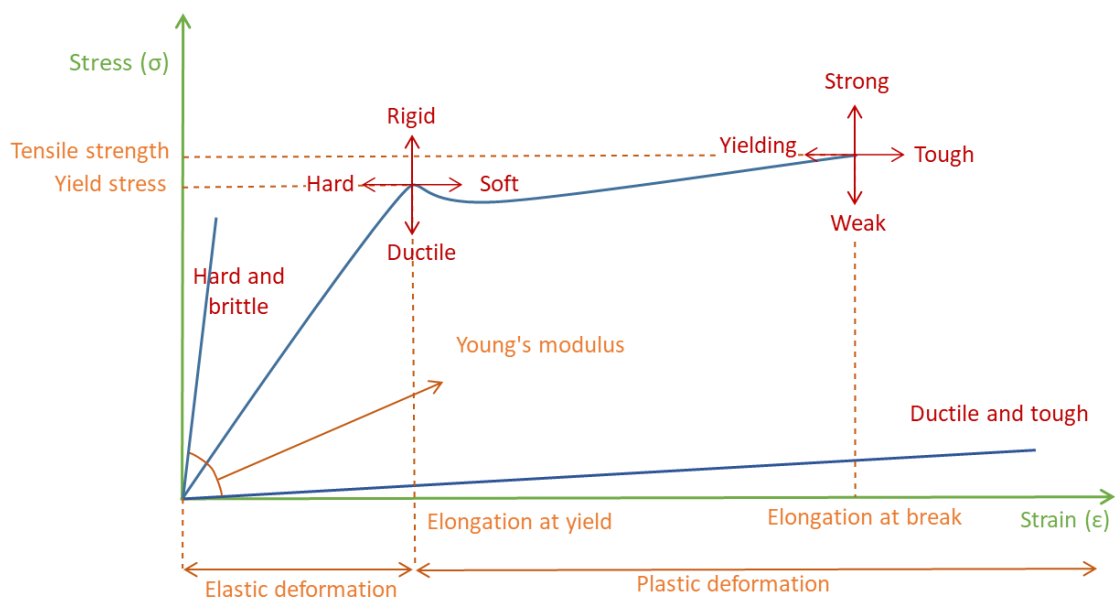
Figure 2.6 Schematic representation of the stress-strain diagrams of materials with different characteristics.

In the stress-strain curve, the tensile modulus or Young's modulus E is given by the initial slope of the curve:

$$E = \left. \frac{\partial \sigma}{\partial \varepsilon} \right|_{\varepsilon=0}$$

Eq. 2.18

in which ε is the strain and σ the stress. In general, ε is defined for a finite deformation as ε = (L - Lo)/Lo where Lo is the initial length an L the actual length. The stress σ is the force F per the cross-sectional area. The maximum in the stress-strain curve (or the point where the elastic deformation becomes plastic deformation, defines the stress at yield, σ_y and the elongation at yield ε_y (yield-strain).

2.5 Atomic Force Microscopy

Since its invention in 1986 by Binnig, Quate e Gerber,[52] Atomic force microscopy (AFM) has played an important role in studying the structure and the physicochemical properties of polymer materials. An AFM allows acquiring three-dimensional topographical images of surfaces using a cantilever of micrometric dimensions at the end of which a very thin tip is placed. The sample is fixed on a piezoelectric scanner, which controls the movement of the sample in the x, y, and z directions with respect to the tip apex. The tip is placed in the immediate vicinity of the sample surface. The interaction between the tip and the sample causes the bending of the cantilever. A laser beam is reflected off the back of the cantilever, and the changes in the cantilever deflection are detected with a position-sensitive photodiode detector that measures small changes in the position of the reflected laser beam. This deflection is processed by the microscope electronics to determine topological height changes on the sample surface. The achievable lateral resolution depends on the details of the tip geometry but can approach sub-nanometre levels. Imaging of polymeric materials with nanoscale resolution and the simultaneous measurement and mapping of the physical properties, like the elastic modulus, provides a unique means of linking structure to properties, opening pathways for the development of more advanced materials. The AFM can work either in air or in other fluids to avoid frictional forces or capillaries between tip and sample. In force spectroscopy mode, AFM allows to plot the deflection of the cantilever as a function of the tip distance from the sample surface. The force vs displacement curve (FD curve) shown in Figure 2.7 gives information about the elasticity and viscoelasticity of materials.[26] The interaction between the AFM tip and the investigated surface may be interpreted with the general theory of contact mechanics. Contact mechanics is the study of the stresses and deformation that arise when two elastic solids come in contact with each other. Several contact mechanical models have been developed to characterize this interaction. These models take into account the geometry of the tip as well as the thickness and adhesion characteristics of the sample. The models described in the following paragraph are the most common contact mechanical models that have been applied to indentation experiments.

2.5.1 Interaction forces and imaging mode

In atomic force microscopy, the van der Waals (vdW) interactions play a prominent role. The vdW forces are present between uncharged atoms or molecules, leading not only to phenomena like the cohesion of condensed phases and physical adsorption of gases, but also to a universal force of attraction between macroscopic bodies. Hamaker in 1937 together with Derjaguin (1934) developed the theory of vdW forces between macroscopic bodies.[53,54] This theory is used to calculate the vdW interaction between the tip and the sample surface schematised respectively with a sphere of radius R and a flat surface. The resulting interaction laws, given in terms of the Hamaker constant (*A*) may be written as:

$$F(D) = \frac{-AR}{6D^2}$$

Eq. 2.19

Where *R* is de radius of the sphere and *D* the distance between the sphere and the flat surface. The interaction potential, *W(D)*, is defined as:

$$W(D) = \frac{-AR}{6D}$$

Eq. 2.20

The Hamaker's coefficient (or constant), being equal to:

$$A = \pi^2 C_L \rho_1 \rho_2$$

Eq. 2.21

The Hamaker constant depends on C_L, a microscopic property of two interacting atoms, then ultimately depends on the strength of the interaction between bodies and the medium surrounding them. *A* also depends on the densities of both materials, ρ_1 and ρ_2 in the formula, and it assumes values between 4 and 0.4 10^{-19} J.[52]

As shown in Figure 2.7, in accordance with the interaction forces between the tip and the sample surface, the AFM can work in contact, non-contact and intermittent contact or tapping mode.

In contact mode, the tip is physically in contact with the sample surface. The repulsive forces developed between the tip and the sample result in deformation of the sample. In the non-contact mode, the tip is close to the sample surface but it does not actually touch it, and the tip is affected by the attractive vdW forces. Finally, in the tapping mode, the oscillating tip scans the sample in order to have an intermittent contact and to be affected by both attractive and repulsive forces.
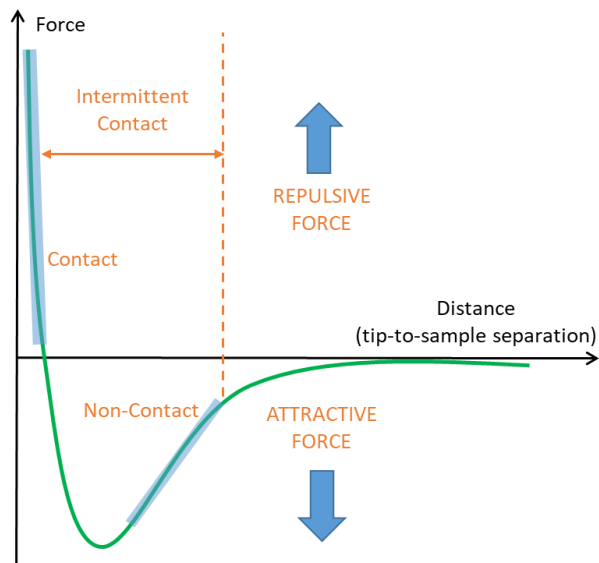
Figure 2.7 Force dependence between tip and sample surface as a function of their distance. The AFM operating modes are indicated

The tapping mode overcomes the problem of friction forces between the tip and the surface, allowing to acquire high resolution topographies even of surfaces that are easily damaged and difficult to analyse with other methods. In tapping mode, the cantilever oscillates with a frequency just below its resonance frequency, f in Figure 2.8a.
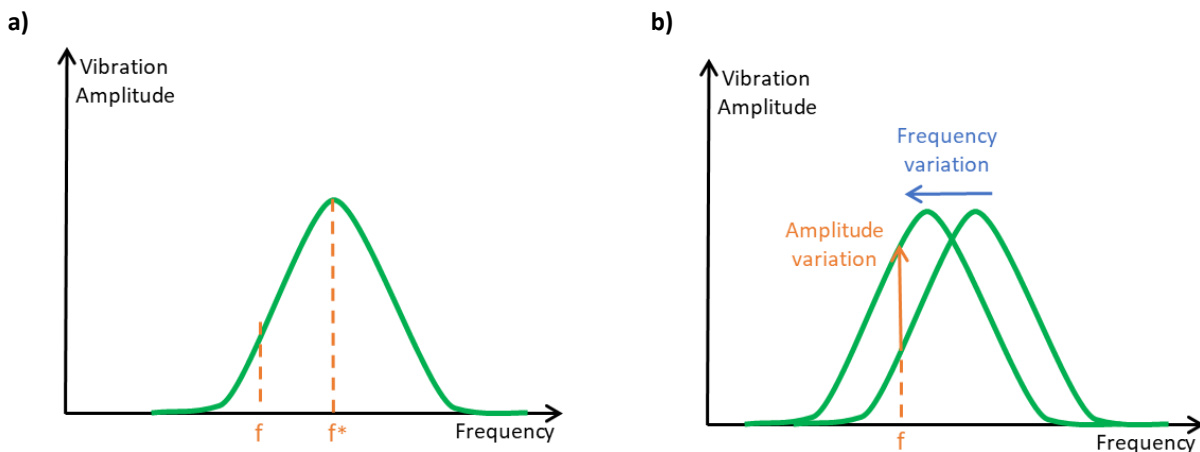
Figure 2.8 Amplitude and frequency variation in tapping mode. Green curve: freely moving tip. The amplitude change provide information of the material properties.

When the tip approaches the sample surface and feels the interaction forces, a shift in the resonance curve are observed, Figure 2.8b. As it scans, the microscope maintains a constant frequency with a consequent increase of the oscillation amplitude bringing the tip into intermittent

contact with the sample. In addition to the topographic image, it is also possible to acquire a phase image. The phase is a qualitative measure of the energy dissipation involved in the contact between the tip and the sample, which depends on a number of factors, including such features as viscoelasticity, sample composition, adhesion forces and also contact area.[55] As the contact area depends on the slope of the sample, the phase image also contains topographic contributions.

2.5.2   Force Spectroscopy mode

Force spectroscopy consists in the measurement of the deflection of the cantilever when the sample placed on the scanner perpendicularly approaches the tip and retracts from the tip. This allows to measure the force interaction between the AFM tip and the sample surface as a function of their separation distance. The force-distance (FD) curve provides information about the long range attractive or repulsive forces acting between the tip and the sample surface, and about the local mechanical properties of the sample. As can be seen in Figure 2.9, the approaching and withdrawal of the tip can be divided into four distinct steps.

At the beginning, point A, there is a large distance between the tip and the sample surface. No interaction is established between them, and thus there is no measurable force. The progressive approaching results in a small downward deflection of the cantilever due to the attractive forces, until the gradient of the attractive forces exceeds the elastic constant of the cantilever. The tip reaches an unstable position, resulting in a snap-into-contact of the tip on the surface, point B. During the progressive expansion of the piezoelectric scanner, the cantilever bends from a concave shape (attractive regime) to a convex shape (repulsive regime) when the tip and the surface are in contact. The expansion of the piezoelectric scanner is stopped, point C, in the elastic domain of deformation of the cantilever. During the withdrawal of the tip by contraction of the piezoelectric scanner, the tip stays in contact with the surface and the force decreases to zero and becomes negative, until the pulling force by the piezoelectric scanner overcomes the tip-surface adhesion, and this results in the jump out of contact of the tip, point D. The difference between the zero normal force and the force preceding the jump out of contact is called the pull-off force.

The hysteresis between the retracting and the approaching curves is due to the tip-surface adhesion. The capillary forces, the increase of the contact area and short-range forces are the principal causes of the tip-surface adhesion.
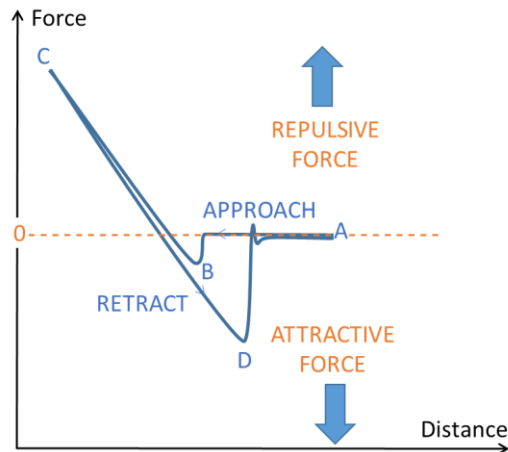
Figure 2.9 Force–distance curve. At point A, the probe is far from the surface, at B "snap-into-contact" occurs as attractive forces pull the probe onto the surface. The force becomes repulsive as the probe continues to be driven towards the sample, C. During the subsequent retraction, at point D 'pull-off' occurs as the force applied to the cantilever overcomes tip–sample adhesion.

2.5.2.1 Calibration

To obtain an FD curve as the one shown in the previous figure, a calibration of the photodiode signal and of the lever elastic constant is needed. Calibration of the deflection sensor is necessary (i.e. calculation of the conversion factor of photodiode reading from V to nm) because the photodiode output can vary depending on the exact position on the cantilever where the laser beam is reflected. The calculation of the deflection sensitivity factor requires the acquisition of a force vs. distance curve on a hard substrate. Mica and sapphire were used during the course of the experiments presented in this Thesis. The stiff nature of mica and sapphire permits the deformation of the cantilever only, and the resulting cantilever deflection (which is proportional to the photodiode voltage) will be identical to the piezo-actuator displacement. Finally, the inverse of the slope of the force-distance curve at the contact region is a measure of the cantilever deflection sensitivity (measured in nm·V^{-1}). Once the photodiode is calibrated, force vs distance in N vs nm can be acquired (Figure 2.10).
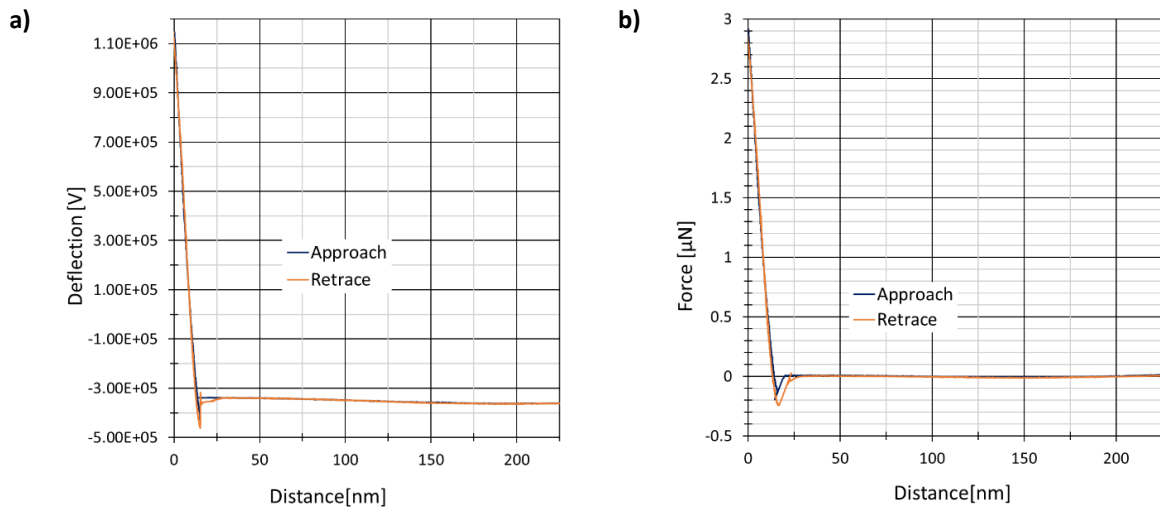
Figure 2.10 Deflection as a function of scanner expansion (Z(V)) curve (a) and Force- distance curve (b).

The procedure for the calibration of the cantilever spring constant is performed through the following steps:

• Selection of a force calibration cantilever called *CLFC* with a known spring constant (k_{ref}), in a range with respect to the nominal spring constant of the unknown cantilever, k_{nom}, *given by 0.3xk_{ref} < k_{nom} < k_{ref};*

• The *CLFC* cantilever, the dark one in Figure 2.11, is positioned on the AFM sample stage, such that it is aligned with the cantilever to be calibrated, but facing the opposite direction, (Figure 2.11b);

• Engaging in contact mode, several measurements of the deflection sensitivity are made on a hard substrate and the average of the results is calculated to obtain the average deflection sensitivity on the *CLFC* cantilever, S_{hard}. (Figure 2.11c);

• After this procedure, the cantilever to be calibrated, the bright one, is aligned close to the end of the *CLFC* cantilever, (Figure 2.11d); Several measurements of the deflection sensitivity are made and an average of the results is calculated to obtain the average deflection sensitivity on the *CLFC* cantilever, S_{ref};

• The length, *L*, of the unknown cantilever and the offset *ΔL* of the tip from the end of the reference cantilever is measured;

• The spring constant of the unknown cantilever is calculated using the following equation:

$$K = K_{ref} \left(\frac{S_{ref}}{S_{hard} - 1} \right) \left(\frac{L}{L - \Delta L} \right)^3 \qquad \text{Eq. 2.22}$$

Uncertainty in the calibration is dominated by the error in determining the deflection sensitivity values.

a)

b)

c)

d)
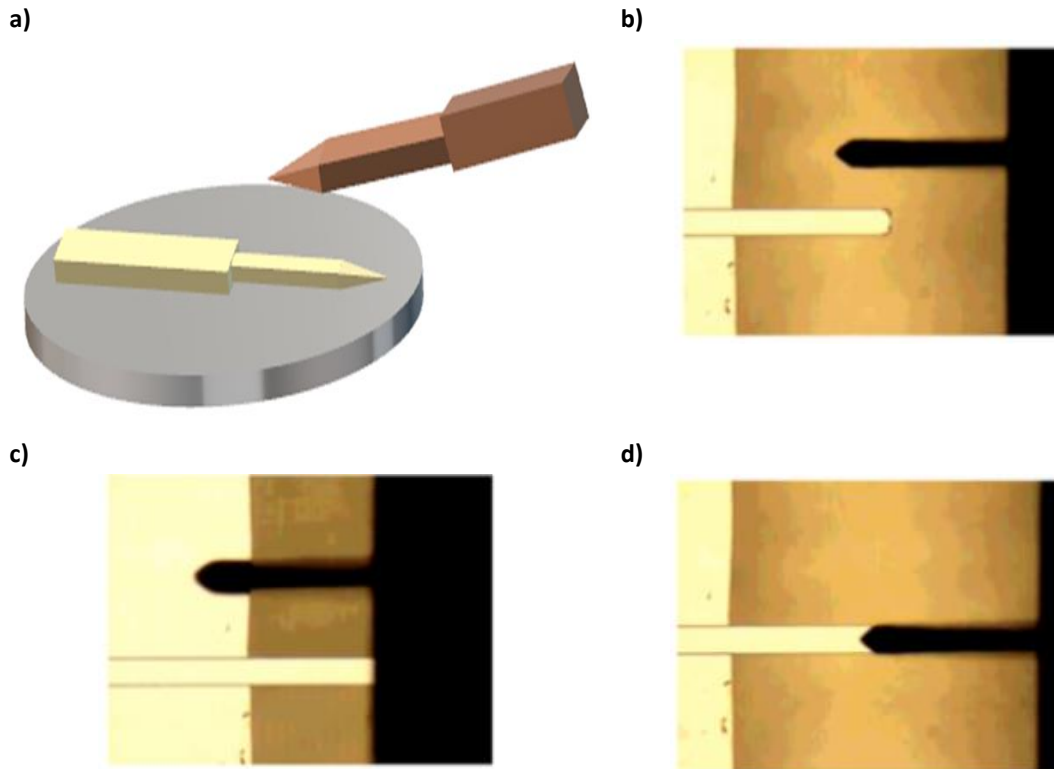
Figure 2.11 Calibration using a CLFC cantilever (black) as the reference cantilever and the bright one is the cantilever with unknown elastic constant.

2.5.2.2 Quantitative analysis

Once the FD curve is correctly acquired it is possible calculate information on Young's modulus of the sample. Several contact mechanical models have been developed to describe this interaction. These models consider the geometry of the tip and assume that only elastic compressions of the sample take place.

2.5.2.3 Hertz model

In 1881 Heinrich Hertz in his paper titled "On the contact of elastic solid" explained how the elastic contact theory between two spheres could be extended to a sphere in contact with a flat surface, neglecting the adhesion and surface forces [56].
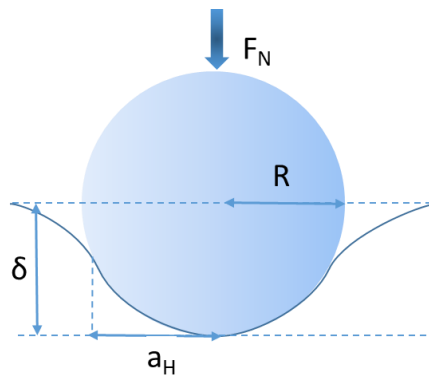
Figure 2.12 Hertz model for an elastic sphere in contact with an elastic half space.

Hertz derived an equation to describe how the interaction forces between a not deformable spherical and a flat surface (Figure 2.12) depend on the surface properties, and it is given by the following equation:

$$F = \frac{4}{3} \frac{E\sqrt{R\delta^3}}{(1 - v^2)}$$

Eq. 2.23

where R describes the effective sphere radius, E the Young's modulus, a is the contact radius, v the Poisson ratios of the surface and δ the indentation depth. The Poisson ratio is a measure of the deformation of a material perpendicular to the force direction.

2.5.2.4 Sneddon Model

In 1948 and further on in 1965, Sneddon proposed, for small displacements, a conventional method for extracting the elastic properties from indentation that extends the Hertzian formulation and is valid for conical tip in contact with a plane. [57]
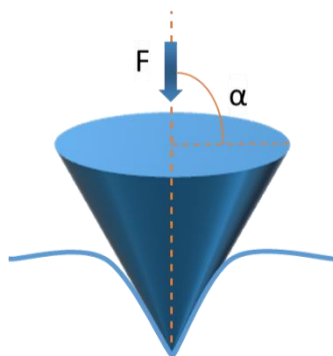
Figure 2.13 Contact between a conical tip and an elastic half-space.

The Hertz-Sneddon theory predicts that the force increases non-linearly with the indentation depth, δ [57]:

$$F = \frac{2}{\pi} \frac{E}{(1 - v^2)} (\delta)^2 \, tan(\alpha) \qquad\qquad \text{Eq. 2.24}$$

where *F* is the force, *E* the Young's modulus, *υ* is the Poisson ratio (assumed to be 0.3)[58] and α is the half-angle of the cone.

Depending on the experimental conditions, these two models are used to fit FD curves data in order to calculate the Young's modulus of the sample.

Force spectroscopy determination of Young's modulus in mixed matrix membranes. [1]

3.1 Introduction

An interesting method to improve the gas separation performance of a membrane is the preparation of mixed matrix membranes (MMMs), i.e. the incorporation of a filler or additive in the polymer matrix.[6,7] The main idea is to combine the good processability and mechanical stability of the polymer, with the superior gas transport properties of suitable fillers, including ionic liquids (ILs).[10] Ionic liquids (ILs) are a class of room temperature molten salts composed of anions and cations. ILs can exhibit a wide range of properties due to the facility to change their properties by variation of their functional groups. They possess thermal and chemical stability, extremely low saturated vapour pressure and a tuneable nature.[59] ILs have been recognized as an alternative to classical organic solvents, mainly due to their ability to solubilize a large range of organic molecules. Adding ionic liquids in polymer membranes offers a range of advantages. Mass transport in ILs is usually much faster than in pure polymeric materials, thus allowing higher fluxes through the membrane.[11] In 1999, Blanchard *et al.* reported that CO_2 has high solubility in the IL [BMIM][BF_6].[60] Subsequently, a large number of studies investigated the influence of functional groups, the alkyl chain length and the anions on the CO_2 solubility.[11,59]

The polymer chosen for this thesis study is Pebax®. Pebax®1657 is an elastomeric multiblock copolymer, with a molecular structure consisting of amorphous rubbery polyether blocks and semi-crystalline polyamide blocks. The Pebax® family consists of various different copolymers and the properties of each copolymer are related to the relative content of PE and PA and to their chemical characteristics. Pebax® block copolymers contain a phase separated microstructure in which the hard PA segments provide mechanical stability and contribute to crystallinity, while only the soft PE blocks act as permeable phase owing to their high chain mobility and thus control the gas transport. This polymer is already used for CO_2 removal from light gases,[61] and here it is proposed further modification by the incorporation of ionic liquids. The choice of the particular IL, 1-butyl-3-methylimidazolium tetrafluoroborate, [BMIM][BF_4], is dictated by the results of previous works, which show that ILs containing fluoroalkyl chains improve the CO_2 solubility.[62,63] The proposed Pebax®/IL membranes present a complex multiphase system with different local mechanical properties. High performance membranes must couple superior gas transport properties to mechanical stability at the working conditions. Jansen *et al.* have demonstrated that the mechanical properties of IL containing membranes may be correlated with their transport properties.[25]

Traditionally the mechanical properties are investigated by tensile tests or rheological characterization.[4] However, these techniques require often quite large sample sizes, which are not always available for novel experimental materials. When only small membrane samples are available, Atomic Force Microscopy (AFM) may allow the quantitative and qualitative investigation of the mechanical properties on different scales,[28–31] besides being a tool for imaging surface topography.[32] In this chapter, Atomic Force Microscopy (AFM) is presented as a powerful alternative to the more commonly used tensile tests for the calculation of the elastic modulus of polymeric membranes. The measurement of the Young's modulus by traditional tensile tests are compared with the results of AFM operated in Force Spectroscopy mode. AFM measurements are carried out with nano and micrometric tips on dense membranes of neat Pebax®1657 and on mixed matrix membranes of Pebax®1657 with different concentrations of the ionic liquid [BMIM][BF$_4$] (Figure 3.1). The use of a nanometric AFM tip enabled the determination of the local Young's modulus of the individual domains of the microphase-separated block-copolymer, while a larger tip gave average values of the bulk polymer. This offers good perspectives for the analysis of samples where traditional tensile tests cannot be used, for instance composite membranes or particularly small samples.
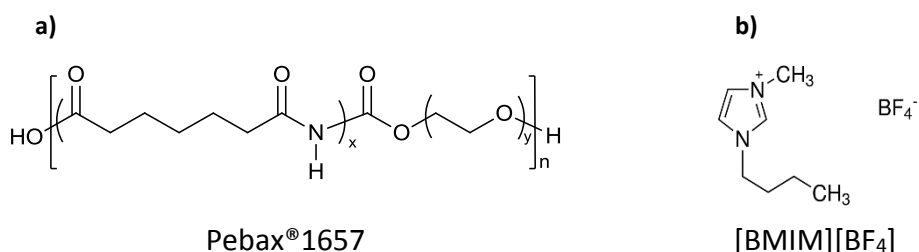
Figure 3.1 Structures of the polymer (a) and the ionic liquid (b) used in this work.

3.2 Membranes preparation

In this chapter, two sets of membranes were prepared. The first series was made starting with the swelling of the Pebax®1657 pellets in a mixture of ethanol/water (70/30 wt%) under stirring for 24 h, after which the solution was left for 2 h at 80 °C under reflux and vigorous stirring. The ionic liquid 1-butyl-3-methylimidazolium tetrafluoroborate ([BMIM][BF$_4$]) was added to the hot polymeric solution in different amounts (0-40 wt% on the basis of the final membrane weight after solvent evaporation). The resulting solution was stirred until it became homogeneous and then it

was poured into metal casting rings on a glass plate. Slow evaporation of the solvent at room temperature yielded translucent self-standing dense membranes with a thickness of about 100 μm.

Another set of membranes was prepared starting with disks of pure Pebax®1657 prepared by similar procedure of the previous set, without the addition of IL. Then, samples with a diameter of 47 mm were immersed in an excess of [BMIM][BF$_4$] to analyse the spontaneous IL absorption. The experiments were carried out at temperatures of 25 °C, 35 °C, 45 °C, 55 °C, 65 °C and 80 °C. The absorption of ionic liquid was determined by monitoring the weight and volume change of the samples as a function of the time and temperature, Figure 3.2.
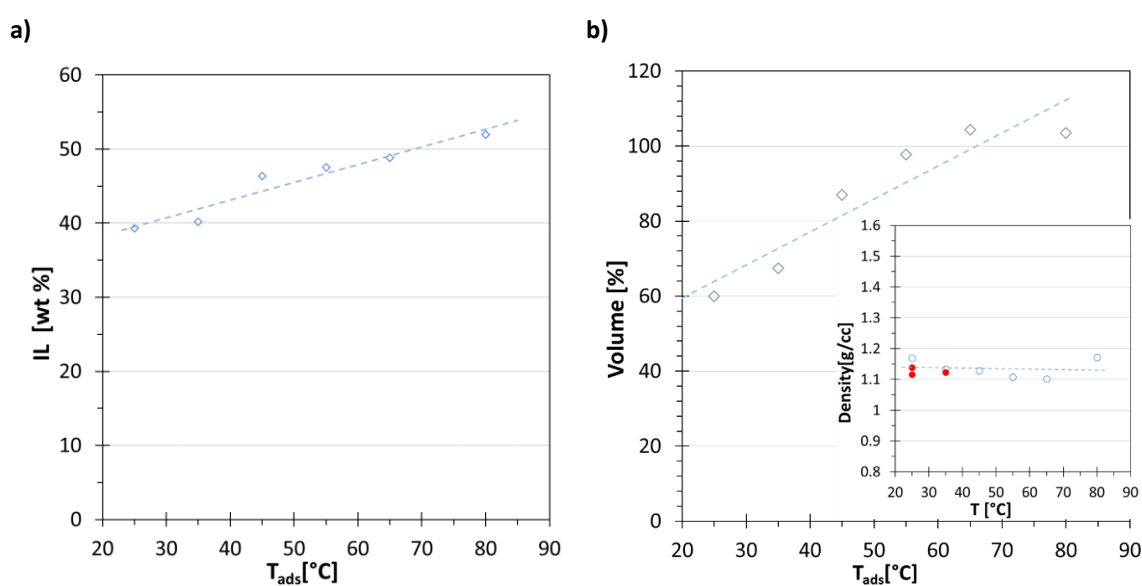
Figure 3.2 [BMIM][BF$_4$] percentage absorbed in Pebax®1657 at different temperatures (a) and volume change as a function of the adsorption temperature (b). The line is indicated as a guide to the eye. The insert shows the density, which tends to decrease slightly with increasing IL soaking temperature, and thus IL content, with exception of the last point, which may be an outlier.

Preliminary absorption kinetics measurements of the IL in these films revealed that equilibrium is reached in approximately 2 days or less. The equilibrium concentration ranged from ca. 40% at room temperature up to 55 wt% at 80°C (Figure 3.2a). The volume change with temperature increases from ca. +60% at room temperature up to ca. +100 wt% at 80°C (Figure 3.2a). This strong swelling means that Pebax®1657 has a high affinity for this IL even at low temperature. These experiments thus showed that higher temperatures favour the amount of ionic liquid absorbed, but the high spontaneous IL absorption even at low temperatures yields membranes with a relatively narrow range of high IL concentrations. Therefore, membranes with a precise amount of IL in a wider

(especially lower) range of concentrations were prepared by solution casting after adding a weighed quantity of ionic liquid to the polymer solution.

3.3 Membranes characterization

3.3.1 Gas permeation analysis

The effect of [BMIM][BF$_4$] on the gas transport properties of these membranes is plotted in Figure 3.3.
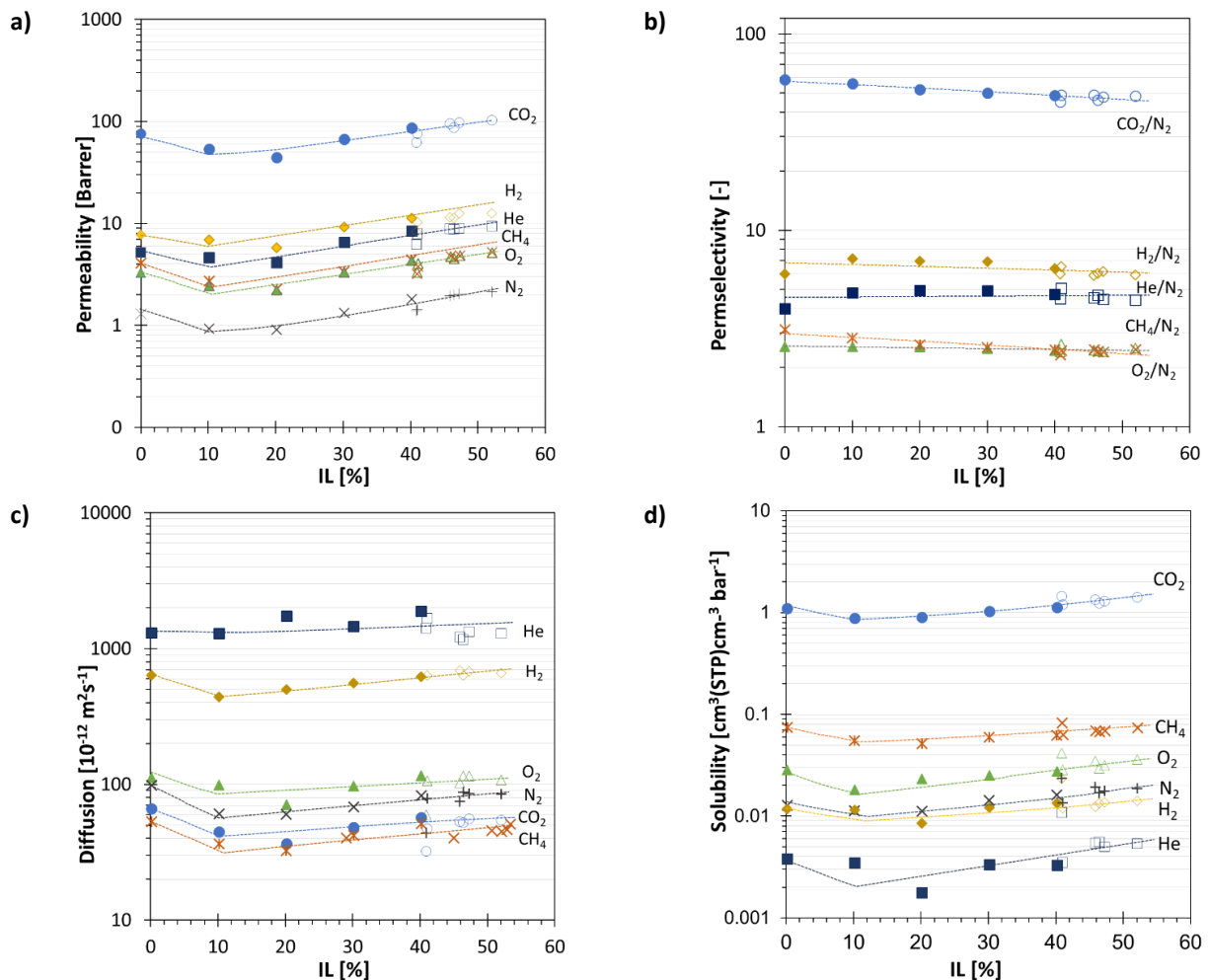
Figure 3.3 Transport properties of six gases as a function of [BMIM][BF$_4$] content in Pebax®1657 membranes. Filled symbols indicate the membranes prepared by addition of the IL to the casting solution; open symbols indicate the membranes prepared by spontaneous absorption of the IL in the pure Pebax® films. The lines are indicated as a guide to the eye.

After a small initial drop at low IL content, the permeability gradually increases with IL concentration for all gases, as previously observed for a similar system with $[BMIM][CF_3SO_3]$ [11] (Figure 3.3a). The permselectivity ($\alpha_{i/N2}$) is more or less constant at high IL content for all gases, except for CO_2 and O_2, for which the selectivity slightly decreases with increasing IL content (Figure 3.3b). The diffusion coefficients and the solubility show the same trend as the permeability (Figure 3.3c, d). The data of the membranes with spontaneous IL absorption (open symbols) and those where the IL is added before the solvent evaporation show generally excellent agreement, which indicates that the transport properties are mainly determined by the sample composition and not by the preparation history.

3.3.2 SEM, Topography and phase image

Figure 3.4a shows the SEM backscattered electron image of the pure Pebax®1657 membrane, confirming the smooth surface and dense membrane structure. Interestingly, the backscattering signal is capable of probing slightly below the surface of the sample and reveals the presence of larger dendrite-like structures. The contrast of the backscattered electron image shows the slight differences in the composition of the micro-phase separated block copolymer domains.
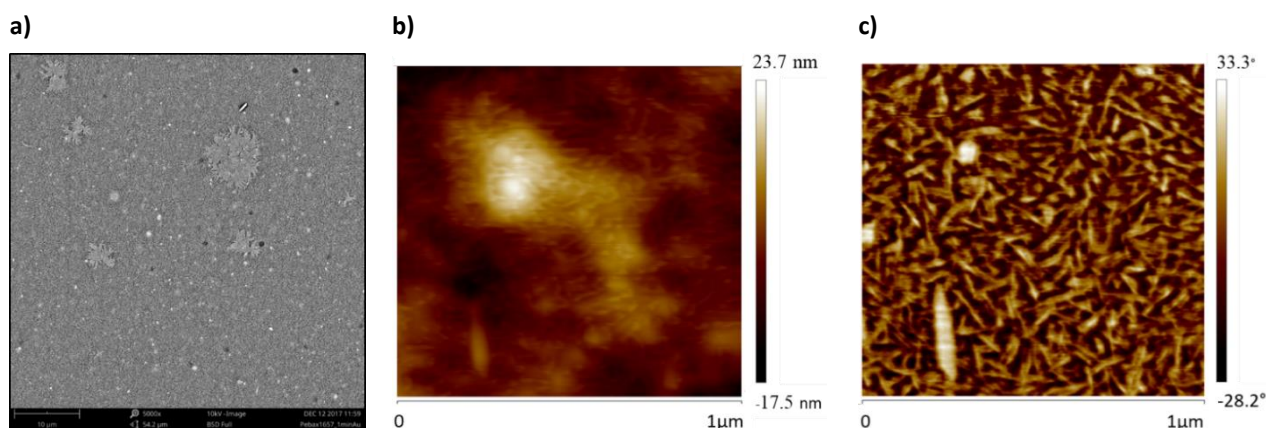
Figure 3.4 SEM image (a), topographic (b) and phase (c) AFM images acquired with a tip radius of 10 nm of the top surface of a neat Pebax®1657

The topographic image of the neat Pebax®1657 membrane, acquired in tapping mode, is shown in Figure 3.4b and the corresponding phase image in Figure 3.4c. The homogeneous surface shows a height variation in topography of about 40 nm, less than 0.05% of the total thickness. The phase

image shows a qualitative clear contrast between the needle-like stiffer domains (bright), dispersed in the softer matrix (dark), being a measure of the energy dissipation during the interaction between tip and sample surface.[55] [55]The hard domains are about 20-30 nm in width and 150-200 nm in length, and most likely correspond to the crystalline PA6 phase, whereas the softer domains correspond to the rubbery PEO phase.

3.3.3 Mechanical properties

Measurements were performed at room temperature in air and in silicon oil on a Multimode 8 AFM system with a Nanoscope V controller, using two different cantilevers. A conical tip with a nominal radius of curvature of 10 nm and a spherical tip with a radius of 2 µm allowed the investigation of the mechanical properties on two different scales. The silicon oil was preferred because it does not affect the membrane properties. In order to have a statistically relevant number of measurement points, for each membrane 60 FD curves were recorded at a scan rate of 400 nm s^{-1}. The FD curves were acquired in three different areas of each membrane, using two types of tips. To minimize capillary forces, due to the thin layer of humidity deposited on the sample surface, both the tip and the sample were immersed in silicon oil, which was verified not to affect the membrane properties. The cantilever properties are reported in Table 3.1. The data of each measurement curve were fitted using the NanoScope Analysis 1.5 software and the results were statistically analysed using OriginPro 8 (OriginLab Corporation) and Microsoft Excel.

Table 3.1 Cantilever characteristics

Cantilever name	TAP150	CP-PNP-SiO
Calibrated elastic constant (N m^{-1})	5*	65.5 (± 10%)
Nominal tip radius (nm)	10	2000 (± 5%)
Tip shape	Conical	Spherical
Producer	Bruker	SQUBE

* Nominal value supplied by the producer.

3.3.3.1 Force spectroscopy method development

The effect of the capillary forces due to the layer of humidity deposited on the sample surface can be minimised by operation in conditions of low humidity, or in a liquid. An example of the FD curves in air and in silicon oil is shown in Figure 3.5.

In air the approaching curve shows no interaction until ca. 150 nm and then the curve shows a very irregular shape due to uncontrolled adhesion forces between the tip and the condensed water layer on the sample surface (Figure 3.5a). The retraction curve is significantly different and presents two partial jump-off-contacts, which appear as small positive peaks on the retraction curve. This is likely due to the sudden loss of capillary forces between the tip and the surface with a condensed water layer, and causes a quite irregular curve shape. In addition to the viscoelastic properties of the polymer, the condensed water layer is the main cause of the strong hysteresis between approaching and retraction curve, and therefore the measurements were also carried out in the liquid phase. Silicon oil was used, although it has poor compatibility with water, in contrast to the often-used glycerol. However, polar liquids such as glycerol might interact with the sample's polyether phase, and therefore silicon oil was preferred. Indeed, the FD curve acquired in silicon oil is much smoother than the one acquired in air and presents no anomalies (Figure 3.5b). Thus, capillary forces are negligible compared to the van der Waals force and the pull-off distance is strongly reduced.
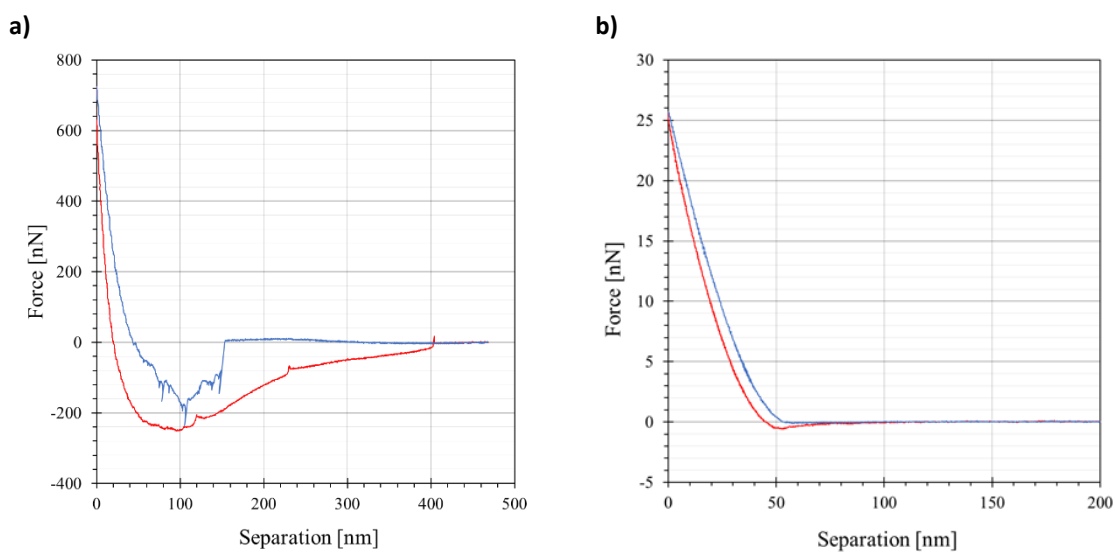
Figure 3.5 Force Distance curves acquired on a neat Pebax®1657 membrane in air (a) and in silicon oil (b) with a 2 µm tip radius. Blue: approaching, red: retraction curves.

The calculated Young's moduli are plotted in Figure 3.6. The histograms show the number of points in a given range of Young's modulus. All samples show a more or less wide distribution of the modulus due to the microphase separation of the multi-block copolymer. With the 2 μm tip, the neat Pebax and the sample with 10 wt% IL show a multimodal distribution of Young's modulus. With the small tip, all membranes show a clearly bimodal distribution, except for the samples with 30 and 40 wt% of IL. This is due to the similar dimensions of the tip on the one hand, and of the domains with different elasticity on the other hand, which are therefore probed individually. The higher overall values of the modulus with the small tip compared to the bigger tip are due to the higher sensibility of the small tip to the stiffness of the different domains. This behaviour is typically observed on materials that self-assemble in complex structures as individual collagen fibrils in corneas. [64,65] Even when measuring the softer area, the tip senses harder domains below the surface, whereas the larger tip really measures the average properties of the whole sample. This is at the same time a strength and a weakness of the technique and highlights the importance of using the right tip for quantitative analysis.
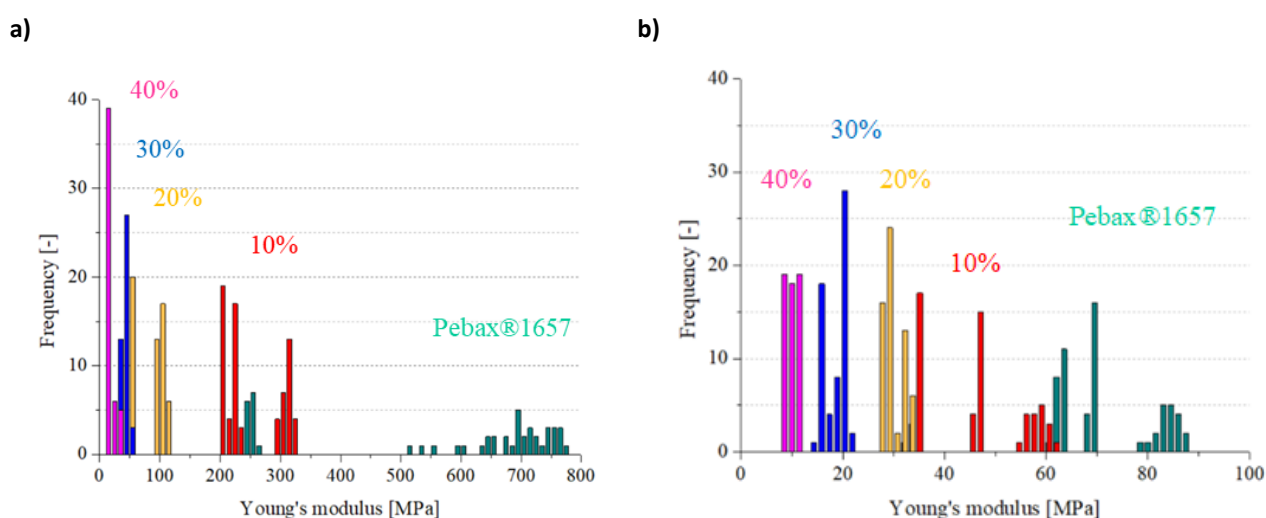
Figure 3.6 Frequency distribution of the Young's modulus of Pebax®1657 samples at different IL concentration, obtained with a tip radius of 10 nm (a) in 10 MPa intervals and a tip of 2 μm (b) in 1.5 MPa intervals.

For both tips, the Young's modulus decreases with increasing IL content due to plasticization of the polymer and reduction of the overall crystallinity upon dissolution of the IL in the polyether phase, as previously observed for similar systems.[11] Figure 3.7a shows the average values of the Young's modulus obtained by force spectroscopy as a function of the IL content. The modulus decreases exponentially with IL content. The Young's modulus measured with the nanometric tip is

about one order of magnitude higher than the one measured with the micrometric tip for low IL contents. The values approach each other for higher IL contents because the concentration of hard domains reduces.

3.3.3.2   Force spectroscopy vs tensile tests

The same samples were also subjected to traditional tensile tests, carried out at room temperature on a Zwick/Roell single column Universal Testing Machine, model Z2.5, equipped with a 200 N load cell. To avoid slipping of the sample, one of the clamp surfaces is convex and the other is flat. The rectangular specimens with a length of 5 cm and a width of 1 cm were tested at a relative deformation rate of 100% min^{-1} for the determination of Young's modulus and then with 500% min^{-1} until breakage. The average value and the standard deviation of the Young's modulus, the break strength and the maximum deformation were determined on a series of five or more samples.

The results show exactly the same trend and similar absolute values as the force spectroscopy measurements with the micrometric tip, which measures the average polymer properties (Figure 3.7b), confirming the interchangeability of the two techniques. This also confirms that there are no substantial differences in the surface properties, analysed by AFM Force Spectroscopy, and the bulk properties measured by the tensile tests. Indeed, being a rubber, Pebax® and the Pebax®/IL blend should be in the completely relaxed equilibrium state, in contrast to glassy polymers. As observed in the force spectroscopy measurements, the maximum deformation and the tensile strength both decrease with increasing IL content too due to the plasticization and decrease of crystallinity (Figure 3.7c,d). At higher IL content, the number of inter-chain interactions and entanglements decreases. Consequently, the membrane loses its mechanical strength. The modulus is around 100 MPa for the neat polymer and it is ten times lower for the membrane with 40 wt% of IL.
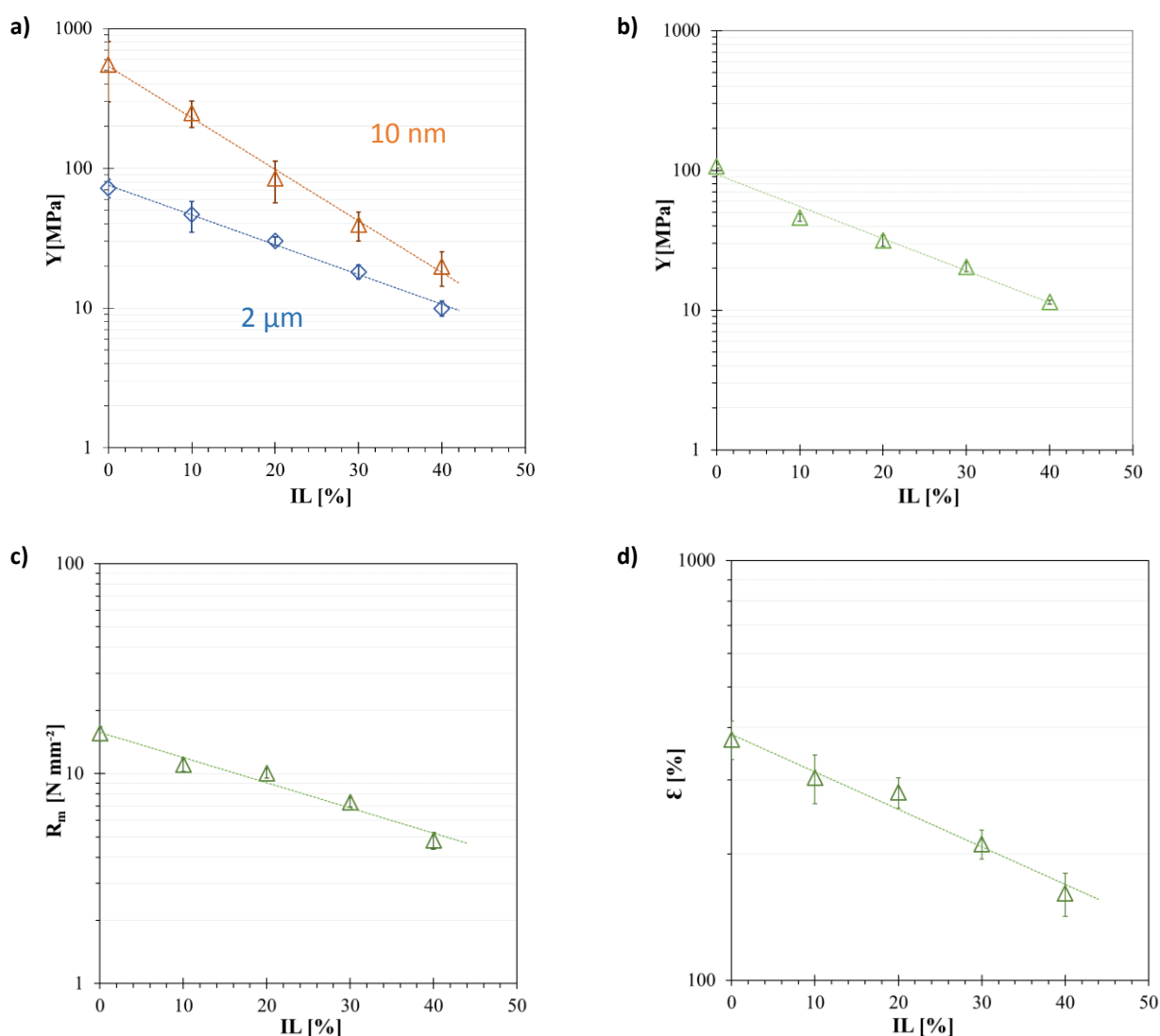
Figure 3.7 Young's module as a function of the ionic liquid content, as measured by force spectroscopy analysis with an AFM tip radius of 10 nm and 2 μm, respectively (a), and with tensile tests (b). Maximum break strength (c) and maximum deformation (d) as a function of the ionic liquid content in Pebax®1657. Errors bars are smaller than the symbols in some cases and represent the standard deviation of all measurements for each sample.

3.4 Conclusion

The aim of this study was to demonstrate that AFM force spectroscopy is an excellent alternative to tensile tests for the analysis of Young's modulus, even in the case of complex systems such as the present blends of an ionic liquid and a multi-block copolymer. The proposed Pebax®/IL membranes present a complex multiphase system with different local mechanical properties. Mechanical properties measured on three different scales are discussed. Measurements on micro- or macro scale provide information on the bulk properties; AFM force spectroscopy analysis on nano-scale

43

provides additional information on the local morphology. A good match between the mechanical properties measured by traditional tensile tests and by AFM force spectroscopy on micro scale is found, ensuring the reliability of the latter method for the characterization of small scale membrane samples. In all cases, an exponential decrease of Young's modulus with increasing IL content is found. The permeability and diffusion coefficients increase with increasing IL content, as a consequence of the lower crystallinity and the increased mobility of the polymer chains in the blend. There is no substantial difference between membranes with IL added in the casting solution or membranes with IL absorbed by soaking of neat Pebax® in excess IL. The Young's modulus measured by force spectroscopy on the AFM with the nanometric tip is about one order of magnitude higher at low IL content than the value measured with the micrometric tip, which is probably because the tip only senses effectively the harder domains in or below the membrane surface. The smaller tip furthermore detects a bimodal distribution of the modulus, due to the comparable dimensions of the polymer domains and the nanometric tip, probing the local properties.

Aging, gas permeation and mechanical properties in polymers of intrinsic microporosity. [1]

4.1 Introduction

As anticipated in the general introduction, another class of polymer materials, receiving most attention from the scientific community in view of their possible use of gas separation membranes, is represented by the polymers of intrinsic microporosity (PIMs). PIMs were first reported by Budd and McKeown [15,66] and have unique rigid and contorted macromolecular backbone structures which prevents an effective packing leading to interconnected, irregularly shaped free volume elements behaving like micropores (i.e., pores of diameter <2 nm according to IUPAC).[15,16] Thus, the term intrinsic microporosity was coined for such polymers as "a continuous network of interconnected intermolecular voids, which forms as a direct consequence of the shape and rigidity of the component macromolecules."[67] PIMs demonstrate attractive properties for membranes with a combination of very high permeability, good separation factor, good mechanical properties and capability to be solution-processed.[16] Like all glassy polymers with high fractional free volume, PIMs suffer from physical aging as a consequence of the nonequilibrium nature of the glassy state, leading to a slow relaxation and rearrangement of the molecular structure. Aging strongly depends on the previous processing and thermal history of the samples, and widely different treatments are reported in the literature to condition samples before the analysis, which may therefore lead to significant differences in the test results.[23] Gas permeation measurements are a very powerful technique to track the aging of membranes.[68] Aging leads to a decrease in permeability and for many glassy polymers a concurrent increase in selectivity generally proceeds in a manner nearly parallel to the upper bound lines.[23] In this chapter, the relationship between the transport properties and Young's modulus for films of polymers of intrinsic microporosity (PIMs) during physical aging are discussed. Physical aging is investigated using pure gas permeability and force spectroscopy. Results from different PIMs provided direct evidence that size selectivity is strongly correlated to the Young's modulus. The archetypal PIM-1 is used as a reference to allow the comparison of the mechanical properties measured using force spectroscopy, with data already reported in the literature using more traditional techniques. Furthermore, one representative ultrapermeable PIM (PIM-DTFM-BTrip) is subjected to both standard physical aging and to accelerated aging by thermal conditioning under vacuum to analyse the effect of possible conditioning protocols. This study of PIM aging provided greater understanding of the relationship between gas separation performance and mechanical properties. In addition, the study of the

permeability, diffusivity and solubility of the ultrapermeable PIM-TMN-Trip and PIM-BTrip, whose transport properties are used to update the Robeson upper bound, are analysed as a function of the temperature in a range from 25°C to 55°C. This analysis investigated how the transport parameters are affected by the temperature and by the dimension of the penetrant gas. The energetic parameters of permeability, diffusivity and solubility are calculated using Arrhenius-van't Hoff equations and compared with those of the archetypal PIM-1 and the poly(trimethylsilylpropyne) (PTMSP), the most permeable polymers used to design the upper bounds in 2008 and 1991 respectively. The last paragraph focuses on the study of the mechanical properties of the first ultrapermeable PIM with a 3D monomeric shape and its copolymer with PIM-1, and of a series of copolymers with different ratio of a novel PIM and PIM-1. This analysis deeply investigated the effect of copolymerization of two monomers with different stiffness on the total Young's modulus. These studies are of great practical interest because knowledge of the correlation between polymer structure, physical aging, mechanical and transport properties are necessary for the development of novel polymer materials for the next generation of membranes for gas separation.

4.2 Membrane conditioning via post-synthesis samples treatments

The polymers of intrinsic microporosity used in this thesis are: PIM-1,[15,69] PIM-2,[70] the ultrapermeable PIM-BTrip (**1**), PIM-TFM-BTrip (**2**), PIM-DTFM-BTrip (**3**), PIM-HMI-Trip (**4**) and PIM-TMN-Trip (**5**)[36,71] and the novel copolymers PIM-1/PIM-DBzMP and PIM-SBI-Trip [72] were synthesised by the group of Prof. Neil B. McKeown of the University of Edinburgh. Their structures are reported in Figure 4.1.

In order to reset the thermodynamic polymer history [73] and to remove traces of residual solvent after membrane preparation,[74–76] all membranes were soaked in methanol for one day and dried for another day at ambient conditions, while loosely pressed between two porous glass disks to maintain a flat shape and to allow the methanol removal via evaporation.
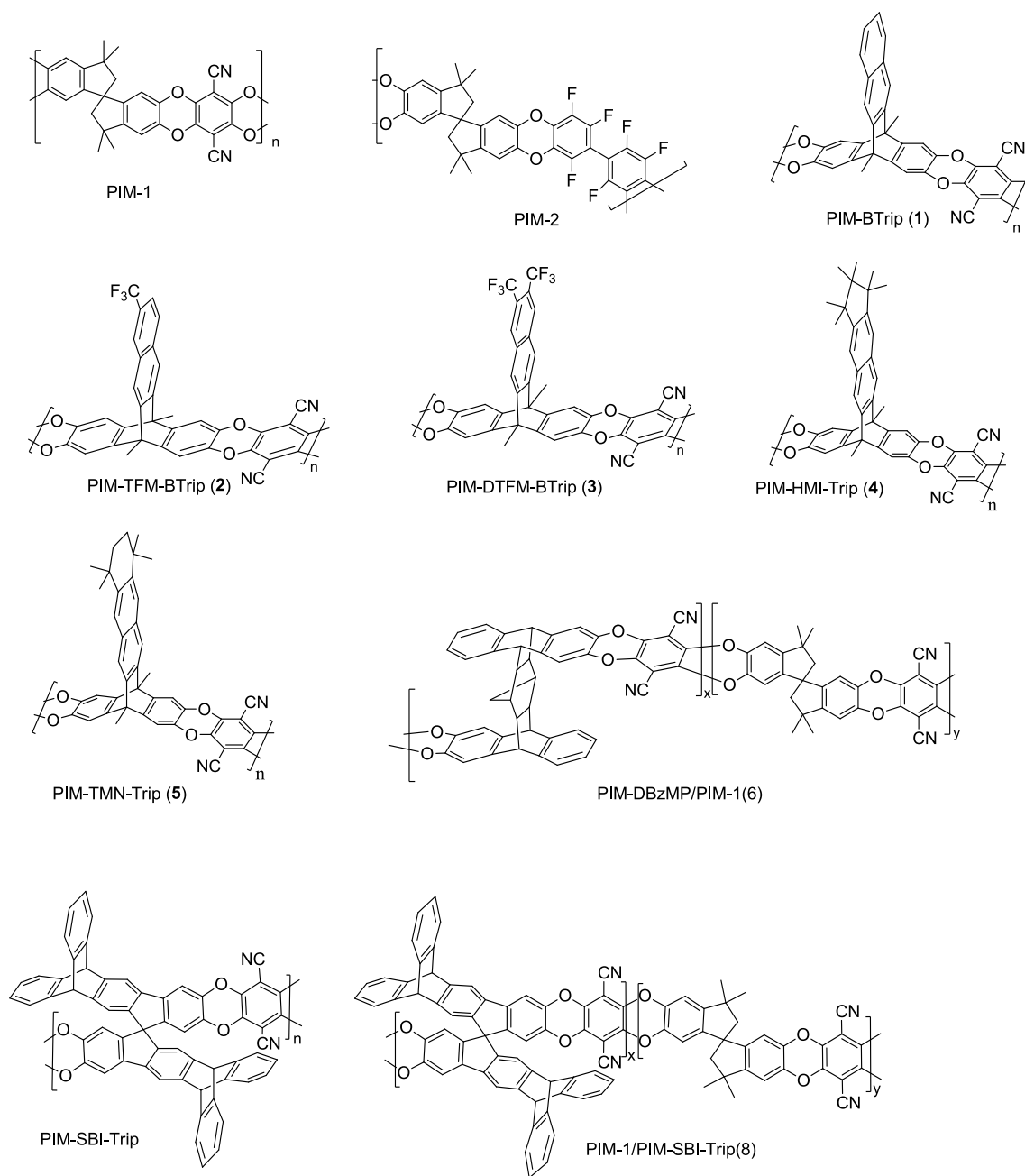
Figure 4.1 Structures of the PIMs discussed in this chapter.

Four equivalent samples of PIM-DTFM-BTrip were soaked in methanol and dried in air as above. Two of these were then further conditioned under vacuum at 140 °C in an attempt to accelerate the aging process. Among samples treated only in methanol and those thermally conditioned, one specimen was tested immediately and the other was aged for 30 days at ambient conditions before the first measurement. Table 4.1 reports all the membranes used in this chapter, as well as their different conditioning history.

Table 4.1 Membrane code, pre-measurement history, and thickness of the films studied in this work.

Polymer	Membrane code and history [a)	Thickness (µm)	Ref.
PIM-1	MeOH [b)	88	[21]
	+140°C_4h	85	[21]
	MeOH+aged 2219d [b)	91	[21]
PIM-BTrip	MeOH	160	[36]
PIM-TFM-BTrip	MeOH	176	[36]
PIM-DTFM-BTrip	MeOH	106	[21]
	+140°C_4h	149	[21]
	MeOH_30d	156	[21]
	+140°C_4h_30d	186	[21]
PIM-HMI-Trip	MeOH	135	[36]
PIM-TMN-Trip	MeOH	166	[36]
PIM-2	MeOH	60,9	[70]
	+140°C_4h		[70]
	MeOH_60d	60,9	[70]
	+140°C_4h_60d		[70]
PIM-1/PIM-DBzMP	MeOH		[in preparation]
PIM-SBI-Trip	MeOH		[in preparation]
	+140°C_4h		[in preparation]
PIM-1/SBI-Trip	MeOH		[in preparation]
	+140°C_4h		[in preparation]

[a) Membrane codes representing their preparation history:

MeOH: Membrane soaked in methanol, dried in air for 24 h, and tested immediately.

MeOH_30d: Membrane soaked in methanol, dried in air for 24 h, and stored for 30 days before testing.

+140°C_4h: Membrane soaked in methanol, dried in air for 24 h, heated at 140 °C for 4 h, and tested immediately.

+140°C_4h_30d: Membrane soaked in methanol, dried in air for 24 h, heated at 140 °C for 4 h, and stored for 30 days before testing.

MeOH+aged 2219d: Membrane soaked in methanol, dried in air for 24 h, and aged for 2219 days before testing.

[b) Different samples

4.2.1 Correlation between the mechanical and gas transport properties in PIMs

In this paragraph, the correlation between the mechanical and gas transport properties was investigated via a systematic study on five ultrapermeable PIMs (**1**-**5** in Figure 4.1). Measurements were performed at room temperature in air. For each membrane 60 FD curves were recorded at a scan rate of 400nm s^{-1}. The FD curves were acquired in three different areas of each membrane, using a spherical tip.
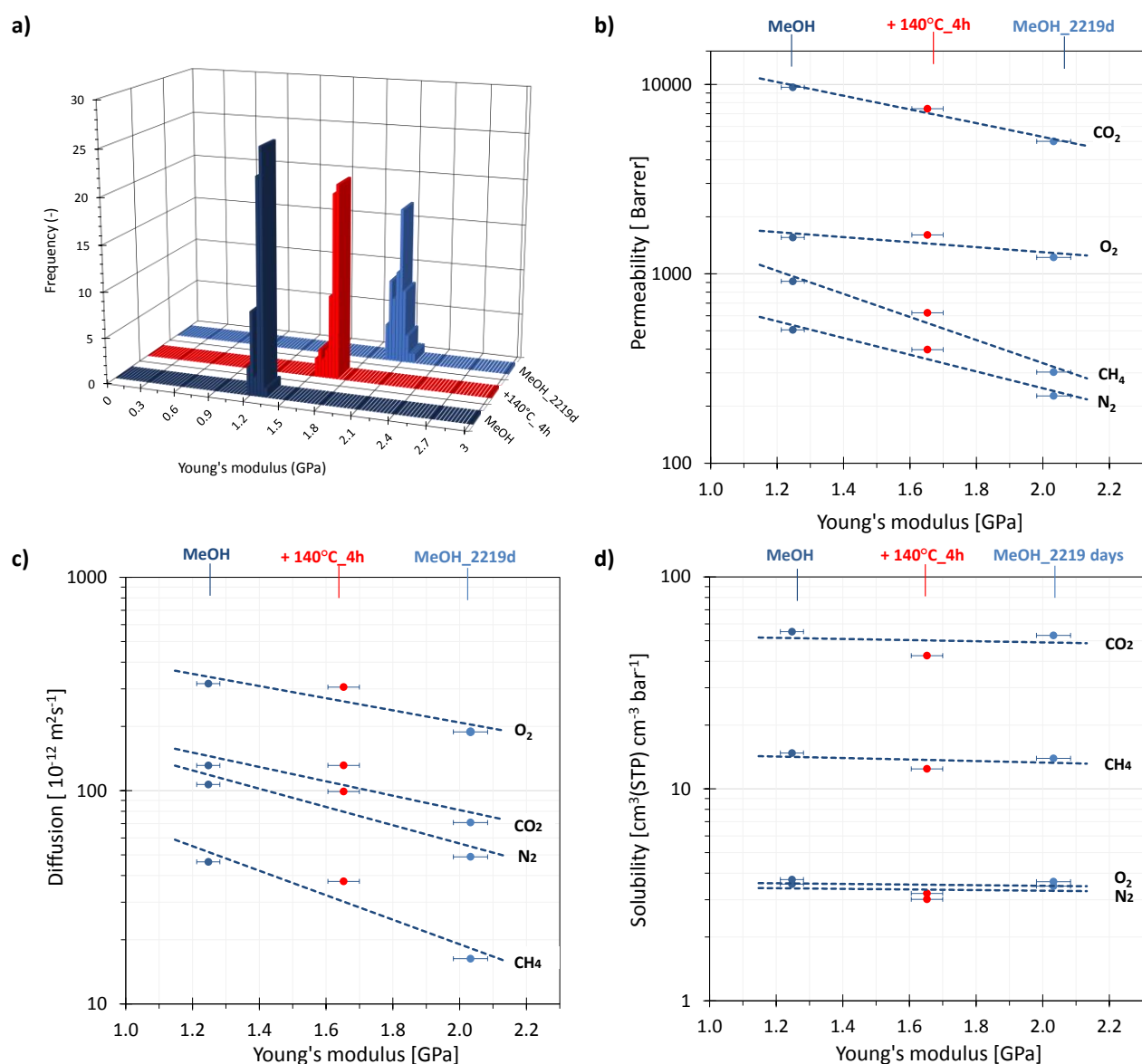
Figure 4.2 Frequency distribution of Young's modulus (a) of a PIM-1 sample after MeOH treatment (dark blue) and subsequent thermal conditioning at 140 °C under vacuum (red) or after 2219 days of physical aging from the MeOH treatment (light blue). Correlation of the permeability (b), diffusion (c) and solubility (d) coefficients of O_2, N_2, CH_4 and CO_2 with Young's modulus of the samples. The symbol and the horizontal error bar show the average modulus and the standard deviation of Young's modulus, respectively, calculated from the 60 individual measurements represented in the frequency distributions.
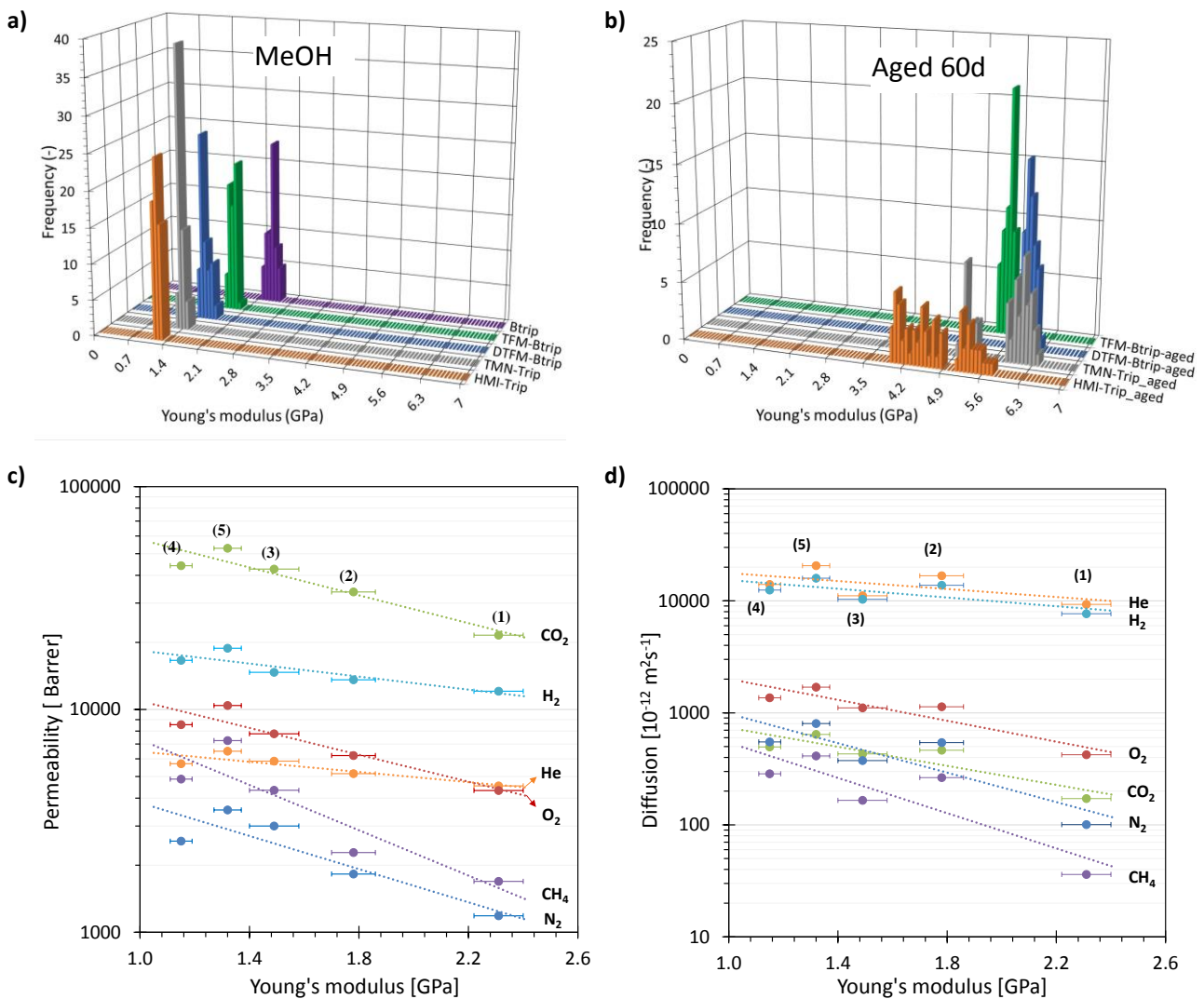
Figure 4.3 Frequency distribution of Young's modulus of the fresh ultrapermeable PIM-BTrip (1), PIM-TFM-BTrip (2), PIM-DTFM-BTrip (3), PIM-HMI-Trip (4) and PIM-TMN-Trip (5) samples tested after methanol treatment and dried in air for 24 h (a) and of the same samples after 60 days of aging (b). Plot of the correlation of the permeability coefficient[36] (c) and of the diffusion coefficients (d) with Young's modulus of the polymers. The symbol and the horizontal error bar (shown only in the CO_2 series for clarity) show the average value and the standard deviation of Young's modulus, respectively, calculated from the 60 individual measurements represented in the frequency distributions.

Figure 4.2a shows the frequency distribution of Young's modulus of three PIM-1 films. The value of the fresh sample (dark blue) is in good agreement with the data available in the literature from different techniques (1 - 1.7 GPa) [77–80] and confirms the validity of the AFM force spectroscopy method. The average value depends strongly on the sample history, as can be seen from the modulus of the film that was thermally conditioned after soaking in methanol (red), which shifts from 1.25 ± 0.03 GPa to 1.66 ± 0.05 GPa. The modulus of the membrane that was soaked in methanol and then aged for 2219 days under ambient conditions (light blue) further increases to 2.03 ± 0.05

GPa. Figure 4.2b shows the correlation between permeability and the average Young's modulus of PIM-1. The permeability decreases with increasing Young's modulus, independently of the sample history (accelerated thermal aging or natural aging), and this trend is mostly due to a decrease in the diffusion coefficient (Figure 4.2c). Instead, the gas solubility is virtually unaffected (Figure 4.2d). Figure 4.3a shows the frequency distribution of Young's modulus of the samples after methanol treatment and Figure 4.3b shows the same samples, with the exception of PIM-BTrip, after 60 days of aging. Aged PIM-BTrip film proved unsuitable for measurement due to the formation of shallow surface cracks with similar dimensions as that of the AFM tip (Figure 4.4). In all cases for the 60 days aged films, the modulus increases to much higher values than those of a 2219 days aged PIM-1 used as a reference for long aging. This suggests that in the state with the highest excess free volume, i.e. just after MeOH treatment, the polymer has a relatively soft structure, and that the aging leads to a denser packing arrangement with an increase in the bulk stiffness of the materials, along with a decrease in permeability.
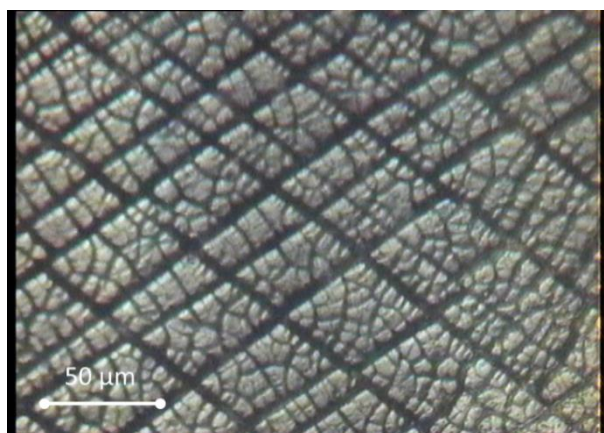
Figure 4.4 Optical micrographs of the membrane surfaces of the ultrapermeable PIMs.

For all gases, the permeability decreases with increasing Young's modulus (Figure 4.3c) in a roughly exponential fashion, with only PIM-HMI-Trip falling slightly below the trend. This correlation is interesting in view of Freeman's analysis of the Robeson Upper bound relationship,[14] and in view of the studies claiming that for instance thermally rearranged (TR) polymers owe their molecular sieve-like size selectivity to the increased rigidity of the polymer after the thermal rearrangement.[81] The decrease in permeability upon aging is usually strongest for the larger gas species and this is correlated with increased size-selectivity.[42] Similarly, diffusivity decreases with Young's modulus in a similar fashion when a sufficiently wide range of modulus values is covered,

but with some deviations from the trend line for the individual polymers (Figure 4.3d), suggesting that the correlation between diffusivity and Young's Modulus is not as strong as that between permeability and Young's Modulus. The deviation from the trend line most likely occurs because sample modulus is not the only factor determining the size selectivity, but also the total free volume and its size distribution. Depending on the gas type and sample history, the standard deviation in the permeability is always below 18%, but typically it is in the range of the symbol size in the graphs,[36] and therefore it does not affect the observed trends or the conclusions of this study.

4.2.2 Effect of sample conditioning on the transport properties for PIM-DTFM-BTrip

For a better understanding of the effect of the sample conditioning and physical aging on the transport properties, four identical samples of PIM-DTFM-BTrip were treated in different ways. All were soaked in methanol but only two were further thermally treated at 140°C for hours. Figure 4.5 shows the transport properties for a series of gases upon aging of a MeOH treated sample of PIM-DTFM-BTrip and of a sample evacuated for 4h at 140 °C. After the initial treatment, the permeability gradually decreases as a function of aging time for all gases in both films, with lower values for the thermally conditioned sample due to the thermally-activated accelerated physical aging (Figure 4.5a). The decrease in permeability is associated with a weak increase in selectivity (Figure 4.5b), following the same trend previously described for physical aging of other PIMs and glassy polymers.[68,82] This trend is clearer on the Robeson plots (Figure 4.7). Diffusivity follows the same trend as permeability (Figure 4.5c), whereas the solubility is hardly affected by either aging or thermal treatment of the samples (Figure 4.5d). Thus, aging affects the mobility and rearrangement of the polymer chains, their packing density and the overall free volume, without substantial changes in the affinity for the gas. For both samples, the diffusion coefficients decrease in the order $O_2 > CO_2 > N_2 > CH_4$, according to their effective gas diameters.[48] This is typical for nearly all dense membranes for which transport is governed by the solution-diffusion transport mechanism, and the effect is particularly strong for PIMs, known for their strong size-selective character.[19,42]
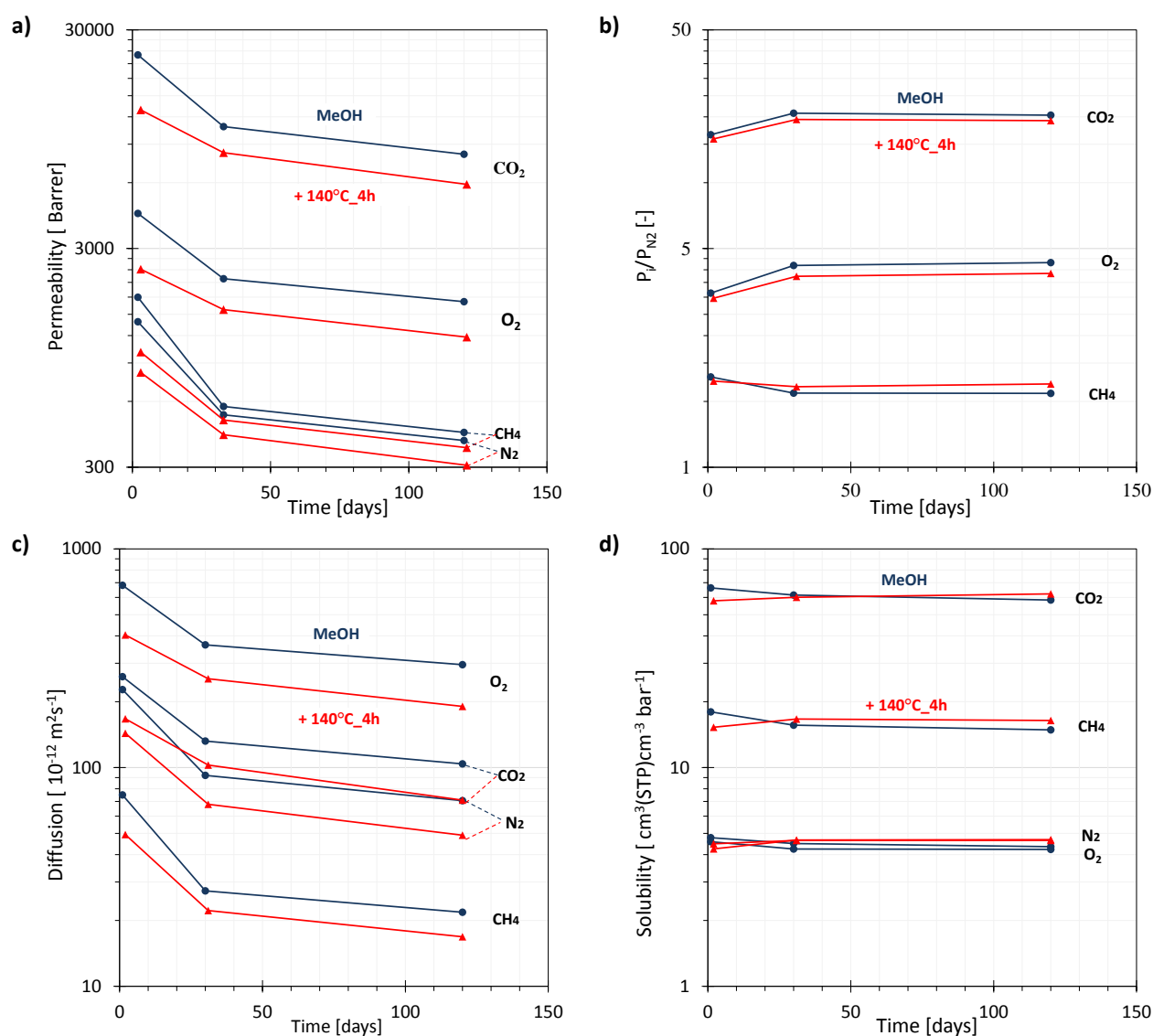
Figure 4.5 Transport properties of O_2, N_2, CH_4 and CO_2 upon aging of the PIM-DTFM-BTrip (3) membranes after methanol soaking (blue, •) and after methanol soaking and thermal conditioning at 140 °C for 4 h (red, ▲): permeability (a), permselectivity (b), diffusivity (c) and solubility (d). (Note that the dotted lines link the curves with the gas name. 1 Barrer = 10^{-10} $cm^3_{(STP)}$ cm cm^{-2} s^{-1} $cmHg^{-1}$).

Interestingly, aging seems to be triggered by the permeability measurement itself, because the samples tested 30 days after the MeOH treatment, with or without conditioning at 140 °C, show the same P and D as the samples immediately tested, and much higher P and D than the samples that were tested and then aged for 30 days (Figure 4.6). This suggests that residual methanol reduces aging until it is removed by the vacuum applied on the membrane before the permeability tests. However, it has been noted previously that repetitive exposure to methanol vapour cannot completely suppress physical aging.[83] Thus, it is mainly associated to MeOH that is present from the beginning.
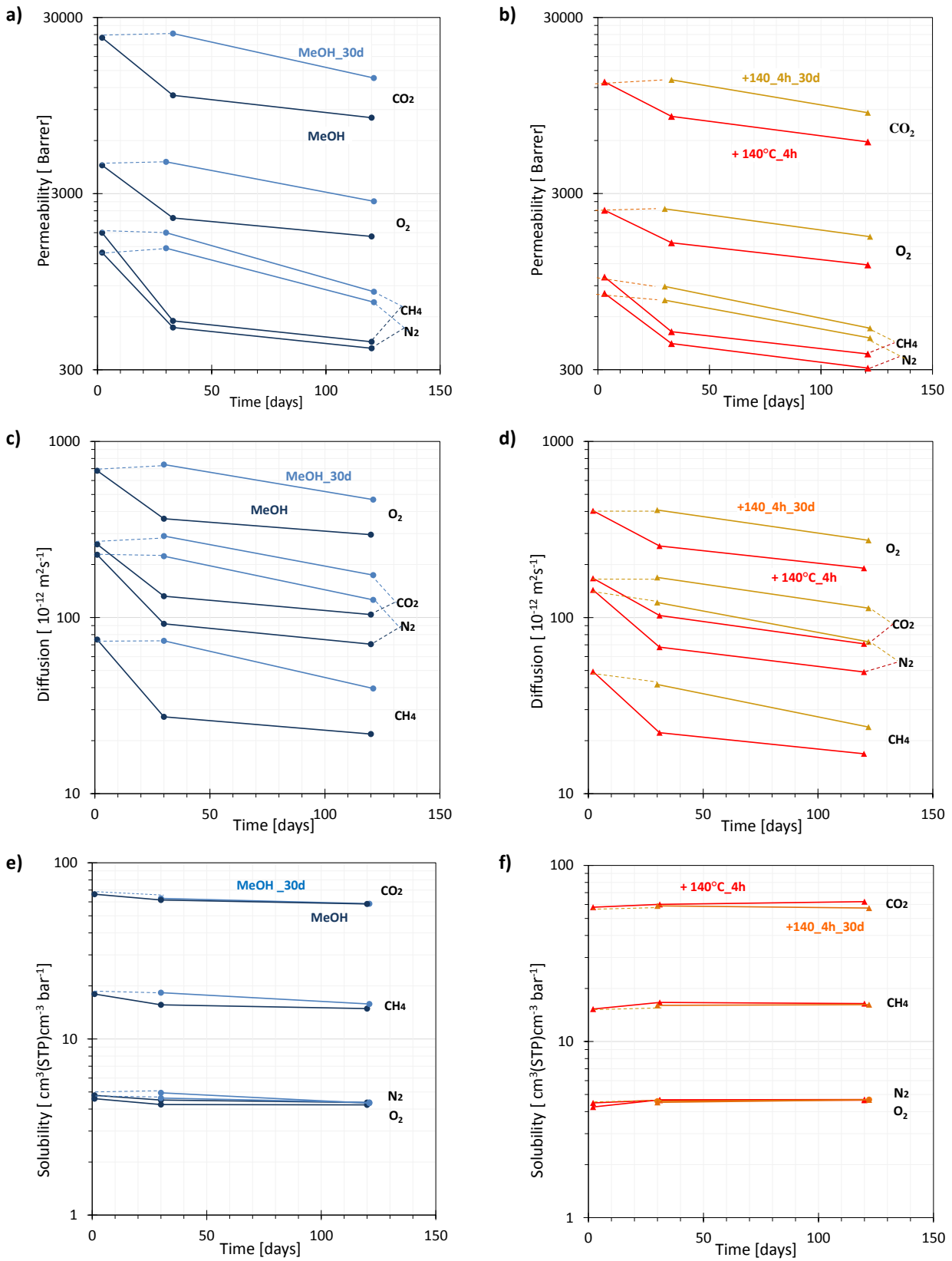
Figure 4.6 Permeability (a), diffusion (b) and solubility (c) of O_2, N_2, CH_4 and CO_2 of PIM-DTFM-BTrip upon aging of sample MeOH in blue (•), MeOH_30d in light blue (•), +140°C_4h in red (▲), and +140°C_4h_30d in orange (•).

The Robeson plots of PIM-DTFM-BTrip for four relevant gas pairs CO_2/CH_4, CO_2/N_2, O_2/N_2, and He/N_2 (Figure 4.7a-d) show that aging generally leads to a decrease in the permeability and an increase in selectivity, more or less parallel to the Robeson upper bound,[84] A similar trend was observed for all members of the benzotriptycene-based PIM family.[36] The strong increase in He/N_2 selectivity (Figure 4.7d) evidences a distinct size-sieving ability of the polymer, which further increases upon aging. Instead, the thermal treatment at 140 °C accelerates aging and reduces the permeability of the samples, but without the desired increase in selectivity. This makes thermal treatment less attractive to optimize and to stabilize the membrane performance.
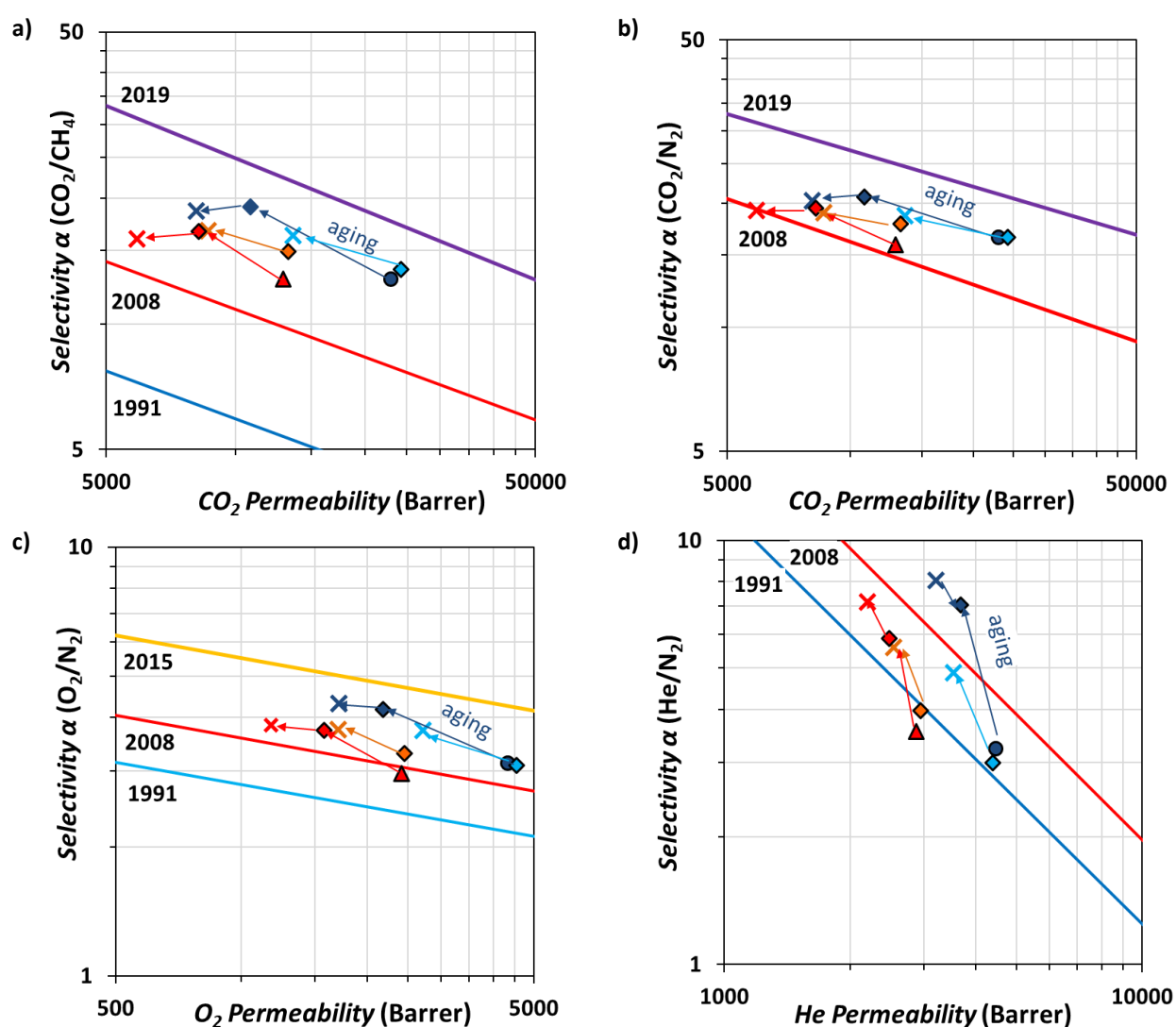
Figure 4.7 Robeson plots of PIM-DTFM-BTrip (3) for CO_2/CH_4 (a), CO_2/N_2 (b), O_2/N_2 (c), and He/N_2 (d) with the 1991 upper bounds indicated by a blue line, 2008 by a red line and those proposed for 2015 by yellow lines. Blue symbols show the data for the sample MeOH (•) and subsequently aged (30d (♦), 120d (✕)). Light blue symbols show the data for the sample MeOH_30d and subsequently aged (30d (♦), 120d (✕)). Red symbols show the data for the sample 140 °C_4h (▲), and subsequent aging (30d (♦), 120d (✕)). Orange symbols show the data for the sample 140°C_4h_30d and subsequent aging (30d (♦), 120d (✕)).

56

4.2.3 Effect of Physical Aging on the Mechanical Properties

The sample history of PIM-DTFM-BTrip also strongly affects its mechanical properties, as witnessed by a significant increase of Young's modulus after different conditioning steps. Figure 4.8 shows the frequency distribution of Young's modulus of the membrane only soaked in methanol (a), and the one further thermally conditioned (c). The three distributions for each sample represent the fresh, the 33 days aged, and the 120 days aged sample, respectively, with the brightest colour for the longest aging. In all cases, the average Young's modulus increases with aging time.
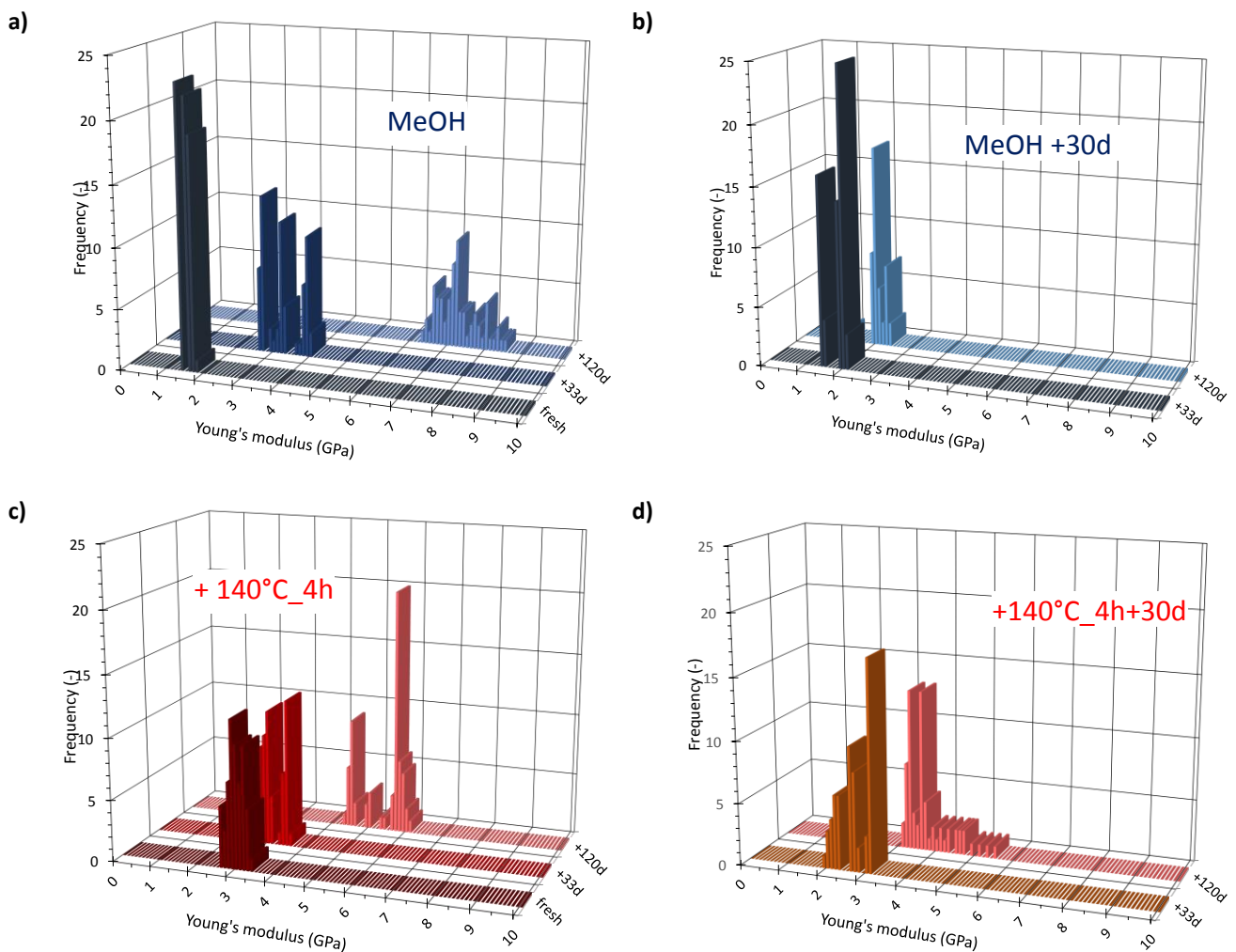
Figure 4.8 Effect of physical aging and post treatments on Young's modulus of PIM-DTFM-BTrip (3) films after MeOH treatment (a), after MeOH treatment and 30 days of aging MeOH_30d (b), after conditioning at 140 °C (c) and after conditioning at 140 °C and 30 day of aging. The groups in the charts represent the frequency distribution of the samples after different aging time.

Literature studies suggest that normal aging occurs predominantly at the surface of the film due to the enhanced mobility near the surface or to the diffusion of free volume toward the surface of the film, allowing the polymer at the surface or in thin films to reach a lower free volume state more quickly than bulk samples,[23,85] and creating a concentration gradient of fractional free volume near the surface.[73,86] The thermal conditioning of the membrane leads to a higher initial modulus but slower further increase over time, consistent with the thermal treatment initially accelerating aging and stabilizing the mechanical properties. This suggests that thermally induced accelerated aging occurs throughout the bulk of the polymer film, as a trade-off between increased thermal motion at elevated temperature and increased free volume due to thermal expansion. Remarkably, for both the fresh MeOH treated sample and the heat-treated sample, the permeability (Figure 4.6) and Young's modulus (Figure 4.8 b, d) change much less upon storage of the samples for 30 days without prior testing, than it does upon aging for 30 days after immediate testing. This suggests that the alternating vacuum and permeation of the samples actually triggers or accelerates the aging process.

4.2.4 Correlation between Gas Transport and Polymer Film Rigidity for PIM-DTFM-BTrip

The correlation between the gas transport parameters and Young's modulus of the methanol treated samples of PIM-DTFM-BTrip, shows that the permeability decreases with increasing Young's modulus (Figure 4.9a) and this is due to a decrease in the diffusion coefficient (Figure 4.9c), consistent with the behaviour observed for PIM-1 and for the five different samples in section 4.2.1. Solubility is not correlated with the mechanical properties and remains virtually constant (Figure 4.9e). This correlation of P and D with Young's modulus is not limited to the MeOH treated sample but it is common for all samples with different histories (Figure 4.9b,d and f). The observed correlation shows a general trend, almost independent of the specific sample history (Figure 4.10). The stiffening of the samples on aging hinders the diffusion of the penetrants though the membrane, particularly the larger gas molecules.
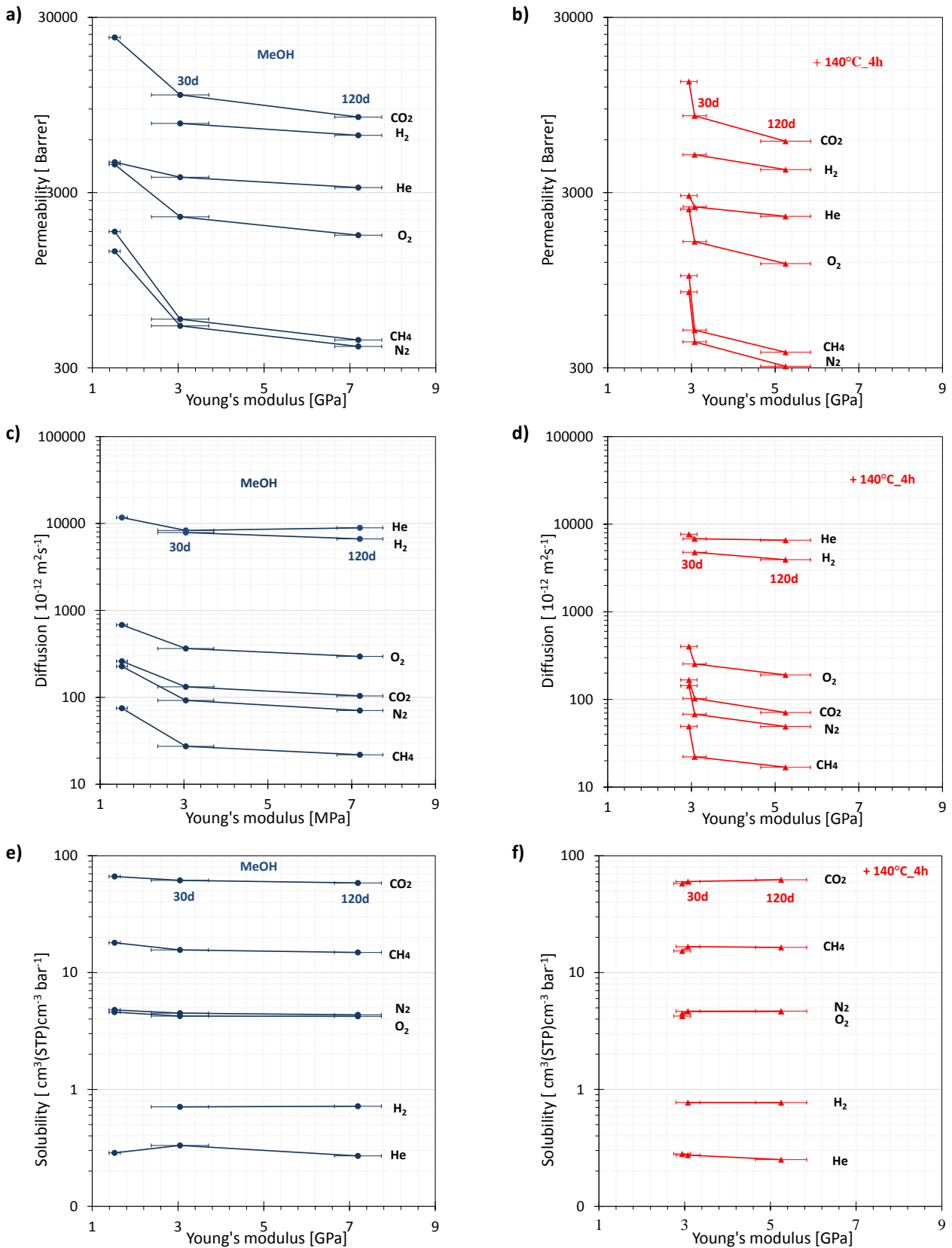
Figure 4.9 Correlation between Young's modulus and permeability (a,b), diffusion coefficient (c,d) and solubility (e,f) for O_2, N_2, He, H_2, CH_4 and CO_2 in the freshly prepared samples (blue, •) and samples treated at 140 °C under vacuum for 4 h.(red, ▲) of PIM-DTFM-BTrip (3) after MeOH. The symbol and the horizontal error bar represent the average modulus and the standard deviation, respectively, calculated from the 60 individual measurements.
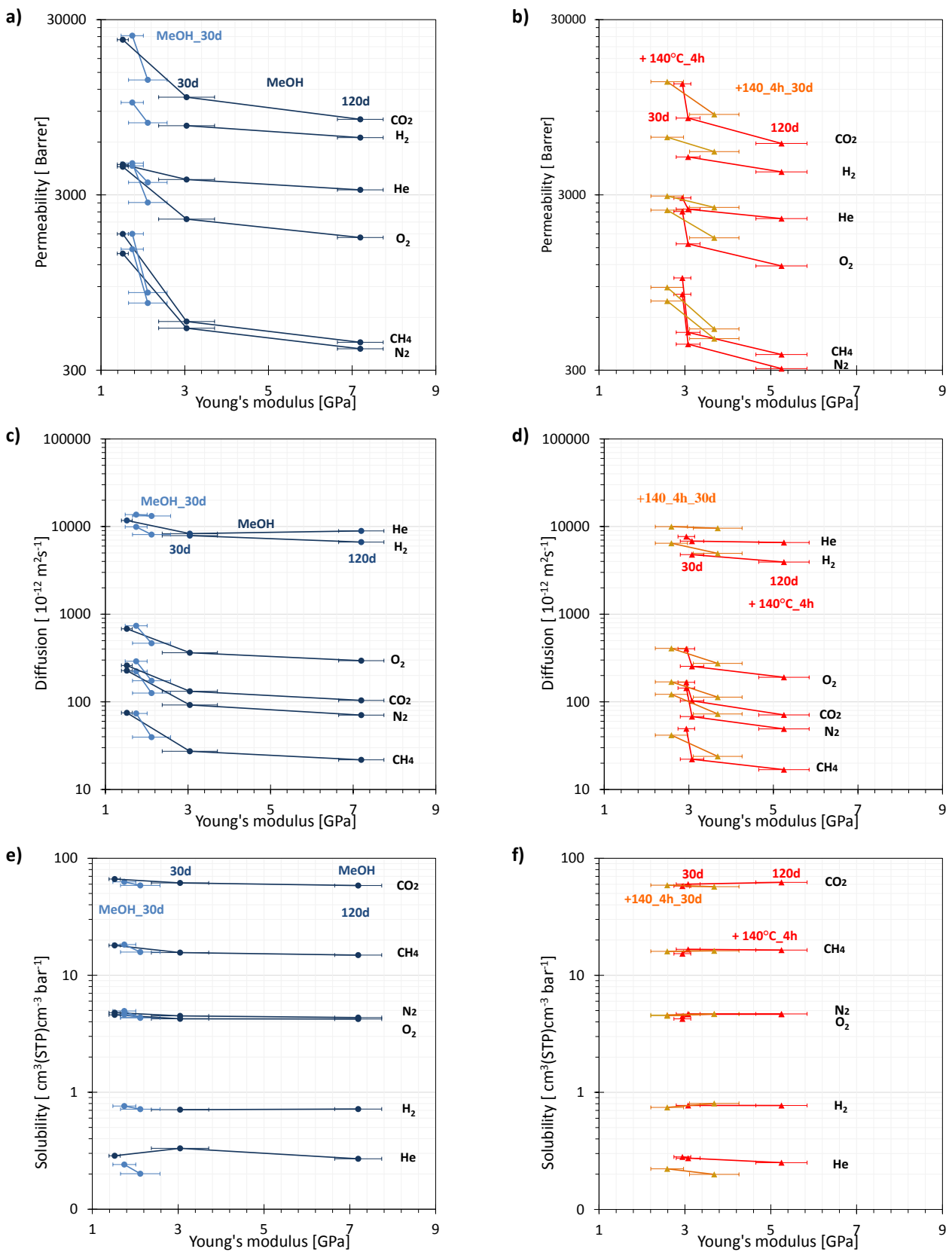
Figure 4.10 Permeability (a,b), diffusion coefficient (c,d) and solubility (e,f) of O_2, N_2, CH_4, He; H_2 and CO_2 as a function of Young's modulus of PIM-DTFM-BTrip sample MeOH in dark blue (●), MeOH_30d in light blue (●), +140°C_4h in red (▲), and +140°C_4h_30d in orange (▲).

At the same time, the decreased chain mobility leads to an increase in the energetic selectivity, increasing the size-sieving properties of the materials, and then the overall selectivity, consistent with a previous study on temperature dependent measurements.[19] The size-selectivity is related to the ability of a gas molecules to pass through tight constriction points between free volume elements formed by the polymer packing.

Figure 4.12a shows the frequency distribution of Young's modulus of two fresh PIM-2 membranes, one soaked in methanol, and the one further thermally conditioned. Both were additionally tested after 60 aging days. The thermal conditioning of the membrane leads to a higher initial modulus, and in both cases, the average Young's modulus increases with aging time, confirming the discussion made for the polymer PIM-DTFM-BTrip in section 4.2.3.
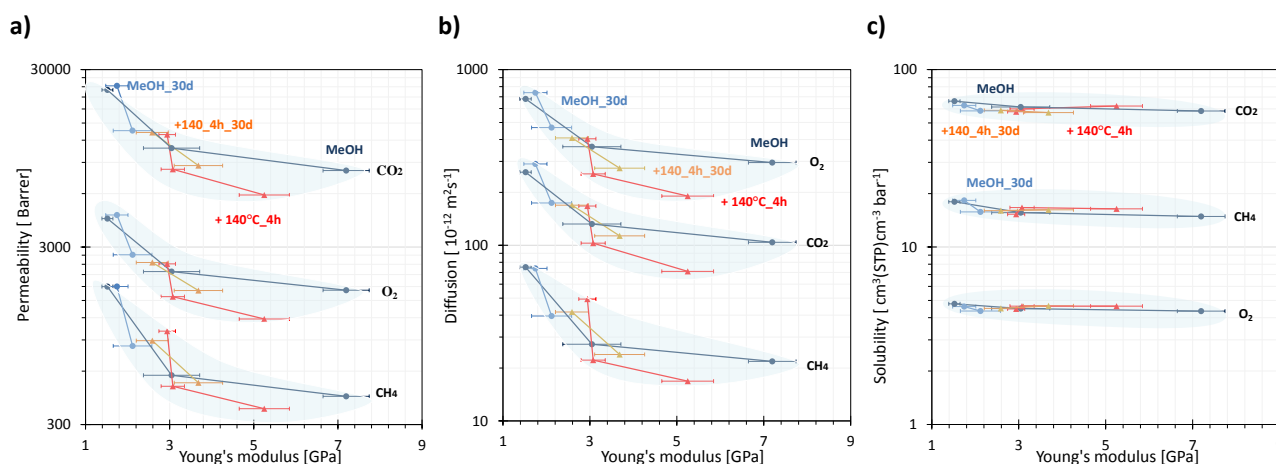
Figure 4.11 Master plot of the permeability (a), diffusion coefficient (b) and solubility (c) coefficients of O_2, CH_4 and CO_2 as a function of Young's modulus for all PIM-DTFM-BTrip (3) samples with different histories (see sample codes in Table 4.1). The lines connect the same samples with different ages.

Comparison of the PIM-1 data with those of structurally different and partially fluorinated PIM-2 reveals that PIM-2 has a higher Young's modulus and, although its permeability vs. modulus falls on the PIM-1 trend for CO_2 and O_2, its permeability is substantially higher for CH_4 and N_2 (Figure 4.12b). This suggests that the correlation between Young's modulus and the transport properties is accurate only for structurally similar polymers. Moreover, during aging also other effects could take place such as a decreasing of the free volume, a parameter that also influences the permeability and the selectivity. This is a well-known phenomenon for PIMs and has been demonstrated in various studies on PIMs and PIM copolymers.[73,87,88] In Table 4.2 are reported the Membrane Young's modulus discussed in the previous paragraphs.
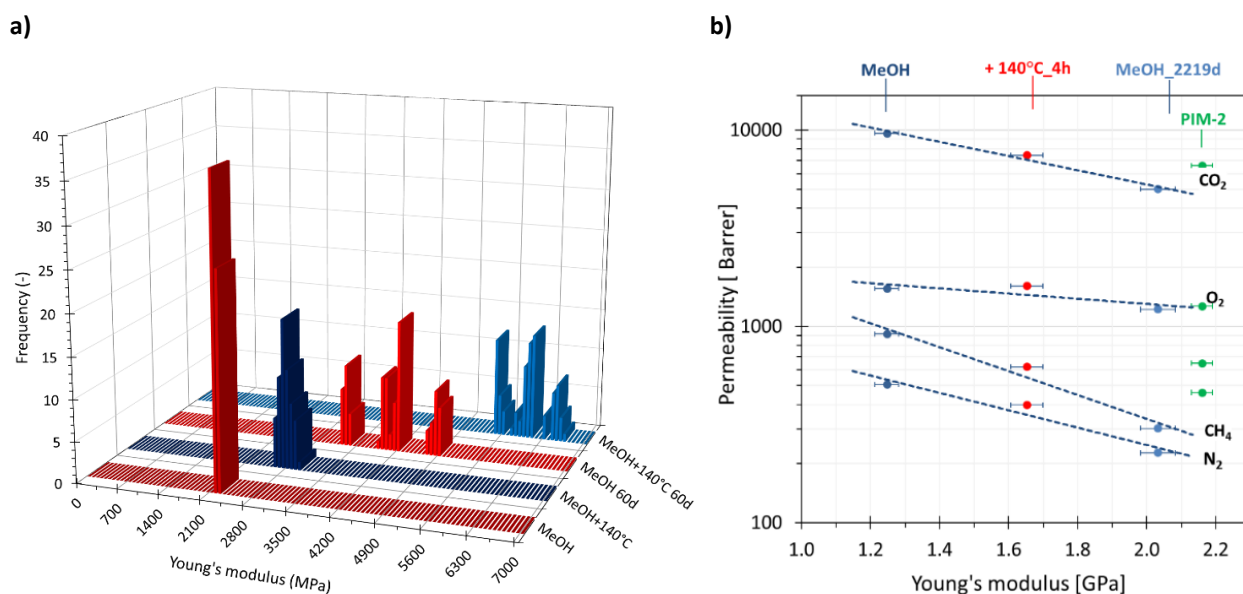
Figure 4.12 Comparison of PIM-1 from Figure 2.1 with data of fluorinated polymer PIM-2 after the MeOH soaking step (green series),[70] showing reasonable to good correspondence for CO_2 and O_2, but rather strong deviation of CH_4 and N_2 from the trend.

Table 4.2 Membrane Young's modulus and standard deviation

Polymer	Treatments	Aging [days]	Young's modulus [Mpa]	St.Dev [Mpa]	Ref.
PIM-1	MeOH	fresh	1247	35	[21]
		2219	2032	51	[21]
	+140°C_4h	fresh	1653	47	[21]
PIM-BTrip	MeOH	fresh	2312	91.8	[21]
PIM-TFM-BTrip	MeOH	fresh	1780	75.2	[21]
		60	5395	94.4	[21]
PIM-DTFM-BTrip	MeOH	fresh	1520	131	[21]
		33	3184	500	[21]
		120	7195	548	[21]
	+140°C_4h	fresh	2934	199	[21]
		33	3075	278	[21]
		120	5273	587	[21]
PIM-HMI-Trip	MeOH	fresh	1154	43.8	[21]
		60	4633	560.2	[21]
PIM-TMN-Trip	MeOH	fresh	1319	46.7	[21]
		60	5714	489.8	[21]
PIM-2	MeOH	fresh	2161	30	[70]
		60	4026	556	[70]
	+140°C_4h	fresh	2723	100	This work
		60	5960	357	This work

4.2.5 *Effect of Physical Aging on the Mechanical Properties in Copolymers*

In this paragraph, the mechanical properties of copolymers with the archetypal PIM-1 and the PIM-DBzMP or the PIM-SBI-Trip are assessed considering the different ratio between monomers and the effect of physical aging. PIM-DBzMP and PIM-SBI-Trip are novel, yet unpublished PIMs and their chemical structures are reported in Figure 4.1.

4.2.5.1 *PIM-DBzMP/PIM-1 copolymers*

Four PIM-DBzMP/PIM-1 membranes, with different amount of the DBzMP monomer, are tested using force spectroscopy to evaluate the effect of the different amounts on the mechanical properties. Figure 4.13 shows the Young's moduli frequency distribution of fresh methanol-soaked (a) and aged (b) membranes having different DBzMP:PIM-1 ratio: 10:90, 25:75, 50:50 and 75:25.
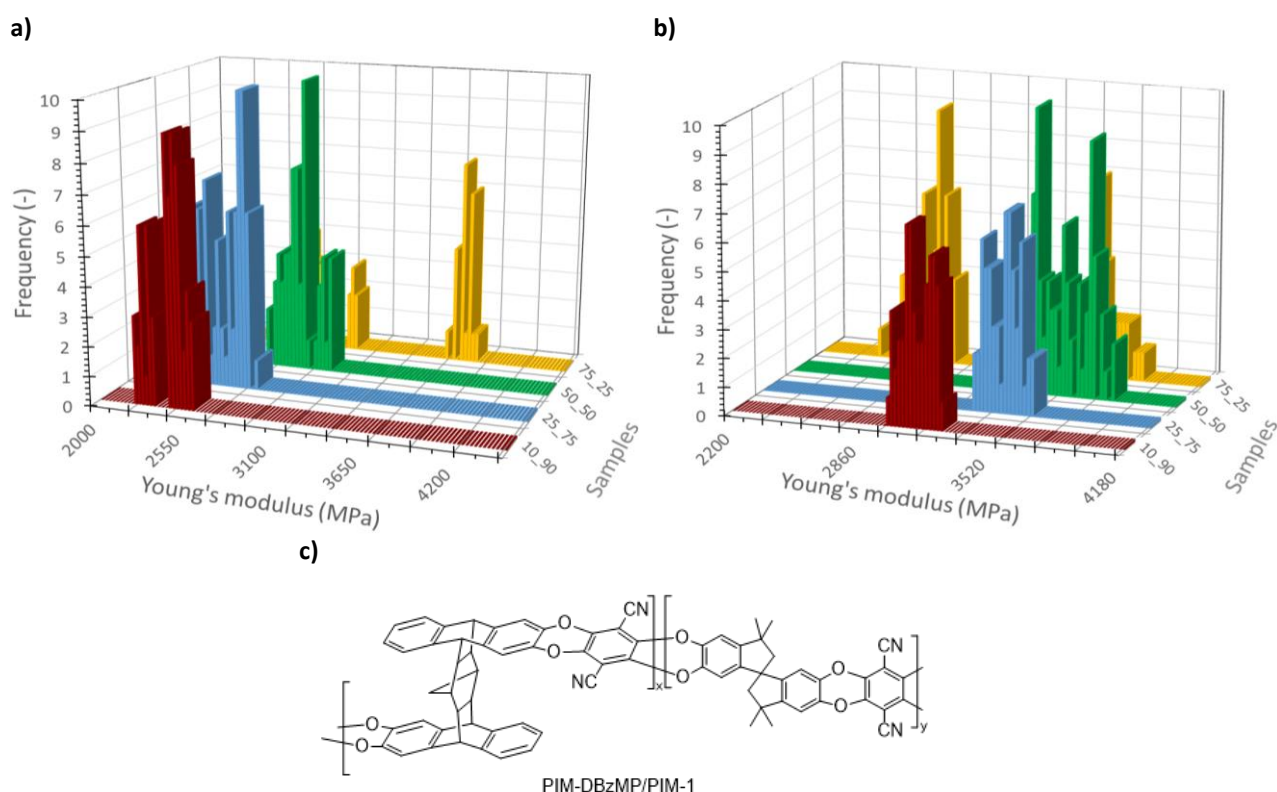
Figure 4.13 Frequency distribution of the Young's moduli of the PIM-DBzMP/PIM-1 fresh membranes (a) and the membranes aged for 144 days (b). The structure is shown in figure c.

All samples show a multimodal distribution of the Young's modulus because of sample heterogeneity, probably due to phase separation process at the microscale. Clearly, the higher the DBzMP content in the copolymer, the higher the Young's modulus (Table 4.3).

Table 4.3 Young's modulus of PIM-1, PIM-DBzMP/PIM-1, PIM-SBI-Trip and copolymer PIM-1/ PIM-SBI-Trip. In brackets are reported the aged values of 144 days.

Polymer	Composition (wt%:wt%)	Young's modulus [MPa]	Standard Dev. [Mpa]
PIM-1	100	1247[21]	35[21]
	100	2032**[21]	51 **[21]
PIM-DBzMP/PIM-1	10:90	2422	110
	10:90	(3141)	(78)
	25:75	2554	145
	25:75	(3434)	(84)
	50:50	2873	111
	50:50	(3588)	(151)
	75:25	3823-2806*	49-134*
	75:25	(3673-2743)*	(104-95)*
PIM-SBI-Trip	100	2004	53
PIM-1/ PIM-SBI-Trip	50:50	1790	83

*different values in different areas
** aged 2219 days

All samples have a significantly higher modulus than pure PIM-1, reported in Figure 4.2a. The modulus of the fresh samples with 90% PIM-1 is around 2400 MPa and it further increases to about 3800 MPa for the one with highest DBzMP fraction. During aging, the rigidity increases for all samples, similarly to the trends in the homopolymer PIMs, with exception for the sample with composition 75:25. Its average modulus seems to remain constant, but the measurements are strongly affected by the clear bimodal distribution of Young's modulus, due to the presence of areas with a different stiffness.

In SEM image of the sample 75:25 surface is not possible to observe phase separation or distinguish different domains (Figure 4.14). In the cross-section image, instead, microfractures very close to the sample surface with size comparable to AFM tip are visible. In this perspective, the bimodal distribution of the Young's moduli for the sample could be explained. For all the other samples, the surfaces appear homogeneous, and the cross sections reveal a dense morphology. By zooming a secondary mesoscale porosity, typical of PIMs is appreciated (Figure 4.14). [79]

SURFACE   CROSS SECTION

75:25

50:50

25:75

10:90
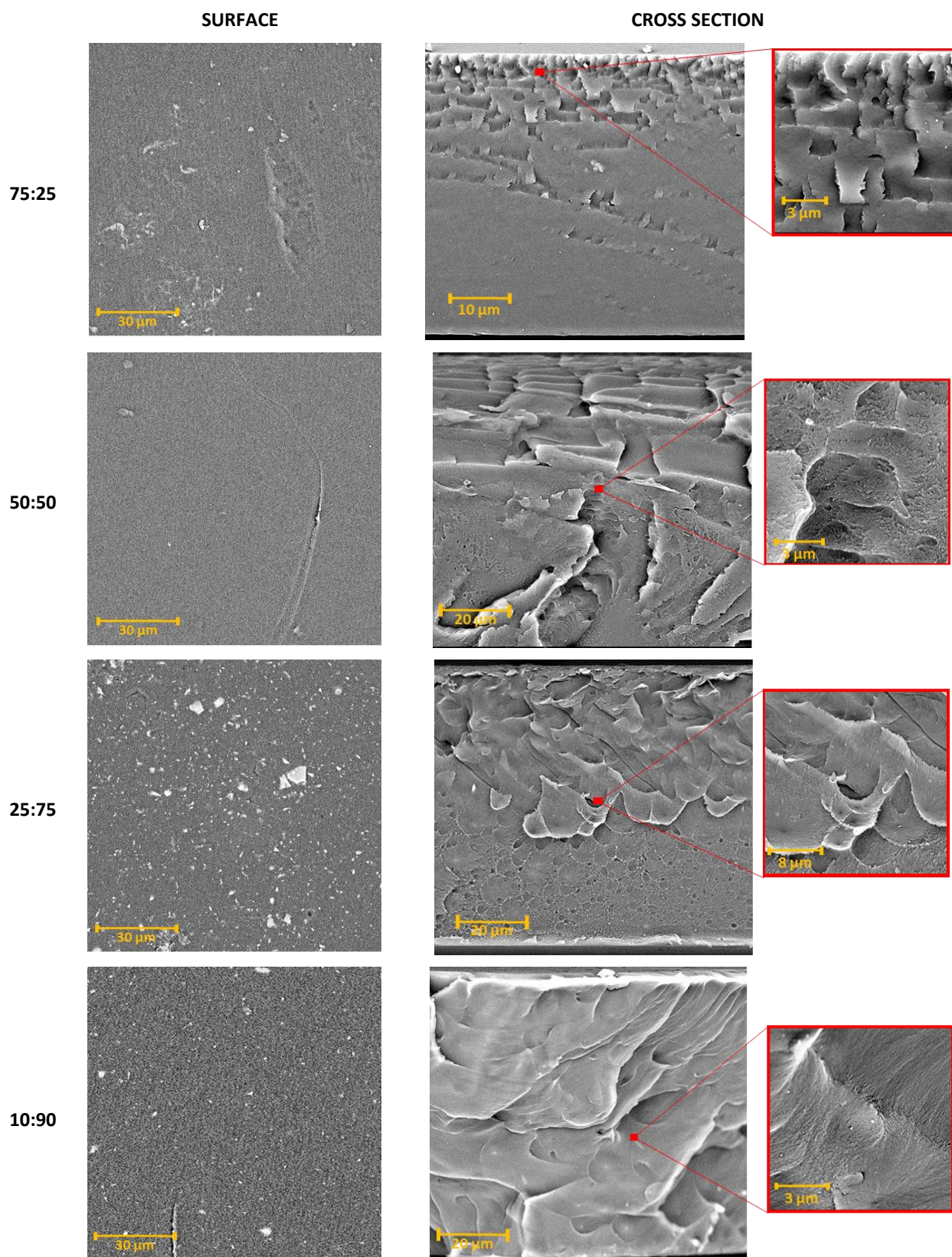
Figure 4.14 SEM images of PIM-DBzMP/PIM-1 (nn:mm) membranes surfaces (right) and cross sections (left) acquired with a backscattered detector and a primary electron beam of 15 KV. The ratio nn:mm represents the molar ratio of the two monomers PIM-DBzMP:PIM-1 in the copolymer.

4.2.5.2   PIM-1/PIM-SBI-Trip copolymers

The mechanical properties of the PIM-SBI-Trip and its copolymer with the archetypal PIM-1, i.e., PIM_1/PIM-SBI-Trip, are tested after methanol treatment and thermal conditioning. Figure 4.15 shows the frequency distribution of the four samples. Two samples were only soaked in methanol (violet and blue distribution), and the other two were further thermally conditioned (pink and red). The copolymer PIM-1/PIM-SBI-Trip have an elastic modulus of 1.79 ±0.08 GPa. This value is intermediate between the one of PIM-1 (1.25±0.04 GPa) and the homopolymer PIM-SBI-Trip 2.00±0.05 GPa, according to its composition.
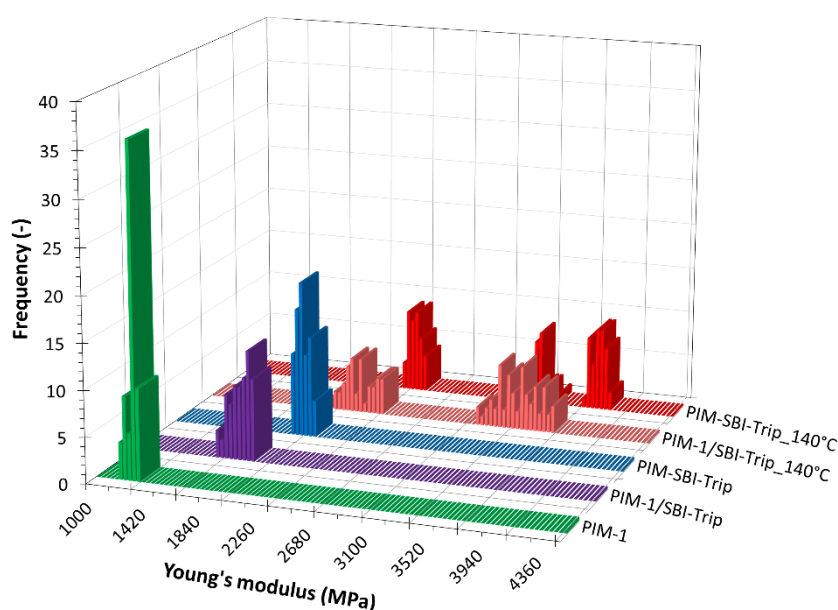
Figure 4.15 Frequency distribution of the Young's moduli of fresh PIM-1, fresh and thermally treated (140°C for 4h) PIM-SBI-Trip and PIM-1/ PIM-SBI-Trip membranes.

The samples tested after the methanol treatment exhibit a single sharp distribution. On the other hand, the thermally treated samples present a multimodal distribution. The reason is not entirely clear, but since the surface shows micro-scale cracks down to about 10 microns from the surface, (Figure 4.16), the heterogeneity in the mechanical properties could be due to non-uniform shrinkage of the samples during heating and subsequent cooling.

MeOH **+140°C_4h**
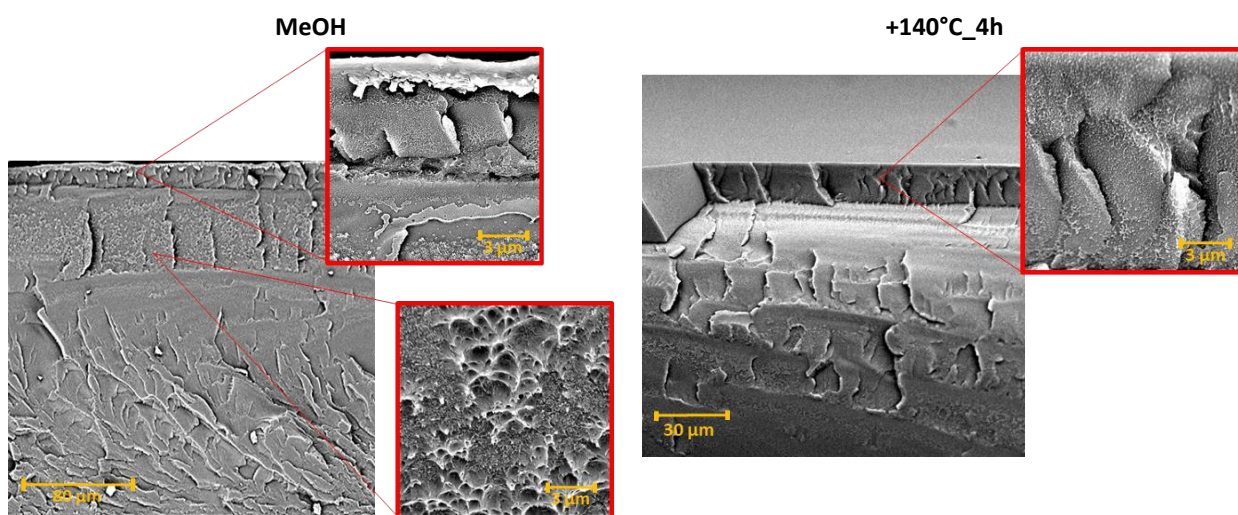
Figure 4.16 SEM image of PIM-1/ PIM-SBI-Trip acquired on fresh MeOH treated sample (left) and the heat-treated sample (right). The images are acquired with a backscattered detector and a primary electron beam of 10 KV.

In SEM images both membranes have a dense morphology with apparent secondary mesoscale porosity, typically observed in PIMs, (Figure 4.17).[79]

PIM-SBI-Trip **PIM-1/ PIM-SBI-Trip**
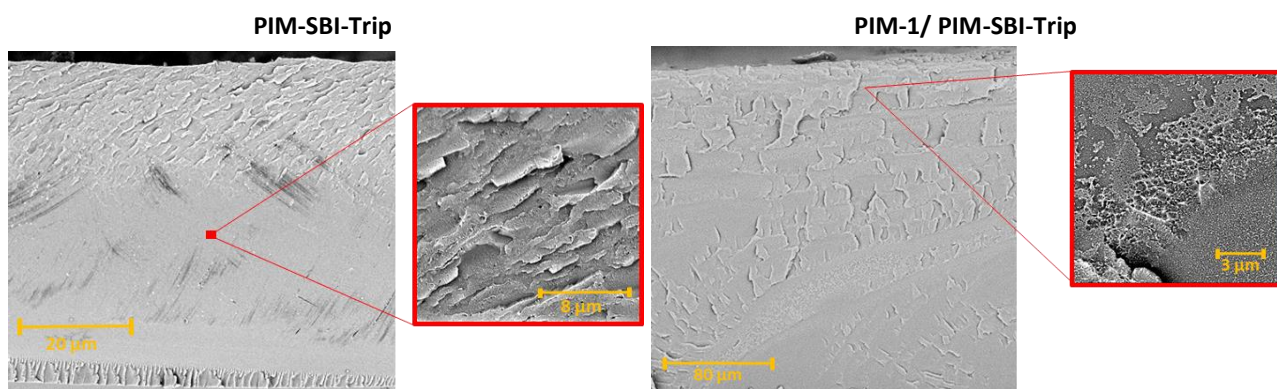
Figure 4.17 SEM images of as cast PIM-SBI-Trip (left) and PIM-1/ PIM-SBI-Trip (right) cross section acquired with a backscattered detector and a primary electron beam of 10 KV.

4.3 Temperature Dependence of Gas Permeation and Diffusion

Since different membrane processes are carried out at different temperatures, or since within the same process the temperature may fluctuate, a detailed knowledge of the temperature-dependence of the membrane performance is important. Therefore, the transport parameters of the two ultrapermeable PIMs (PIM-BTrip and PIM-TMN-Trip) were studied as a function of temperature from 25°C to 55°C. They are chosen as representative samples in the high and low permeability range of the ultrapermeable PIMs. Since freshly prepared PIM membranes are known

to undergo physical aging, [82,89] a PIM-TMN-Trip sample that was already aged for 100 days after thermal treatment (heated at 140 °C for 4 h in vacuum) and a PIM-BTrip sample that was physically aged for 250 days were used during the permeation tests to guarantee time-independent performance. The results are plotted in Figure 4.18.
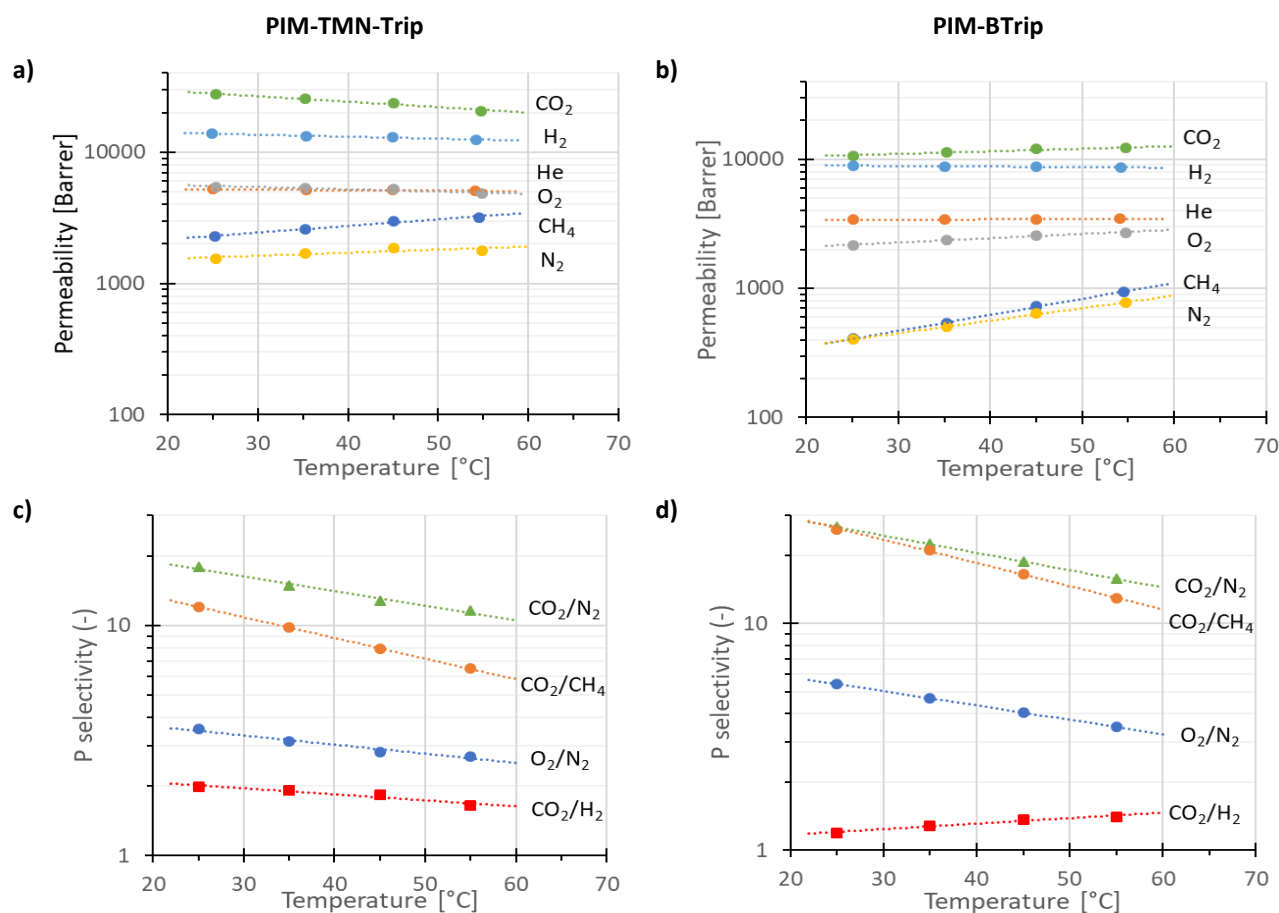
Figure 4.18 (a, b) Permeability coefficient and (c, d) ideal permselectivity of four relevant gas pairs for PIM-TMN-Trip and PIM-BTrip as function of temperature during a heating cycle from 25°C to 55°C with steps of 10°C. Dotted lines are the least squares fit of the experimental data with an exponential equation and are shown as a guide to the eye.

In general, for both membranes the permeability increases with temperature, with exception of the very small penetrants (H_2 and He), which maintain an almost constant value. For the PIM-TMN-Trip membrane, the permeability decreases with temperature for faster penetrants (CO_2 and O_2), Figure 4.18a, b. The order of permeation is $N_2 < CH_4 < O_2 < He < H_2 < CO_2$, over the entire range of temperatures, with exception of He and O_2 which are inverted in PIM-TMN-Trip. With rising temperature, the selectivity for all gas pairs decreases and its effect is strongest for CO_2/CH_4 (Figure 4.18c, d). The only exception is the gas pair CO_2/H_2 in PIM-BTrip (Figure 4.18d), the selectivity trend is determined by the increase of the e CO_2 permeability with temperature, whereas it decreased for

PIM-TMN-Trip. The trends in *P* are better understood when looking at *D* and *S* individually. The diffusion coefficients of all gases increase with temperature (Figure 4.19a, b). As described in the paragraph 2.3, a higher temperature favours the molecular vibrations and facilitates the opening of a motion-enabled zone through which the gases can diffuse, in agreement with the theory of the non-specific activated diffusion process.[90] For the same reason, a lower diffusion coefficient is accompanied by a higher temperature dependence. The diffusion coefficients of H_2 and He are similar in both PIMs, whereas bulkier gases showed a markedly lower diffusion coefficient in PIM-BTrip. The enhanced diffusivity selectivity observed in PIM-BTrip clearly suggests a higher size-sieving behaviour for this polymer with respect to PIM-TMN-Trip.
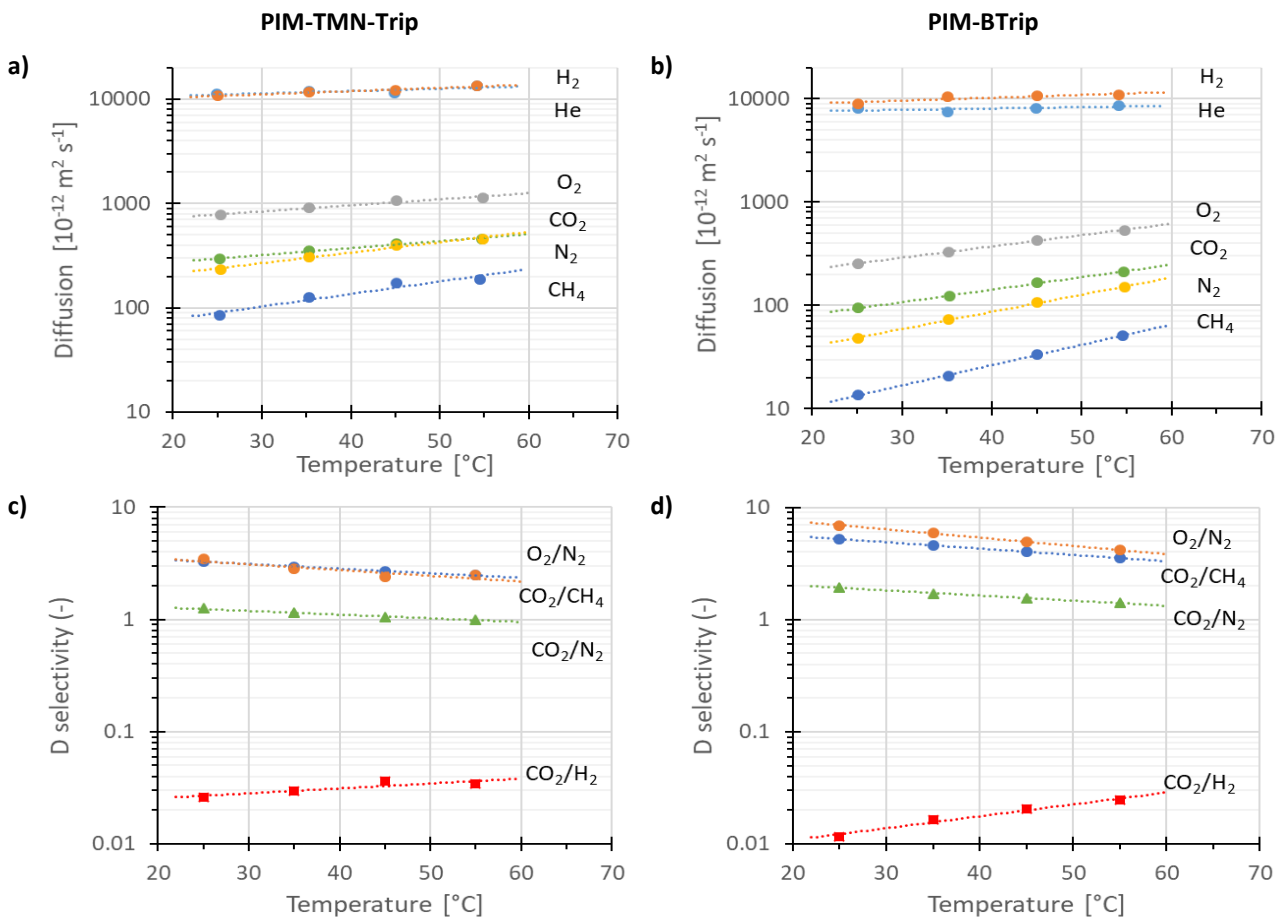
Figure 4.19 Diffusion coefficient (a,b) and diffusion selectivity (c,d) of four relevant gas pairs for PIM-TMN-Trip and PIM-BTrip as function of temperature. Dotted lines are least squares fit of the experimental data with an exponential equation

Both polymers have nearly identical and extremely high gas solubility (Figure 4.20a,b), for example, almost 100 times higher for CO_2 than in Pebax®1657 at 25°C (paragraph 3.3.1). It should be noted that the calculated values for H_2 and He loses precision due to the fast membrane time-

lag, which leads to a likely overestimation. Nevertheless, this deviation is almost negligible on the logarithmic scale used in the figure. The high permeability coefficients of these two polymers are due to a combination of extremely high gas solubility and high diffusivity. In both PIMs the solubility selectivity for gas pairs involving CO_2 decreases with temperature, reflecting the stronger decrease in solubility of CO_2 (Figure 4.20c, d) because the most soluble gases are usually more affected by a temperature change.
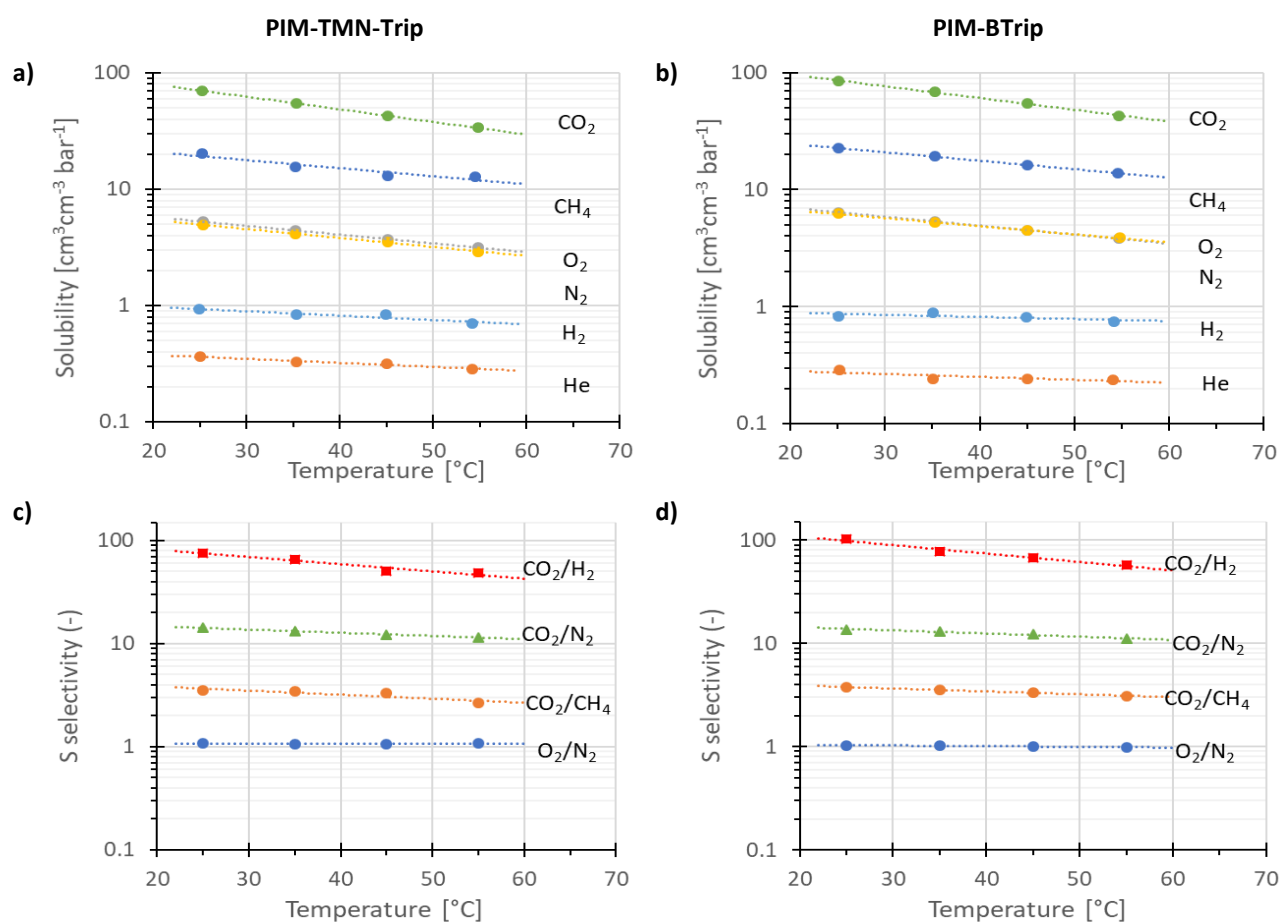
Figure 4.20 (a, b) Solubility coefficient and (c, d) solubility selectivity of four relevant gas pairs for PIM-TMN-Trip and PIM-BTrip as function of temperature. Dotted lines are least squares fit of the experimental data with an exponential equation and are plotted as a guide to the eye.

An overall analysis on transport coefficients reveals that diffusion is most affected by temperature in PIM-BTrip, resulting in an increasing permeability with temperature. In PIM-TMN-Trip, the effect of temperature on the relative contributions of the diffusion coefficients and on the solubility has different weights depending on the penetrant, causing different trends for all penetrants.

4.3.1 Entropic and energetic selectivity analysis

Table 4.4 lists the values of activation energy of permeability (E_p), the heats of sorption (H_s) and the activation energy of diffusion (E_d) of six gases for the polymers PIM-BTrip and PIM-TMN-Trip.

Table 4.4 Activation energies for Permeation (E_p) and diffusion (E_d), and heat of sorption (H_s), for six gases in PIM-1, PIM-TMN-Trip and PIM-BTrip

	Gas	Energy, [kcal mol^{-1}]		
		PIM-1[a]	PIM-TMN-Trip[b]	PIM-BTrip[b]
E_p[c]	N_2	2.8	1.06	4.34
	O_2	0.6	-0.76	1.49
	CO_2	0.4	-1.84	0.90
	CH_4	4.2	2.27	5.55
	H_2	0.4	-0.67	-0.21
	He	0.6	-0.15	0.12
H_s[d]	N_2	-3.1	-3.44	-3.11
	O_2	-4.7	-3.38	-3.41
	CO_2	-3.8	-4.85	-4.50
	CH_4	-3.7	-3.12	-3.24
	H_2	-2.8	-1.67	-0.77
	He	-2.4	-1.53	-1.14
E_d[e]	N_2	6	4.50	7.45
	O_2	5.3	2.62	4.90
	CO_2	4.2	3.01	5.40
	CH_4	7.8	5.39	8.78
	H_2	3.2	1.00	0.57
	He	3	1.38	1.26

a) data from reference [91]; b) this work; c) Calculated from Eq. 2.12; d) Calculated from Eq. 2.13; e) Calculated from Eq. 2.14

The value of E_p in PIM-BTrip is positive for all the gases, with exception of H_2, while for PIM-TMN-Trip, E_p is positive only for the bulkiest gases (N_2 < CH_4) and negative for the other four (He > H_2 > O_2 > CO_2). A negative E_p means that the permeability decreases with temperature. All heats of sorption (H_s) are negative values, similar to PIM-1 for N_2, O_2 and CH_4 and more negative for CO_2.[91]

The activation energy of diffusion (E_d) for H_2 and He in PIM-TMN-Trip and PIM-BTrip are among the smallest values known, and smaller compared to those in PIM-1. These small values indicate a low energy barrier for diffusion, which is weakly influenced by the temperature and ascribed to the

intrinsic microporosity. [91,92] On the other hand, the E_d for O_2, CO_2, N_2 and CH_4 of the two PIMs are similar to those found for PIM-1 (Figure 4.21). The slope of the activation energy of diffusion as a function of the square effective diameter follows the trend PIM-1 < PIM-TMN-Trip < PIM-BTrip (Figure 4.21). The steeper the slope, the higher the size-sieving behaviour of the polymer. All heats of sorption (H_s) are negative values, similar to those of PIM-1 for N_2, O_2 and CH_4 and more negative for CO_2.[91] The value of H_s represents the strength of the polymer-sorbent interaction, which decreases when thermal motion increases.
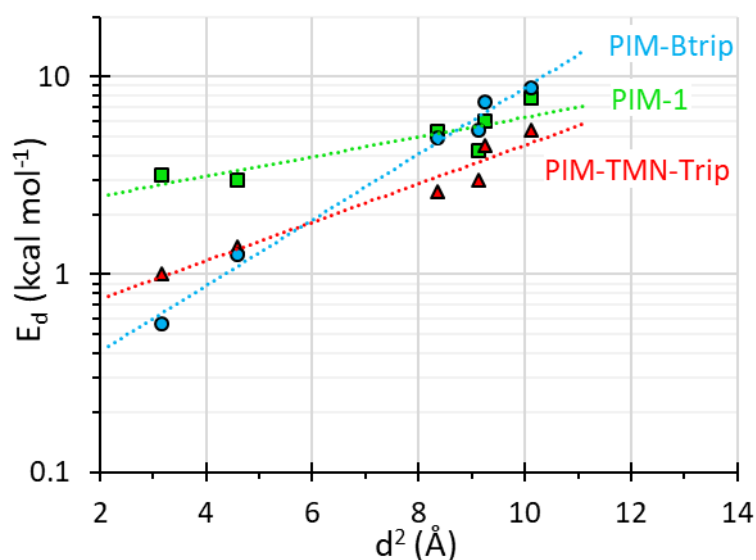
Figure 4.21 Activation energy of diffusion for PIM-1 (■)[91], PIM-TMN-Trip (▲) and PIM-BTrip (●) as a function of the gases effective diameter.[48] (Lines are plotted as a guide for the eyes)

Table 4.5 shows the diffusion selectivity and correlated energetic and entropic selectivity for six gases for PIM-1, PIM-TMN-Trip and PIM-BTrip. The energetic selectivity values are all greater than one, except for CH_4. This is due to the bigger effective diameter of CH_4 compared with N_2, requiring a more extended motion-enabled zone for diffusion. An energetic selectivity of about 1 indicates that the free volume elements are interconnected by windows that are larger than the kinetic diameter of these gases. He and H_2 have very high energetic selectivity in PIMs since the diffusion of these two small gases requires a smaller motion-enabled zone between molecular chains than the bulkier N_2, which needs more energy to open a gap between the very rigid polymer chains. The lower polymer cohesion of PIM-TMN-Trip is also consistent with its greater solubility in organic solvents and the lower energetic selectivity for diffusion.

Table 4.5 Diffusion selectivity (D_i/D_{N_2}) and correlated energetic and entropic selectivity for six gases at 25°C in the four polymers PIM-1, PIM-TMN-Trip and PIM-BTrip.

	Gas	PIM-1[a]	PIM-TMN-Trip	PIM-BTrip
Diffusion	O_2	2.93	3.31	5.25
selectivity	CO_2	1.60	1.25	1.94
(i/N_2)	CH_4	0.33	0.36	0.28
	H_2	45.3	47.6[c]	166[c]
	He	44.0	45.7[c]	184[c]
Energetic [b]	O_2	3.26	24.1	74.1
selectivity	CO_2	20.9	12.5	31.9
(i/N_2)	CH_4	0.048	0.23	0.10
	H_2	113	371[c]	1.12E+05[c]
	He	159	194[c]	3.45 E+04[c]
Entropic [b]	O_2	0.99	0.15	0.08
selectivity	CO_2	0.077	0.10	0.06
(i/N_2)	CH_4	6.37	1.48	2.44
	H_2	0.81	0.26[c]	0.003[c]
	He	0.81	0.69[c]	0.016[c]

a) diffusion selectivity data from reference [91]; b) the energetic and entropic selectivities are calculated in this work; c) It should be noted that the calculated values for H_2 and He lose precision due to the fast membrane time-lag, which lead to a likely underestimation of the diffusion coefficient of max. 25%.

The entropic selectivity for a gas over N_2 in PIMs is low for all gases, with the exception of the gas pair CH_4/N_2, for which it is greater than 1 in the investigated PIMs, Table 4.5. PIM-1 demonstrates O_2/N_2 entropic selectivity that is typical of that of semi-rigid polymers with rigid fused-ring components linked together by flexible units (i.e. ether bonds, methylene groups or spiro-centres). The inverse O_2/N_2 entropic selectivity of PIM-TMN-Trip and PIM-BTrip can be ascribed to the greater rotational mobility of O_2 in the micropores compared to N_2. When the molecules have to diffuse through the windows between the micropores, the high rigidity of the triptycene-based polymers PIM-TMN-Trip and PIM-BTrip makes these windows similar to carbon molecular sieve pores, where O_2 and N_2 have similar entropy. Thus, the transition from a region where O_2 has a greater entropy than N_2, to a region where their entropy is similar, gives rise to reverse entropic selectivity. In the case of He/N_2 and H_2/N_2, this effect is even stronger, as highlighted by the very low entropic selectivity in the 250 days aged PIM-BTrip. These two light gases have more entropy in the free

volume elements compared to bulkier gases. When they have to diffuse through a motion-enabled zone, their entropy is drastically reduced, and this reduction is relatively large with respect to that experienced by bulky gases. This relative reduction leads to a large inverse entropic selectivity that is, nevertheless, swamped by a strong energetic selectivity.

4.4 Conclusion

Permeation tests and AFM force spectroscopy studies on a series of different PIM membranes revealed a strong correlation between the transport parameters and the polymer film stiffness. Structurally similar samples with different history follow a nearly universal trend, independent of the specific sample. Excellent agreement between Young's modulus obtained for reference sample PIM-1, and values reported in the literature based on different analytical techniques, show that AFM force spectroscopy offers a practical and convenient alternative to measure the mechanical properties of PIMs. This technique is particularly useful for 'exotic' polymers for which only small samples are available. For the series of structurally similar ultrapermeable PIMs, it was found that the decrease of the diffusion coefficients during aging is associated with an increase in their Young's modulus. Extensive transport studies on the sample PIM-DTFM-BTrip after different conditioning steps, highlight that the decrease of permeability in time is mainly due to the reduction of the diffusion coefficient. Thermal treatment accelerates the physical aging of the samples in terms of transport parameters and slightly slows down further aging. Also in terms of mechanical properties, after an initial increase in Young's modulus, there is a slower further increase with time, apparently because the high temperature stabilizes the sample properties. Interestingly, it appears that the permeation measurement itself affects the physical aging of these polymers: membranes immediately tested after methanol treatment or thermal treatment at 140 °C exhibit significantly faster aging compared to the membranes tested only after additional 30 days of aging at ambient conditions. It will be subject of further studies to investigate whether this is due to more efficient removal of residual solvent under vacuum, or whether the vacuum exposition during the permeation tests results in higher aging rates. Studies on PIM-2 reveal a high rigidity of the polymer already after only methanol treatment and after thermal treatment, which further increases upon aging. This high elastic modulus is a result of the rigid ladder-like polymer backbone in combination with the halogen bonds occurring within the polymer matrix. Analysing the mechanical properties

of PIM-DBzMP and PIM-SBI-Trip and their copolymers with PIM-1, it is shown also that the Young's modulus can be tailored by the copolymer composition. Overall, it can be concluded that the gas permeability and diffusivity systematically decrease with Young's modulus in PIMs, in a somehow universal trend, regardless the sample history. Some sample-to-sample differences indicate that the correlation is not perfect, and that other independent factors may play a role, such as differences in pore size distribution and fractional free volume.

The permeation analysis on PIM-TMN-Trip and PIM-BT revealed that the enhanced gas-separation performances for O_2/N_2, H_2/N_2, and He/N_2 relative to those of PIM-1 are driven by strong energetic selectivity, with extremely high values demonstrated for PIM-BTrip. Hence, when the penetrant gas diffuses though a well-packed region of the polymer, the opening of motion-enabled zones in PIM-TMN-Trip and PIM-BTrip requires a displacement of the very rigid polymer chains, which leads to high energetic selectivity as a function of the penetrant dimensions. The comparison with PIM-1 highlights that the very rigid molecular structures of PIM-TMN-Trip and especially of PIM-BTrip, which does not possess the flexible TMN solubilizing group, enhance the energetic selectivity and thus the diffusion selectivity. In addition, the operating membranes derived from triptycene-based PIMs at low temperatures may help to achieve commercially interesting separation factors for several gas pairs. This is especially valid for the gas pairs CO_2/N_2 and CO_2/CH_4 where the enhanced selectivity is accompanied by the enhanced permeability of CO_2 due to its strong increase in solubility.

Chapter 5

Membranes of polymer blends.[1]

---

[1] Parts of this chapter are published as: **M. Longo**, B. Comesana-Gandara, M. Monteleone, E. Esposito, A. Fuoco, L. Giorno, N.B. McKeown, J.C. Jansen, **Matrimid®5218/AO-PIM-1 Blend Membranes for Gas Separation**, J. Membr. Sci. Res., *in press*. https://doi.org/10.22079/JMSR.2021.540493.1504. [135]

5.1 Introduction

An alternative method to tailor the properties of gas separation membranes is by blending two different polymers. This procedure is somewhat more flexible than copolymerization of different monomers that yields copolymers of different compositions (see previous chapter) but requires good compatibility of the two polymers and it requires that both are soluble in the same solvent.

5.1.1 Properties of polymer blend membranes

Generally, commercial glassy polymers used for gas separation membranes, such as polysulfones, polyethersulfones and polyimides have a good selectivity, but low permeability. Blending of polymers is one of the possible strategies to combine the advantages of each polymer into a blend product. Most performing polymers with a combination of high permeability and good selectivity, such as thermally rearranged (TR) polymers [93,94] and polymers of intrinsic microporosity (PIMs) [37,95] are expensive and the synthesis is difficult to realise at industrial scale, or have other issues such as physical aging [23]. A possible way to boost the use of expensive high-performance polymers in large-scale applications is by blending them with a second inexpensive polymer. Potentially, this strategy combines the advantages of each polymer into a blended product and obtains the desired properties that differ from those of the individual polymers.[96]

The ability to predict polymer blend membranes permeability from single polymeric permeabilities is highly desired in order to identify optimum membrane candidates. A simple equation for predicting the permeability of a homogeneous miscible blend is proposed by Robeson,[97] expressing the permeability, P_b, in terms of the volume fractions and permeabilities of the individual components:

$$ln\, P_b \;=\; \varphi_1\, ln\, P_1 \;+\; \varphi_2\, ln\, P_2 \qquad\qquad \text{Eq. 5.1}$$

where φ_1 and φ_2 are the volume fractions of the two polymers in the blend, and P_1 and P_2 are their respective permeabilities. This empirical equation shows the behaviour of permeability as a function of membrane composition.[97]

One of the possible problems of polymer blends is the limited miscibility and homogeneity of the blend components. Miscible blends are a homogeneous system where two materials dissolve in

each other at the molecular level, exhibiting single phase properties. Instead, in immiscible blends, the two components do not or do not completely dissolve in each other, thus resulting in the formation of two different phases. For systems where the dispersed phase is less than ca. 30 vol% and consists of spherical particles, the Maxwell model is usually employed to describe the gas transport [98–101]:

$$P_{MMM} = P_c \left[\frac{P_d + 2P_c - 2\varphi_d(P_c - P_d)}{P_d + 2P_c + \varphi_d(P_c - P_d)} \right]$$

Eq. 5.2

where the P_{MMM} is the effective permeability of the mixed matrix membrane, P_c and P_d are the gas permeabilities in the continuous and dispersed phase, respectively and φ_d is the volume fraction of dispersed phase. The gas transport in a mixed matrix membrane depends on the two different phases and on the nature of their interface, and several fundamentally different cases were discussed by Koros et. al. [102]. Systems with a higher concentration of the dispersed phase and with non-spherical particles require different and more complex models.

The fundamental understanding of the phase behaviour and the molecular interaction of the blend components is essential to develop desirable membrane materials for gas separation. A miscible blend is needed for producing a membrane with a uniform and stable properties. The selection of the proper parent polymers with the desired physical and chemical properties is one of the key strategies in the development of polymer blends. There are various methods available to determine the phases of polymer blends. One of the simplest ways to visualize the morphology or microstructure of the polymer blends is through SEM inspection with elementary analysis (EDX) or with a compositions-sensitive detector (e.g. backscattering detector).

5.1.2 Matrimid®5218/PIM Blend Membranes

Matrimid®5218 has good selectivity and relatively low permeability. However, its permeability is too low for applications that need to handle extremely large gas volumes, such as CO_2 capture. A possible route to overcome this limitation is the blending with a Polymer of Intrinsic Microporosity (PIM) to exploit the high selectivity of Matrimid® and the exceptionally high permeability of the PIM.[16] Various blends of PIMs and other polymers have been reported in the literature.[103] Blends of Matrimid®5218 with PIM-1 were first reported by Yong *et al.,*[104] showing that the

addition of a small quantity of Matrimid®5218 in PIM-1 improved the O_2/N_2 permselectivity, while a small amount of PIM-1 in an excess of Matrimid®5218 enhanced the CO_2/CH_4 gas separation performance. Moreover, they used the PIM-1/Matrimid®5218 blend to fabricate hollow fibres, demonstrating the greater versatility of the polymer blend for obtaining an ultrathin dense layer, potentially suitable for industrial use,[105] and using much less PIM-1 than the pure PIM-1 fibres.[106] More recently, the comparison between the highly selective Matrimid®5218, the highly permeable PIM-EA(H_2)-TB and their 50/50 wt% blend membrane showed an increase of permeability of Matrimid®5218 by the addition of the ethanoanthracene-based PIM, whilst maintaining a reasonably high selectivity.[103]

5.2 Matrimid®5218/AO-PIM-1 Blend Membranes

In the present paragraph blends of Amidoxime-functionalized PIM-1 (AO-PIM-1) and the commercial polyimide Matrimid®5218 are discussed. PIM-1 was synthesized and the subsequent amidoxime-modification was made to realise blended polymer membranes with AO-PIM-1 and Matrimid®5218 for gas separation. The aim of this work is to enhance the permeability of Matrimid®5218 by the addition of AO-PIM-1, and to find the optimum combination of the high permeability of the PIM and the high selectivity of the polyimide. In this chapter, a detailed analysis of the gas transport parameters under single permeation conditions of the novel Matrimid®5218/AO-PIM-1 blend is reported (Figure 5.1).

a)   b)
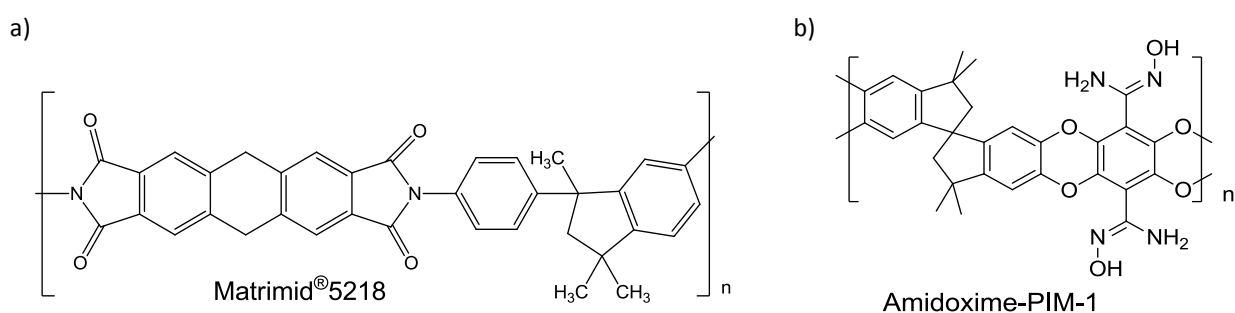
Figure 5.1 Chemical structures of Matrimid®5218 (a) and AO-PIM-1 (b).

The use of the AO-PIM-1 in this work is inspired by a previous study in which Swaidan *et al.* show how the AO-modification induced a tightening of the polymeric matrix and an improvement of

selectivity over PIM-1.[107] It is also evaluated the effect of a PDMS coating on the reduction of possible pinhole defects present in the membrane. The aim of this work is to enhance the permeability of Matrimid® by the addition of AO-PIM-1, and to find the desired combination of the high permeability of the PIM and the high selectivity of the polyimide. Detailed analysis of the gas transport parameters under single gas permeation conditions will provide deep insight into the role of gas diffusivity and solubility in the overall transport properties of the novel blend.

5.2.1 PIM-1 synthesis and AO-Modification

The commercially available catechol 5,5',6,6'-tetrahydroxy-3,3,3',3'-tetramethyl-1,1'-spiro-bisindane (TTSBI) was purified by soxhlet extractor and a thimble filter with two different solvents: chloroform and isopropanol. Soxhlet extraction was used because contrary to the pure compound, the impurities are soluble in chloroform and they were discarded after 24 h under reflux. The compound remained in thimble filter is further purified with the isopropanol. The high solubility of the TTSBI in this solvent allowed after some soxhlet cycles and a simple filtration to separate the latest impurities and recover the pure compound. It was dried for 24 hours in oven at 100°C and other 24 hours in oven at 100°C under vacuum. An NMR spectrum in acetone was recorded in order to evaluate the purity of the compound (96.88 wt% compound - 1.95 wt% acetone - 1.17 wt% isopropanol), Figure 5.2.
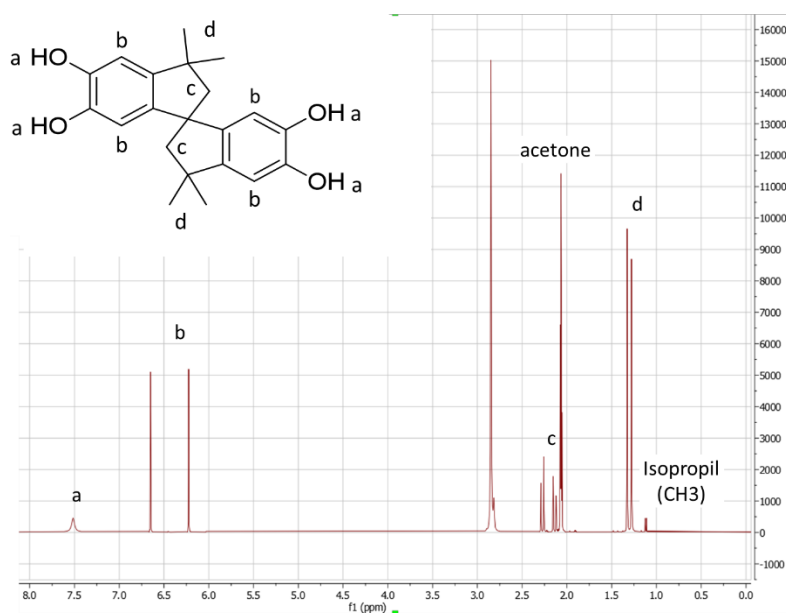
Figure 5.2 NMR spectra of 5,5',6,6'-tetrahydroxy-3,3,3',3'-tetramethyl-1,1'-spirobisindane

PIM-1 was synthesized according to procedure reported by Budd et al [66]. A mixture of 5,5',6,6'-tetrahydroxy-3,3,3',3'-tetramethyl-1,1'-spirobisindane (TTFPN) (5 g, 13.2 mmol), 2,3,5,6-tetra-fluoroterephthalonitrile (2.6 g, 13.2 mmol) and anhydrous DMF (90 mL) was stirred under a dry nitrogen atmosphere. Anhydrous K_2CO_3 was added in stoichiometric excess (14.52 g, 105.6mmol) and the mixture heated at 65 °C for 3 days. Figure 5.3 shows the reaction scheme of the polymer:
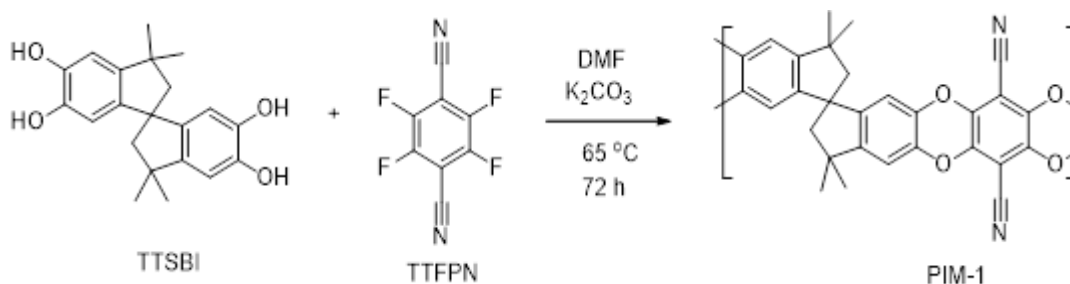
Figure 5.3 Reaction scheme of PIM-1

After cooling down to room temperature, the reaction mixture was precipitated in water and the precipitate was collected by filtration. Repeated washing from water, acetone and methanol, gave 3.5 gr of fluorescent yellow polymer. The synthetized polymer proved soluble in chloroform allowing its analysis by gel-permeation chromatography, which confirmed that a high molecular mass polymer was achieved (average molar mas of 220 Kg mol^{-1} relative to polystyrene standards). Finally, the product was dried in an oven at 100 °C overnight.

AO-PIM-1 was synthesised according to the method reported by Patel *et al.* [108]. 3.5 gr of PIM-1 was dissolved in 60 mL tetrahydrofuran (THF) at 65 °C under a dry nitrogen atmosphere. Then, 150 mL of hydroxyl amine was added drop-by-drop with a syringe. The reaction mixture was refluxed at 70 °C for 48 hours. Figure 5.4 shows the reaction scheme of the Amidoxime-PIM-1. After cooling, the polymer was precipitated by pouring the solution in ethanol and the white product was collected by filtration. The polymer was filtered and washed with ethanol for four times and dried in an oven at 100 °C for 24 hours.

Thermogravimetric analysis (TGA) was performed on pure AO-PIM-1 and Matrimid® polymers in order to check for the presence of water or residual solvent in the polymer and to evaluate their thermal stability.
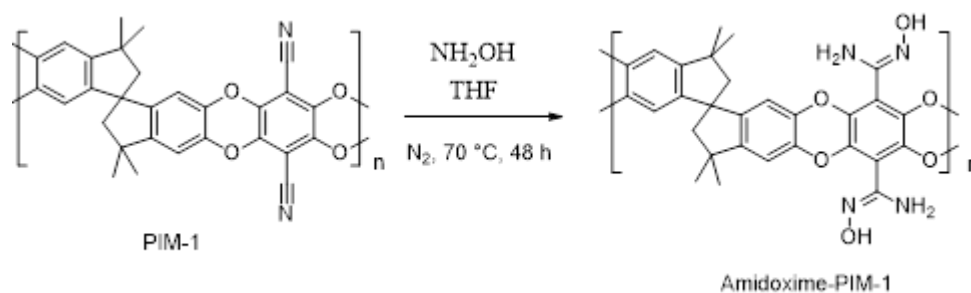
Figure 5.4 Reaction scheme of Amidoxime-PIM-1 (AO-PIM-1)

5.2.2 Preparation of Matrimid®5218/AO-PIM-1 Blend Membranes

AO-PIM-1/Matrimid® dense films were prepared by a solution casting method in anhydrous dimethylacetamide (DMAc). The pure Matrimid® solution at a concentration of 3 wt% was prepared and homogenous solution was obtained under magnetic stirring overnight. Matrimid®5218/AO-PIM-1 blend solutions were obtained by mixing a fixed amount of Matrimid®5218 solution (containing 0.140 g of Matrimid®) with different amounts of AO-PIM-1 solution (to yield mixtures with 20 wt%, 40 wt%, 60 wt% and 80 wt% of AO-PIM-1 in Matrimid®5218 after solvent evaporation). The pure PIM solutions were prepared at concentrations between 2-3%. The resulting solutions were stirred until they became homogeneous and filtered (3.1 µm GMF syringe filters) to remove possible dust or polymer gel particles. Membranes were casted pouring the solutions in a glass Petri dish of 12 cm diameter, placed in the oven at 50 °C for at least 5 days. The dense films were labelled as Matrimid®_AO-PIM-1 xx_yy, where xx_yy represent the weight percentages of the two polymers, as reported in Table 5.1.

Table 5.1 Membrane codes and percentage of AO-PIM-1 in the final membrane

Name Matrimid®5218_AO-PIM-1	Matrimid®5218 (mg)	AO-PIM-1 (mg)	AO-PIM-1 content (wt%)	Membrane thickness (µm) [a]
100_0	140	0	0	19.1 ± 3.5
80_20	140	35	20	11.2 ± 3.4
60_40	140	93	40	30.2 ± 6.5
40_60	140	210	60	54.8 ± 7.5
20_80	140	560	80	74.8 ± 12.3
0_100	0	455	100	39.0 ± 4.9

[a] Average thickness and standard deviation from at least 8 individual measurements on the same membrane without silicon coating.

This procedure yields membranes in which the thickness increases with the AO-PIM-1 content, but since the permeability and diffusivity are expected to increase with increasing PIM content, the measurement time should not increase dramatically for the thick films.

5.2.3 Chemical and morphological analysis

All membranes showed high optical transparency, suggesting the formation of a homogeneous phase and good compatibility of the two polymers. Chemical and morphological analysis of the membranes were performed by scanning electron microscopy (SEM) and Fourier-transform infrared spectroscopy (FTIR). The SEM images of all samples are collected with a backscattered electron detector (BSD) at different acceleration voltages, in order to probe the sample properties at different depths within the sample. The samples were sputter-coated with a thin layer of gold to minimise the charge and improve the image quality.

While the SEM images of the top surface of the neat polymer membranes appear dense and uniform (Figure 5.5), micro phase separation and domains of different size and shapes are visible in the blend surface. The cross section of the membrane with 20 wt% of AO-PIM-1 shows a layered structure, in which AO-PIM-1 domains of different shape are clearly distinct from the Matrimid® 5218 bulk. Qualitatively, the volume fraction of the dispersed phase in this sample seems to be higher than 20 % of the total volume. This suggests a partial solubility of Matrimid® 5218 in the phase-separated AO-PIM-1. Phase separation is clearly observed in the cross sections of all other blends as well, and the domains of the two polymers have different shapes and dimensions. Thus, the two polymers are poorly compatible and the optical transparency must be a result of the apparently very similar refractive indices of the two polymers. The relatively large domains of the phase separated polymers are a result of the slow evaporation of the solvent and the long time available for the nucleation and growth of the domains of the phase separated polymers.
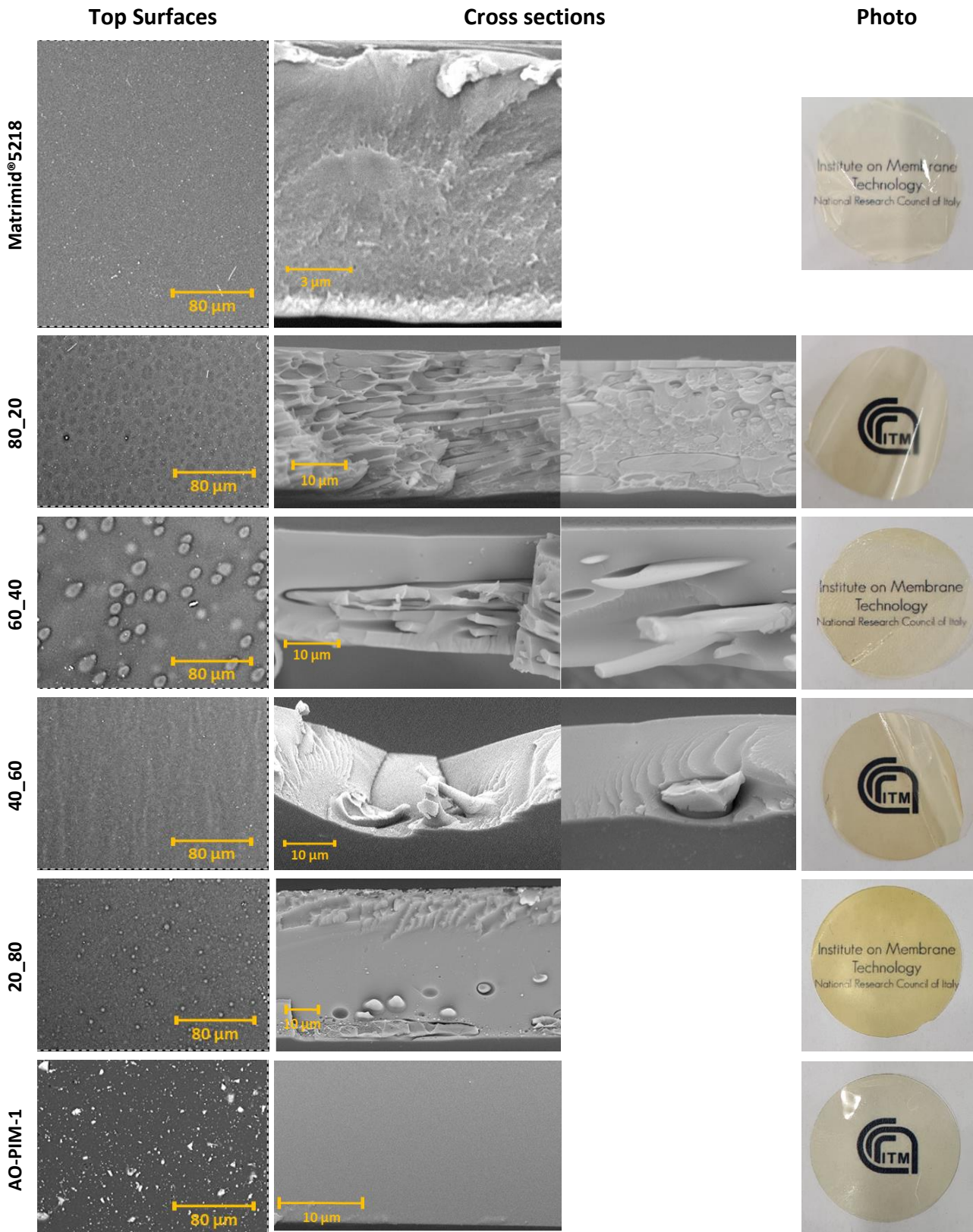
Figure 5.5 SEM images of the surface and cross sections of the pure Matrimid®5218 and AO-PIM-1 membranes, and their blends with compositions of 20, 40, 60 and 80 wt% of AO-PIM-1. Photographs of 2.5 cm circular membranes demonstrate their optical transparency.

Figure 5.6 shows the SEM analysis of the 40_60 membrane at different beam voltages and different measurement modes. The membrane surface image acquired with a backscattered detector and a primary electron beam of 5 KV appears as a homogenous sample (Figure 5.6a). In the same area, using a primary electron beam of 15 KV, some spherical structures appear (Figure 5.6c). Since in this case the beam has much higher energy than in the first case, the secondary electrons emerge from deeper locations within the specimen, so that the layers below the surface are observed. The topographic image in Figure 5.6b, acquired at 5 KV, shows a sample topography in which these structures emerge from the surface.

| (a) 5 kV | (b) Topography (5 kV) | (c) 15 kV |
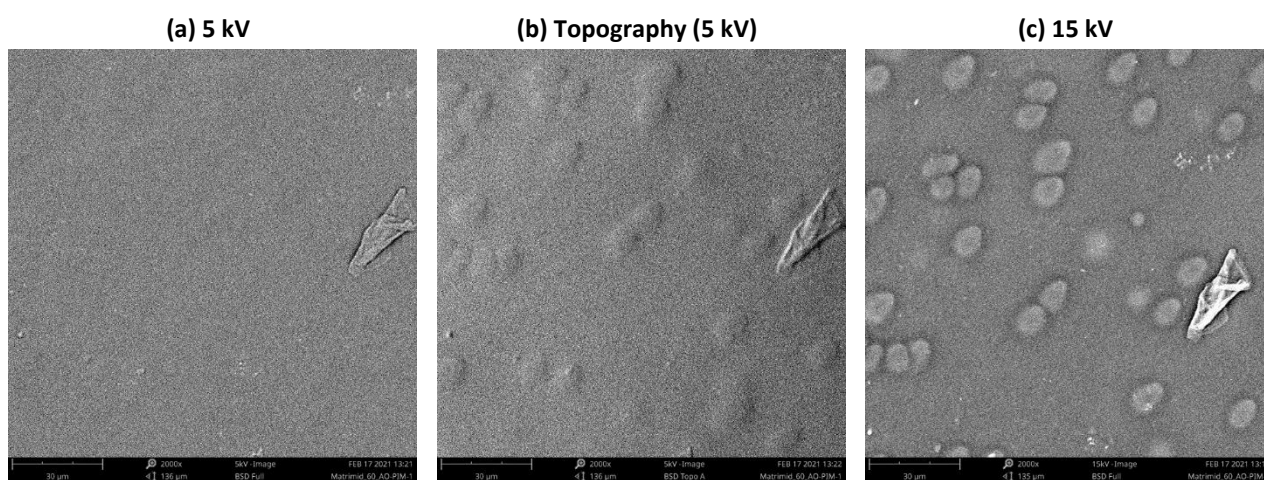
Figure 5.6 Example of SEM images of the blend Matrimid®5218/AO-PIM-1 40_60, acquired with a BSD. The left image (a) is obtained with a low-intensity primary electron beam of 5 kV, the right one (c) with a primary electron beam of 15 kV. The middle image (b) is a topographical image of the sample surface.

The possible presence of chemical interactions between Matrimid®5218 and AO-PIM-1 was studied by a FTIR-ATR. This technique allows the analysis of solids without any sample preparation. The penetration thickness of the incident radiation in ATR mode typically ranges from 0.5 and 2 μm and this allows the analysis of features at or slightly below the surface. The IR-spectrum for neat Matrimid®5218, neat AO-PIM-1 and for the blends are shown in Figure 5.7. The spectrum of Matrimid® 5218 exhibits the characteristic bands of polyimides, denoted by asymmetric and symmetric C=O stretching vibration bands around 1780 and 1720 cm^{-1}; asymmetric C-N stretching at 1365 cm^{-1}; stretching of C-N-C groups at 1102 cm^{-1}; and the out-of-plane bending of C-N-C groups around 725 cm^{-1}.
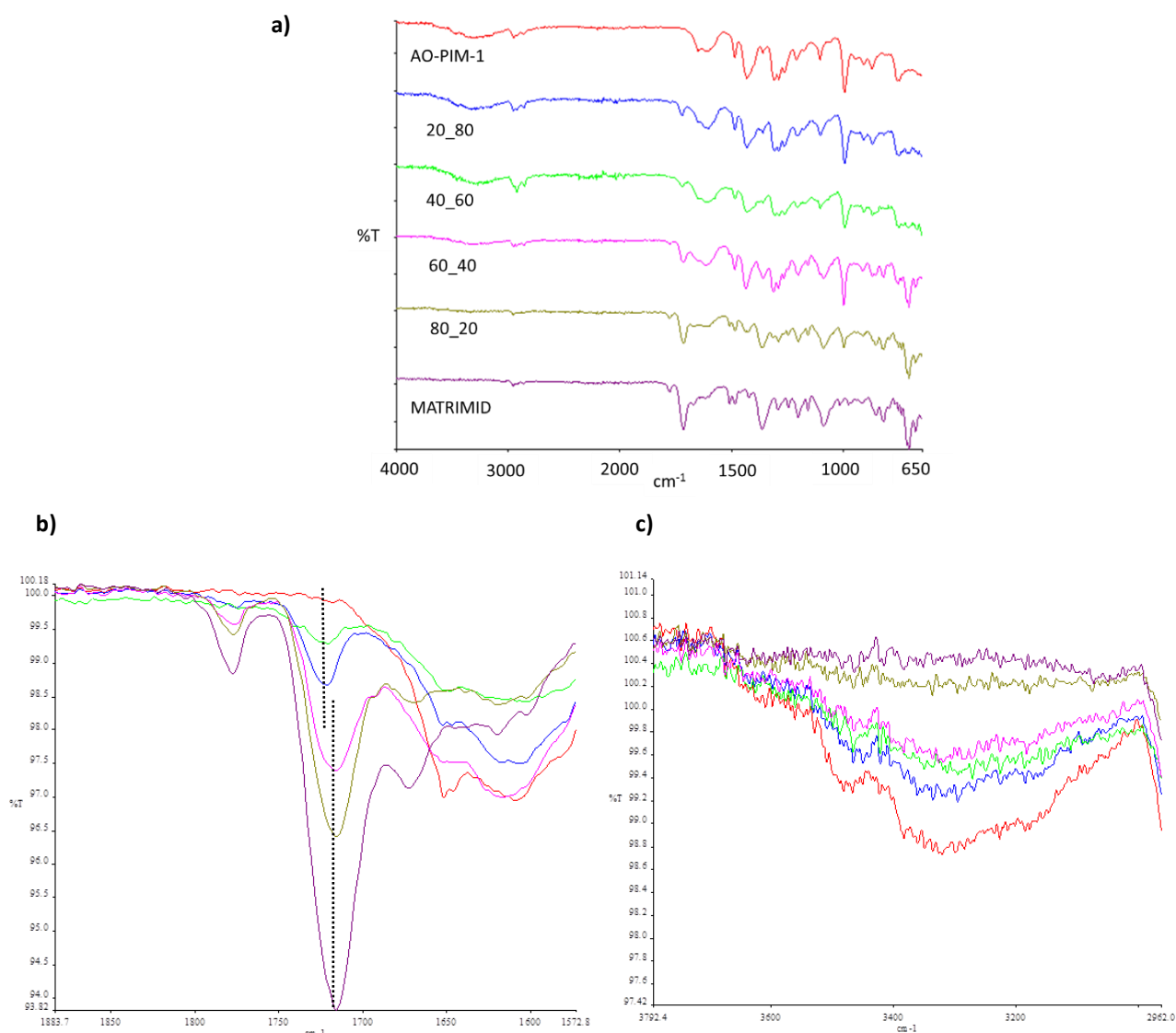
Figure 5.7 a) ATR-FTIR spectra of the Matrimid®5218/AO-PIM-1 blends and neat polymer membranes and a zoom of b) the carbonyl stretching vibration of the Matrimid®5218 around and c) the symmetric and asymmetric -NH$_2$ and -OH stretching vibrations.

The characteristic band of AO-PIM-1 at 3302 cm^{-1} could be assigned to an asymmetric and a symmetric stretching of NH$_2$ groups. A band at 2951 cm^{-1} is assigned to the C–H stretching vibration. The bands at 1608 and 1092 cm^{-1} are assigned to a C=N stretching mode and a C-N-C stretching mode respectively. FTIR spectroscopy is an effective tool for studying the molecular interactions occurring in Matrimid®5218/AO-PIM-1 blends. The C=O peak is absent in AO-PIM-1 and its intensity gradually increases with increasing Matrimid® 5218 content, with some deviations from the trend that may be due to the heterogeneous nature of the blend (Figure 5.7b) and the limited sampling depth in ATR mode. Interestingly, the C=O peak shifts to slightly higher wave numbers at the highest AO-PIM-1 content, where Matrimid® is the dispersed phase. This suggests that interaction between

the two polymers occurs, probably by hydrogen bonding between the C=O group of Matrimid® and the -OH and -NH$_2$ groups of AO-PIM-1, and it supports the hypothesis that Matrimid® is partially soluble in AO-PIM-1. The sharp band at 914 cm^{-1}, ascribed to the N-O stretching vibration mode, representative of the oxime groups, appear in pure AO-PIM-1 and all the blends, but not in pure Matrimid®. The signal at 914 cm^{-1} tends to become more intense with increasing AO-PIM-1 content, and also in this case some deviations from the trend (*e.g.* remarkably strong signal at 40 wt% AO-PIM-1) may be due to the sample heterogeneity. An increasingly intense broad band emerges in the region of 3600 – 3100 cm^{-1}, (Figure 5.7c), involving overlapping bands that are assigned to the asymmetric and symmetric stretching mode of -NH$_2$ groups (3480 and 3340 cm^{-1}, respectively) and the stretching vibration mode of the -OH groups (3175 cm^{-1}), both characteristic of AO-PIM-1.

5.2.4 Coating of the membranes with PDMS

A solution of PDMS ELASTOSIL® M 4601 A/B at 20 wt% was prepared in cyclohexane. PDMS ELASTOSIL® M 4601 A/B is a two-component silicone resin, *i.e.* the base or prepolymer and the curing agent, to be mixed at a ratio of 9:1. The final solution composed of 80 wt% cyclohexane, 18 wt% of base and 2 wt% of curing agent, was stirred for about 1 hour at 60°C to promote a partial initial cross-linking.[109] After cooling, this solution was further diluted with cyclohexane, to obtain a final concentration of 10 wt% silicone resin. The coating was applied with a pipette, while slightly tilting the membranes, allowing the excess solution to flow away. The membranes were left to dry for several days at room temperature, in order to allow the total evaporation of the solvent and the crosslinking of the polymer. The final thickness of the coating layer was approximately 5 μm.

5.2.5 Transport properties of the membranes

Single gas permeation measurements of the pure polymers Matrimid®5218 and AO-PIM-1 and the blend membranes were carried out in the order He, H$_2$, O$_2$, N$_2$, CH$_4$ and CO$_2$ at 25 °C. Figure 5.8, Figure 5.9 and Figure 5.10 show the trends of the gas transport parameters of the membranes as cast (open symbols) and after PDMS coating (filled symbols) as a function of the AO-PIM-1 concentration in the membrane. The quantitative values are reported in Table 5.2.

Table 5.2 Permeability (Barrer), Diffusion (10^{-12} m^2 s^{-1}), Solubility (cm$^3_{STP}$ cm^{-3} bar^{-1}) coefficients and their respective selectivities of Matrimid®5218 and AO-PIM-1 blends membranes tested as cast and after PDMS coating.

Matrimid®5218 _AO-PIM-1	State	Permeability coefficient (Barrer)						$\alpha(P_x/P_{N2})$				
		N$_2$	O$_2$	CO$_2$	CH$_4$	H$_2$	He	O$_2$	CO$_2$	CH$_4$	H$_2$	He
100_00 [103]	AC	0.2	1.6	8.6	0.2	22.8	22	8.5	45.3	0.9	120	115
100_00_	AC	0.19	1.13	7	0.18	13.5	13.4	6.0	37.1	0.93	71.9	71.1
80_20	AC	/	1.8	10.6	/	12.6	10.8	/	/	/	/	/
	PDMS	0.26	1.6	9.7	0.24	19.9	19.4	6.2	37.1	0.92	76.1	74.1
60_40	PDMS	0.43	2.0	15.0	0.46	19.1	16.7	4.7	34.4	1.1	44.2	38.7
40_60	AC	0.42	2.3	17.2	0.57	20.3	17.7	5.4	41.4	1.4	48.6	42.5
20_80	AC	0.54	2.6	27.0	0.68	23.7	20.1	4.3	39	1.3	43.6	36.9
	PDMS*	0.79	4.2	33.0	0.92	37.0	29.0	5.3	41.7	1.2	47	36.9
00_100_ **	AC	4.8	19.9	178	6.3	133	83.2	4.2	37	1.3	27.8	17.4
00_100	AC	180	75.0	625	21.5	417	218	4.2	34.7	1.2	23.2	12.1
00_100 [107] ***		33	147	1153	34	912	412	4.5	35	1	27.6	12.5
		Diffusion coefficient (10^{-12} m^2 s^{-1})						$\alpha(D_x/D_{N2})$				
		N$_2$	O$_2$	CO$_2$	CH$_4$	H$_2$	He	O$_2$	CO$_2$	CH$_4$	H$_2$	He
100_000 [103]	AC	0.2	1.2	0.3	0.1	/	/	5.7	1.3	0.2	/	/
100_000_	AC	0.51	2.1	0.47	0.10	/	/	4.1	0.92	0.18	/	/
80_20	AC	/	/	/	/	/	/	/	/	/	/	/
	PDMS	0.65	2.9	0.60	0.11	208	849	4.4	0.93	0.17	318	1300
60_40	PDMS	0.88	2.9	0.90	0.20	243	612	3.3	1.0	0.23	275	670
40_60	AC	1.2	4.2	1.3	0.35	193	1365	3.5	1.0	0.29	160	1139
20_80	AC	0.91	3.1	1.1	0.23	158	625	3.3	1.2	0.25	173	650
	PDMS*	0.93	3.6	1.2	0.25	190	659	3.8	1.3	0.27	203	705
00_100_ **	AC	2.9	9.9	4.4	0.78	407	1003	3.4	1.5	0.27	141	347
00_100	AC	5.4	20.5	8.7	1.3	775	2381	3.9	1.6	0.25	134	116
00_100 [107] ***		9.9	40.6	24.6	2.6	/	/	4.1	2.5	0.26	/	/
		Solubility (cm$^3_{STP}$ cm^{-3} bar^{-1})						$\alpha(S_x/S_{N2})$				
		N$_2$	O$_2$	CO$_2$	CH$_4$	H$_2$	He	O$_2$	CO$_2$	CH$_4$	H$_2$	He
100_000 [103]	AC	0.7	1	23	3.5	/	/					
100_000_	AC	0.28	0.41	11.2	1.5	/	/	1.5	40	5.3	/	/
80_20	AC	/	/	/	/	/	/	/	/	/	/	/
	PDMS	0.30	0.42	12.1	1.6	0.07	0.02	1.4	40	5.3	0.24	0.06
60_40	PDMS	0.37	0.53	12.3	1.7	0.06	0.02	1.4	33.5	4.6	0.16	0.06
40_60	AC	0.26	0.40	10	1.2	0.08	0.01	1.5	38.3	4.7	0.30	0.04
20_80	AC	0.45	0.64	14.3	2.2	0.11	0.03	1.4	32	5	0.25	0.06
	PDMS*	0.63	0.88	19.8	2.8	0.15	0.03	1.4	31.3	4.4	0.23	0.05
00_100_ **	AC	1.3	1.5	30.2	6	0.25	0.06	1.2	24.2	4.8	0.20	0.05
00_100	AC	2.5	2.7	54	12.2	0.44	0.26	1.1	21.4	4.9	0.17	0.10
00_100 [107] ***		2.7	2.7	34.4	10	/	/	1.0	12.7	3.7	/	/

* aged 7 months ,   ** casted in DMSO,   ***Test and preparation conditions: T=35 °C, 2 bar; 24 h methanol soak; dried under vacuum at 120 °C for 24 h.

For unforeseen practical reasons, the membrane with 20% of AO-PIM-1 was tested only after 7 months of aging at ambient conditions, while the others were prepared shortly after preparation. In spite of all the care during the preparation, the membrane performance could be compromised by the presence of pinhole-defects due to dust particles. A common practise to reduce the effect of defects is to cover the membrane with a thin layer of highly permeable PDMS, which has no significant influence on the resistance to gas transport of the dense polymer membrane, but it reduces the low-selective Knudsen contribution to the overall mass transport.[110]
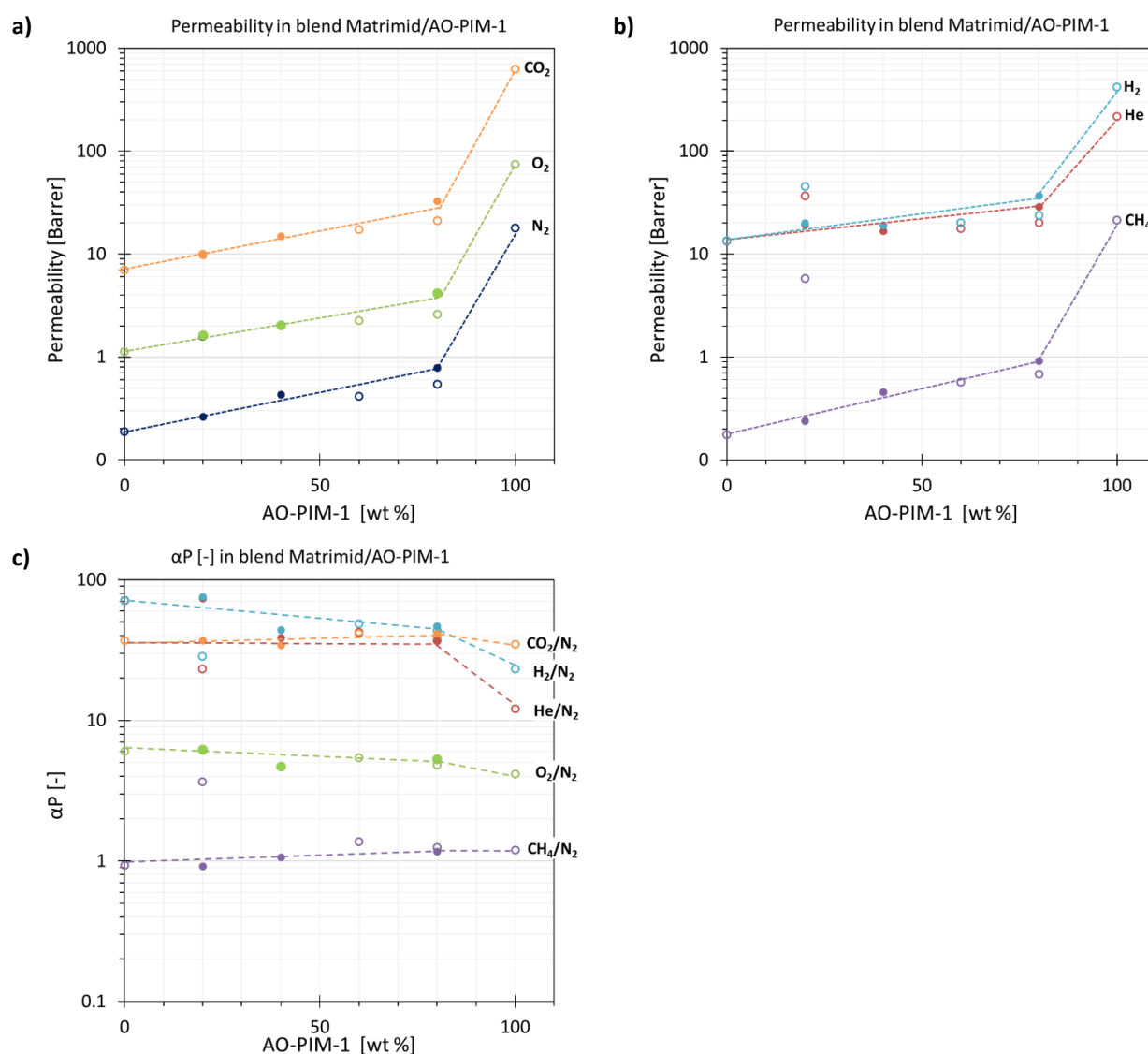
Figure 5.8 Permeability (a, b) and permselectivity (c) of six gases as a function of AO-PIM-1 content in Matrimid®5218 membranes. Open symbols indicate the as-cast membranes and filled symbols indicate the membranes coated with PDMS. Missing of the some open symbols is due to the presence of pinhole defects and therefore of high permeabilities and low selectivities. In these cases are reported the data 'fixed' with the silicone coating. Data of membrane with 20% is referred to sample aged 7 months. The lines are indicated as a guide to the eye.

The results highlight the different behaviour of Matrimid®5218 and the blends on the one hand, and pure AO-PIM-1 on the other hand. For all gases, the permeability gradually increases with the increasing PIM content (Figure 5.8a and b).

a)

b)
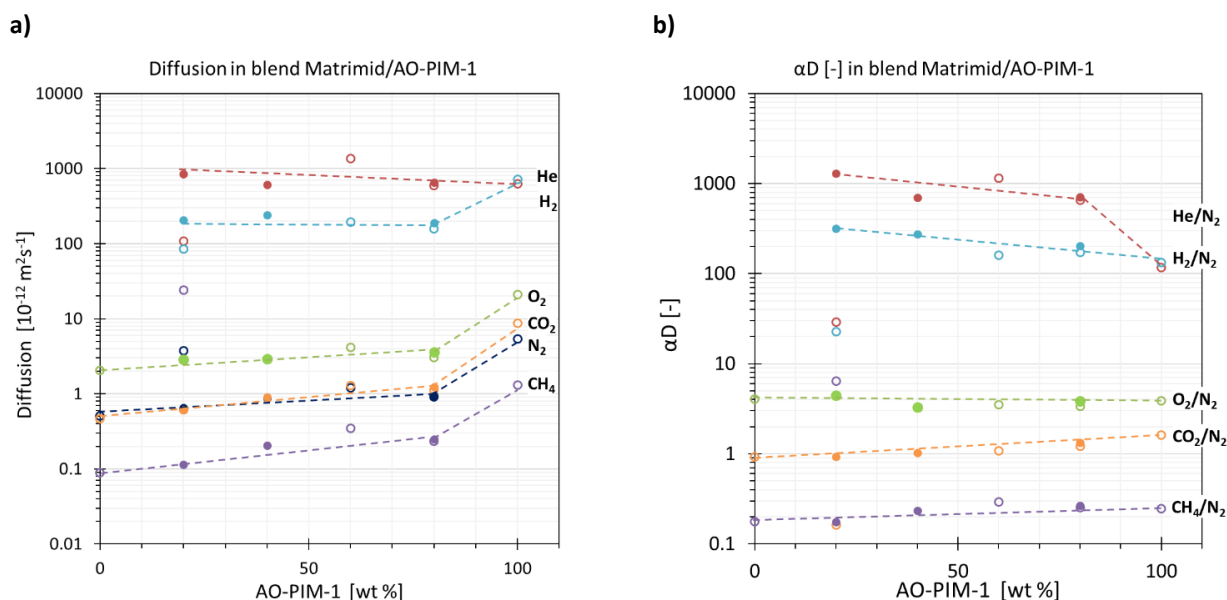
Figure 5.9 Diffusion (a) and diffusion selectivity (b) of six gases as a function of AO-PIM-1 content in Matrimid®5218 membranes. Open symbols indicate the as-cast membranes and filled symbols indicate the membranes coated with PDMS. Deviations from the trends of some open symbols is due to the presence of pinhole defects. Data of membrane with 20% is referred to a sample aged for 7 months. The lines are indicated as a guide to the eye.

Then there is a very strong and somewhat unexpected discontinuity, and the permeability of pure AO-PIM-1 is much higher. Moreover, some of the as-cast samples showed unreasonably high permeabilities and low selectivities, apparently due to the presence of pinhole defects. In these cases, the samples were successfully 'fixed' with the silicone coating, which plugs the defects. In most cases, the coated membranes have a lower permeability and higher selectivity. The permeability coefficients of the blend 20_80 after PDMS coating are higher than expected. The precise reason is unknown, but most likely slight swelling and subsequent shrinkage by absorption and desorption of the solvent has altered the contact between the PIM phase and the Matrimid® phase. Indeed, this is the membrane with apparently the most heterogeneous morphology and an apparently layered structure (Figure 5.5). The permselectivity is generally lower in AO-PIM-1, especially for gas pairs with very different kinetic diameters, like H_2/N_2 and He/N_2, Figure 5.8c. This is due to the different transport mechanism of H_2 and He in PIMs, [42] which sense the free volume differently, with higher interconnectivity.

As discussed previously, the incorporation of a high free volume PIM, such as AO-PIM-1, into Matrimid® is expected to give an overall increase in the FFV.[104] The high free volume in AO-PIM-1 and the micro phase separations present into the blends allow having a high diffusion coefficient that increases in the blend series with increasing PIM content, Figure 5.9a. For gases with large size, like CH_4 and CO_2, the diffusion selectivity with respect to N_2 decreases with AO-PIM-1 content, meanwhile it is mostly constant for O_2/N_2, Figure 5.9b. On the other hand, for small gases like H_2 and He the selectivity seems to decrease with increasing PIM content. This was found to be due to the fact that small molecules experience a more interconnected free volume than large molecules, in spite of the generally very high size-selectivity of PIMs with their highly rigid polymer structure.[42] The solubility increases linearly with the amount of AO-PIM-1 in the blend. The solubility selectivity of CO_2 and O_2 decrease with increasing of AO-PIM-1 content, it is almost constant for CH_4, Figure 5.10b. The time lag of H_2 and He is too short to be measured accurately in the thin pure Matrimid®5218 membranes, and thus the related diffusion coefficient and solubility coefficient are not determined.
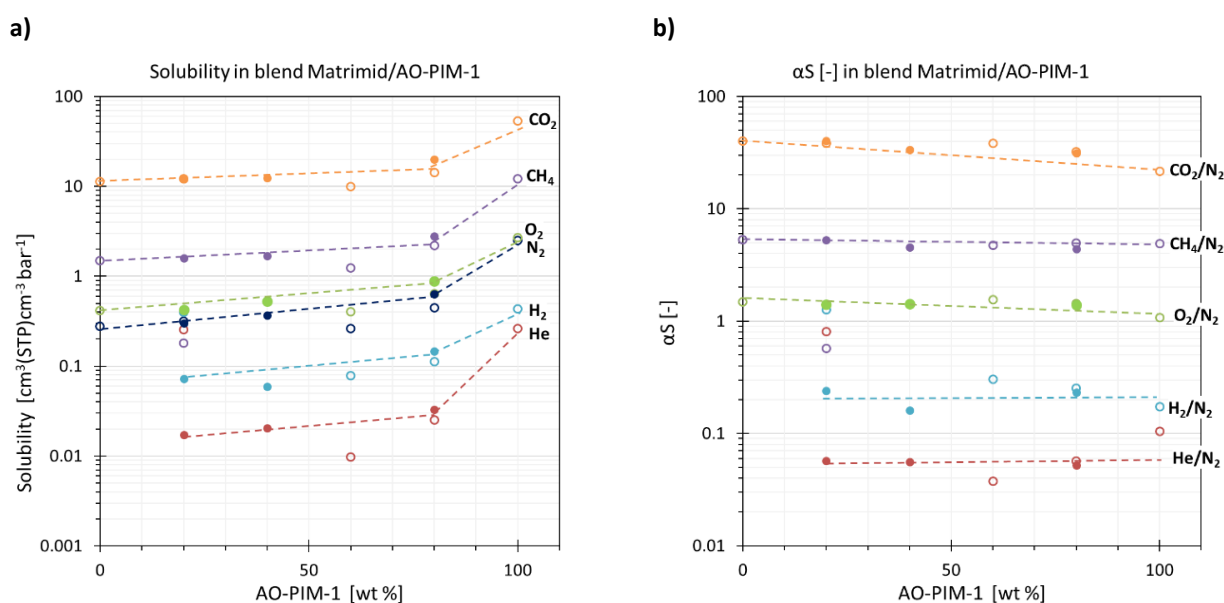
Figure 5.10 Solublity (a, b) and solubility selectivity (c) of six gases as a function of AO-PIM-1 content in Matrimid®5218 membranes. Open symbols indicate the membranes as cast and filled symbols indicate the membranes coated with PDMS. The lines are indicated as a guide to the eye.

Figure 5.11 shows the gas permeability data of neat Matrimid®5218, AO-PIM-1, and their blend membranes in the Robeson diagrams for CO_2/N_2, CO_2/CH_4, O_2/N_2 and H_2/N_2.
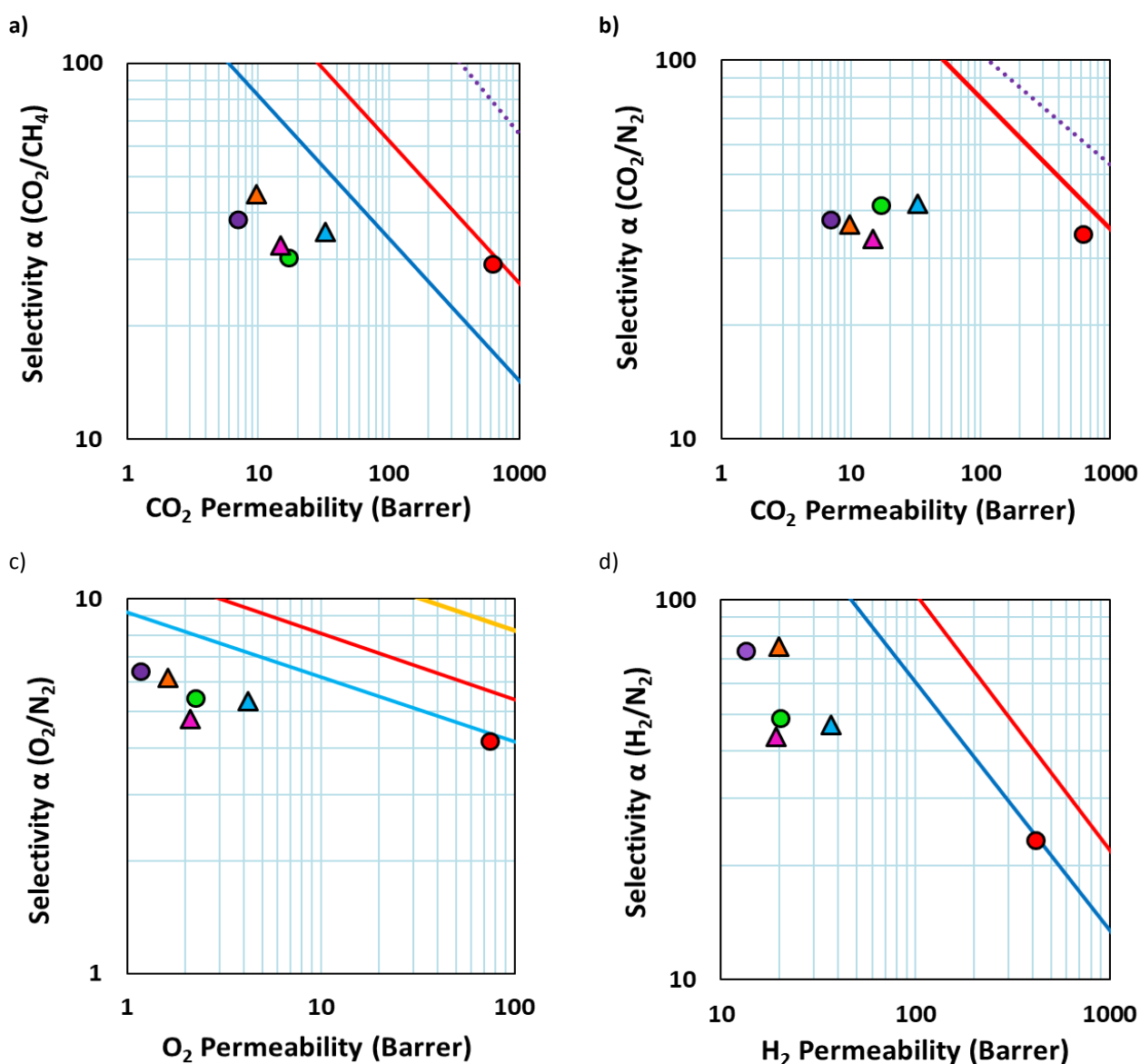
Figure 5.11 Robeson plots of membranes: ● pure AO-PIM-1, ● pure Matrimid®, ▲ Matrimid®_AO-PIM-1_20_80_PDMS_ aged 7 months, ● Matrimid®_AO-PIM-1_40_60, ▲ Matrimid®_AO-PIM-1_80_20_PDMS, ▲ Matrimid®_AO-PIM-1_60_40 for CO_2/CH_4 (a), CO_2/N_2 (b), O_2/N_2 (c) and H_2/N_2 (d) with the 1991 upper bounds indicated by a blue line, 2008 by a red line, 2015 by a yellow line, and 2019 by purple lines.

The general trend in the diagrams show an increase in the pure gas permeability, accompanied by a modest decrease in ideal selectivity compared to the neat Matrimid®. The CO_2/CH_4 selectivity of the blends is similar to that of neat Matrimid®5218, while the permeability increases only slightly (Figure 5.11). The higher CO_2/N_2 selectivity in Matrimid®, Figure 5.11b, must be ascribed mainly to the higher solubility selectivity, Figure 5.10b. The O_2/N_2 selectivity, Figure 5.11c, is higher in Matrimid®5218 due to a slightly higher solubility selectivity, whereas the diffusivity selectivity, Figure 5.9b, is roughly the same for both neat polymers and the set of blends. In general, the

selectivity is higher in Matrimid®5218, especially for gas pairs with very different kinetic diameters, like H_2/N_2, Figure 5.11d, mainly as a result of the much higher diffusion selectivity (Figure 5.9b).

The discontinuity in the permeability between the blends and the neat PIM suggests that even small amounts of Matrimid® apparently occupy most of the original free volume of the PIM, thus reducing drastically the permeability of the neat polymer. FT-IR analysis above confirmed the interaction between the two polymers and showed that at low Matrimid® content the carbonyl groups of the polyimide interact with the AO-PIM-1 matrix, resulting in a shift to slightly higher wave numbers.

Figure 5.12 shows the trends predicted by Eq. 5.1 and Eq. 5.2. The limited miscibility of the two blend components is the main reason for the deviations of permeability from the logarithmic trend predicted by Eq. 5.1, which is unsuitable in this case. Indeed, a more appropriate model for immiscible blends is the Maxwell model (Eq. 5.2). The Maxwell model was used because of its simplicity and the absence of adjustable parameters, although more sophisticated models may be more suitable that account for the non-uniform size and shape of the dispersed phase.[111]
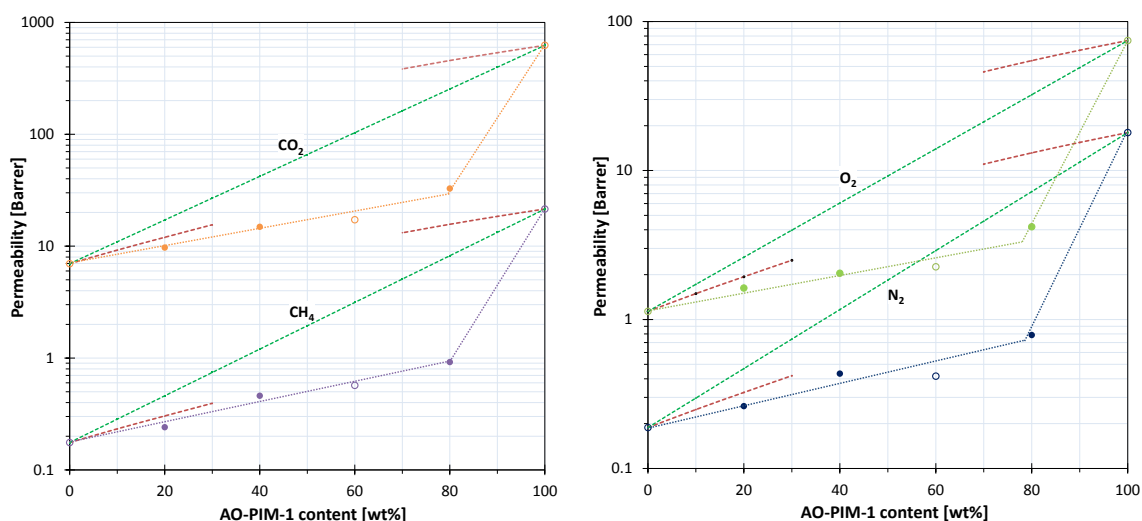
Figure 5.12 Experimental permeability of CO_2, CH_4, O_2 and N_2 as a function of the Matrimid®/AO-PIM-1 blend composition, and comparison with the logarithmic model for miscible blends (Eq. 5.1, green dashed line) and the Maxwell model (Eq. 5.2, red dashed lines, indicated within the limits of its validity). Open symbols indicate the as cast membranes and filled symbols indicate the membranes coated with PDMS, in case healing was needed.

Although other models may be suitable for higher loadings or non-spherical dispersed phases [112], the simple Maxwell model describes the transport properties quite satisfactorily at low AO-PIM-1 concentration in the blend, up to ca. 40 wt%, as shown for CO_2, CH_4, O_2 and N_2 in Figure 5.12. We may assume that AO-PIM-1 is the dispersed phase in this range, and the Maxwell model fits the experimental data best for CH_4, while it slightly overestimates the data for CO_2, O_2 and N_2. On the other hand, the presence of low amounts of Matrimid® in AO-PIM-1 dramatically reduces the permeability of the PIM, suggesting that the first and most important effect of Matrimid® is to occupy the free volume of the PIM. Therefore, the trend deviates completely from the Maxwell model for PIM percentages higher than 60%, where Matrimid® is assumed to be dispersed or dissolved in AO-PIM-1. The phase behaviour could be confirmed by analysis of the additive (or non-additive) behaviour of the density, but the reported densities of Matrimid® and AO-PIM-1 reported, 1.24 g cm^{-3} [113] and 1.18 g cm^{-3} [114], respectively, are too similar in this case. Therefore, it is not possible to verify the phase behaviour of the two polymers accurately with the help of their density, and the permeability appears to be much more sensitive, and decisive in combination with SEM analysis.

To some extent, the deviation from the trend might also be due to slight differences in the degree of physical aging in the samples, typically observed for PIMs but to a lesser extent in common glassy polymers with lower free volume. This could not be investigated systematically with the present blends, because the commonly used alcohol treatment to reset the casting history damaged the heterogeneous films with their different degrees of swelling of the two phases. In any case, aging is much slower in as-cast membranes [82] and therefore we believe that this effect is of minor importance.

5.3 Conclusion and future perspectives

The performance of the heterogeneous Matrimid®5218/AO-PIM-1 blends was evaluated in terms of their pure gas permeation properties. The newly developed blend membranes show intermediate gas transport properties between those of Matrimid®5218 and AO-PIM-1, with diffusivity coefficients that increase with increasing PIM content in the blend. This is ascribed to the presumed increase of free volume by the presence of AO-PIM-1 in the Matrimid® and is further supported by

the trends in solubility and permeability. The permeability at low PIM contents (< 40%) is described fairly well by the Maxwell model for CH_4, while the experimental values are somewhat lower than the model for CO_2, O_2 and N_2. At higher AO-PIM-1 content, assuming Matrimid® as the dispersed phase, the experimental permeability is much lower than the predictions by the Maxwell model and even lower than the predictions by the miscible blend model, which are both inadequate. In all cases, blend membranes exhibit a higher permselectivity than pure AO-PIM-1. The best performing blend membrane is the one with the smallest amount of PIM (Matrimid®5218_AO-PIM-1_80_20). For this membrane the permeability increases substantially, whereas the permselectivity remains the same as in Matrimid®5218. Therefore, the AO-PIM-1 offers the possibility to increase the permeability of Matrimid®5218, maintaining a reasonably high selectivity. The unexpectedly low permeability of AO-PIM-1 with a low amount of Matrimid® may be related to specific interactions of the functional groups in Matrimid® and the polar AO group in the PIM. The relatively strong decrease in the diffusion coefficient is apparently due to a significant loss of the intrinsic microporosity and free volume.

Comparison of the two models defined, show that in immiscible blends, following the Maxwell model, small amounts of the PIM improve the permeability of the low-permeable polymer bulk much less than in miscible blends. More effort is therefore needed to find a compatible polymer for AO-PIM-1. Since large domains were formed upon slow evaporation of the solvent, this suggests that the morphology may be finer in the case of a higher evaporation rate, for instance when preparing thin film composite membranes. This may be a topic for further studies in order to evaluate whether a fine microstructure could improve the transport properties.

Approaches to machine learning.[8]

---

[8] Parts of this chapter are based on the manuscript: [121] Q. Yuan, **M. Longo**, A.W. Thornton, N.B. McKeown, B. Comesaña-Gándara, J.C. Jansen, K.E. Jelfs, **Imputation of missing gas permeability data for polymer membranes using machine learning**, J. Memb. Sci. 627 (2021) 119207. https://doi.org/10.1016/j.memsci.2021.119207. (Preprint from: [136] ChemRxiv, 22 Oct 2020. https://doi.org/10.26434/chemrxiv.13124993.v1)

6.1 Introduction

In the previous two chapters it is shown how the gas permeability of PIMs depends on the polymer structure, on the polymer blend composition and on the sample history. For the design of novel materials, it would be useful to know such relationships and even to be able to predict them. This requires the precise knowledge of the structure-property relationships of the materials, based on a large number of available data. It also requires the availability of versatile computational methods to correlate these structure-property relationships with the structures of newly designed materials. The use of machine learning in computational molecular design has great potential to accelerate the discovery of innovative materials, and to make predictions on properties based on an already known set of data.[115] This chapter will briefly describe the development of a machine-based learning approach for the prediction of gas separation properties of polymeric membranes.

6.1.1 Machine learning and gas permeability

The machine intelligence is applied to intellectually demanding tasks across various fields using a massive amount of data, and in principle can match or even outperform humans. Thus, there is increasing attention in the use of machine learning (ML) to save substantial time and cost for the designing of new materials and in the prediction of materials properties. Machine learning (ML) methods have been developed and applied to polymers for predicting various properties, including the gas permeability.[115] One of the most commonly used methods for predicting gas transport parameters (permeability and diffusion coefficients) of glassy polymers is the group contribution theory, where additivity rules govern. For this method the chemical structure of a polymer is divided into smaller fragments and the fragments are used in various ML models as input features. [116,117] Such models were built upon chemical structures of polymers and are of great value for identifying structure-property relationships. This method can be used to 'design' novel polymers in order to optimize the gas transport properties, but it has a limited applicability if there is not a sufficient number of data available for polymers having different chemical structures.[118] An alternative way is imputing the database to predict the permeability of unknown gases based on data for gases with known permeability. As suggested by Alentiev *et al.,* [119] the logarithm gas permeability coefficients of two gases are strongly correlated, while Malykh *et al.* correlate even three

permeabilities or one permeability and two selectivities. [120] Thus. it is possible to predict the gas permeability of a gas using the permeability data for other gases without requiring any information on the molecular structure of the polymers or experimental conditions. In statistics, imputation is used to replace missing data to get a more complete database for future experimental and theoretical study.

The initial intent of this work was to perform permeability prediction of novel polymers via the construction of a database with all the known gas permeation data in PIMs, and via the development of a ML model. However, this proved a difficult task considering the relatively small number of molecular structures of PIMs already present in the literature, since this results in a limited amount of training data, which in its turn makes these methods impractical or too inaccurate for prediction. Thus, the data set was enlarged using the *Gas Separation Membrane Database of the Membrane Society of Australasia* (*MSA*), which includes data for over 1500 polymer films published from 1950 to 2018. [22] The database of membrane gas permeation measurements contains different gases including hydrogen, oxygen, nitrogen, carbon dioxide and methane. The membrane materials include a range of rubber and glassy polymers, carbon sieves, zeolites and mixed composites. However, the data set is not fully filled since experimental measurements are not always performed for all the gases included in the database. Experimental measurement of the missing gas permeability of previously reported polymers would be time consuming and expensive, especially when the permeability against aging needs to be tested. It is thus necessary to develop an easily accessible computational model to estimate the permeability of certain gases when the experimental data were not performed, while those of other gases are available. In this work, ML models were developed to "learn" the relationship of permeability of different gases recorded in the Polymer Gas Separation Membrane Database and impute the missing gas permeability in the database using the ML models. An overview of the approach is shown in Figure 6.1. The imputation model was validated with published data that are not included in the database as a test set, indicating that it is a powerful tool for examining the gas permeability of a novel polymer at an initial experimental stage, when not all gas permeability data are available. This model gives also the possibility to uncover additional, but previously unknown, properties of existing polymers in the database. It is not the aim of this work to discover any novel gas selective polymers in this paper; however, the open-source ML model presented could be used in the future to impute the gas

permeability data of novel polymers at an early stage of experimental measurements and thus help to accelerate the identification of polymer membranes worth further experimental investigation.
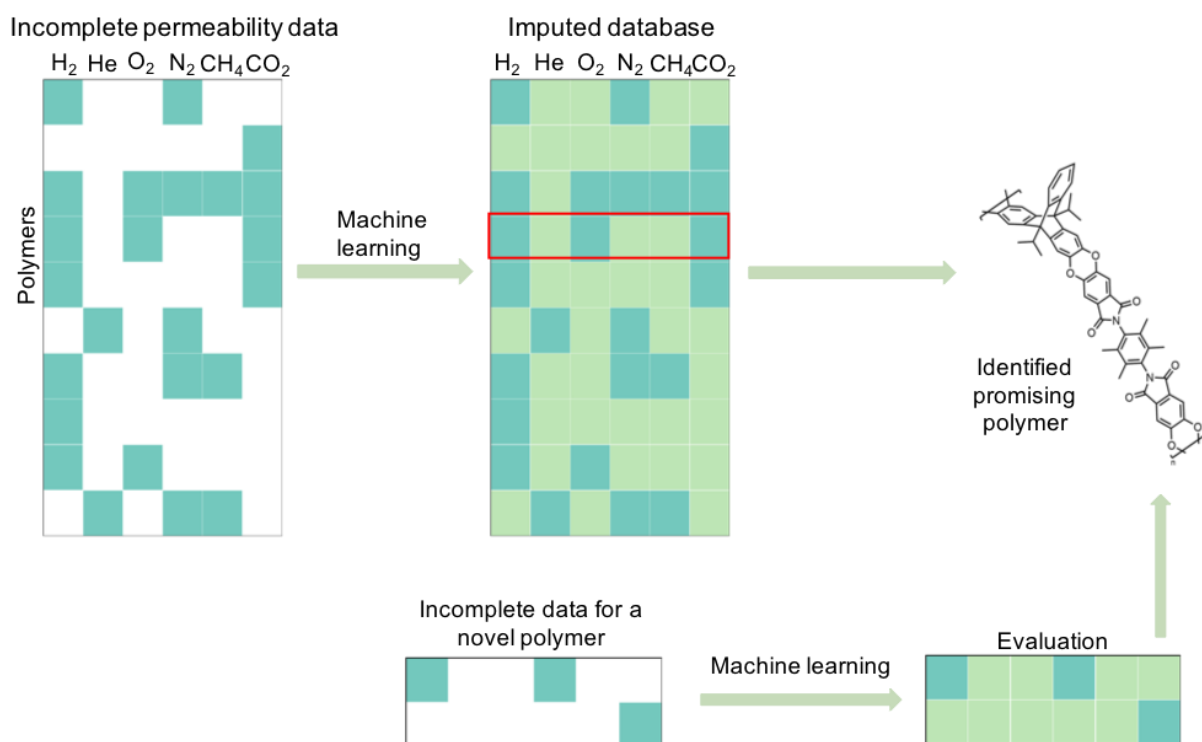
Figure 6.1 Overview of our workflow. [121] It is imputed the existing Polymer Gas Separation Membrane Database [https://membrane-australasia.org/msa-activities/polymer-gas-separation-membrane-database/] using machine learning, where previously reported polymers in the database that miss gas permeability values can be re-analysed and these gaps filled. An imputed database opens the potential for identifying promising polymers and the developed machine learning model has the potential to take incomplete datasets for novel polymers and impute them in seconds to allow the evaluation of which systems should be the focus of continuing experimental effort.

6.2 Methods

The focus of this work was on commonly measured gases, i.e. He, H_2, O_2, N_2, CO_2 and CH_4. The initial database was downloaded from the MSA website in 2019, and the datasets of polymers that did not contain at least one of the gases of interest were removed from the database. The final database includes 1,378 entries, and the number of missing values for the permeability of each gas is shown in Table 6.1.

The gas permeability, usually reported in Barrer, in this study is converted to logarithm with base 10 values, since the logarithm values are used to define the empirical Robeson upper bounds of gas selectivity. [33,34] Missing value imputation of the *Polymer Gas Separation Membrane Database*

was performed using the Multivariate Imputation by Chained Equations (MICE), which 'fills in' the missing data in a dataset through an iterative procedure of predictive models.[122] In each iteration, the missing values of a specific variable are predicted with the predictive model using other variables in the dataset. For this work two predictive models were selected: the Bayesian Linear Regression (BLR)[123] and the Extremely Randomized Trees (ERT).[124] Predictive performance of these two models on the test set were compared. The BLR is an approach for linear regression where the statistical analysis is undertaken with Bayesian inference in which the probabilities are not interpreted as frequencies or simple proportions, but rather as confidence levels in the occurrence of a given event. The name derives from Bayes' theorem, the foundation of this approach. Decision tree learning is one of the predictive modelling approaches used in statistics and machine learning. It uses a decision tree (as a predictive model) to go from observations about an item (represented in the branches) to conclusions about the item's target value (represented in the leaves). An ensemble of individual trees is defined a random decision forest. The ERT is a sort of random forest and its prediction accuracy and the control of the over-fitting depends on the number of randomized decision trees implemented into the method. The over-fitting is the production of an analysis too closely or exactly to a particular set of data, which fail to fit additional data or predict future observations reliably. In this study, the ERT model was composed of 100 decision trees. The missing value imputation of the *Polymer Gas Separation Membrane Database* was performed using Python 3.7.1 and Scikit-learn 0.21.2.[125]

Table 6.1 Number of missing values for the gas permeability in the *Polymer Gas Separation Membrane Database* of each gas. In this study, the total number of data points for the permeability of each gas is 1,378.

Gas	He	H_2	O_2	N_2	CO_2	CH_4
Number and percentage of missing values	620 (45%)	608 (44%)	102 (7%)	123 (9%)	165 (12%)	341 (25%)

The performance of the ML models to predict the permeability data in these polymers was tested via two different tests. In the first test, the permeability data of H_2 was removed from the test database, and the data of H_2 was modelled as a function of the other gases in the test database. In the second test, to examine the ability of the imputation models for cases where limited permeability data is available, the gas permeability data of only one gas was used to predict the permeability for all other gases, for example, predicting the gas permeability of He, O_2, N_2, CH_4 and

CO_2 using the gas permeability data of H_2 only. The performance of the ML model on the test set is quantified by the rooted mean squared error (RMSE) between the logarithm gas permeability obtained by ML prediction and the experimentally reported values, as defined in Eq. 6.1:

$$RMSE = \sqrt{\frac{\sum_{i=1}^{n}(p_i - \hat{p}_i)^2}{n}}$$

Eq. 6.1

where *n* is the number of data points, p_i is the experimentally reported logarithm gas permeability of polymer *i,* and $\hat{p}_i$ is the logarithm gas permeability of polymer *i* prediction using the ML model.

The ability of the ML models to predict the gas selectivity of polymers was measured by a classification problem, where the ML models were used to predict the permeability of a gas pair and then tested whether the polymers in the test set had gas selectivity beyond the Robeson 2008 upper bound. The classification means that polymers with gas selectivity above the Robeson 2008 upper bound were regarded as "*positive*", while those below the Robeson 2008 upper bound were regarded as "*negative*". The gas permeabilities of polymers were evaluated using the ML models to determine if they were predicted "*positive*" or "*negative*" in the Robeson diagram. "*True positive*" represents polymers that were positive from both experimental measurements and ML prediction; "*False positive*" represents polymers that were positive from ML prediction but negative from experimental measurements; "*True negative*" represents polymers that were negative from both experimental measurements and ML prediction, and "*False negative*" represents polymers that were negative from ML prediction but positive from experimental measurements. It is computed the accuracy, precision, and recall scores for identifying the polymers with gas selectivity above the Robeson 2008 upper bound. In this study, accuracy refers to the fraction of correct predictions from all predictions made, precision refers to the fraction of "*true positive*" values from values that were predicted as "positive", and recall refers to the fraction of "*true positive*" values from all values that were "positive" experimentally. The accuracy, precision and recall scores are defined as:

$$Accuracy = \frac{True\ positive + True\ negative}{Size\ of\ test\ set}$$

Eq. 6.2

$$Precision = \frac{True\ positive}{True\ positive + False\ positive}$$

Eq. 6.3

$$Recall = \frac{True\ positive}{True\ positive + False\ negative}$$

Eq. 6.4

6.3 Validation of the imputation models on the test set

For the validation of the imputation model have been selected data not recorded in the *Polymer Gas Separation Membrane Database* for PIMs [36,126,127] and polyimides [128–133], as shown in Figure 6.2. The test set contained experimental gas permeabilities of 50 PIMs and 37 polyimides. The test set is a diverse dataset in terms of both polymer structure and the range of gas permeability and selectivity, where PIMs exhibit higher gas permeability compared to polyimides. Performance of the BLR and ERT imputation models was compared by computing the RMSE between "predicted" logarithm gas permeability and the experimental logarithm gas permeability reported in the literature.
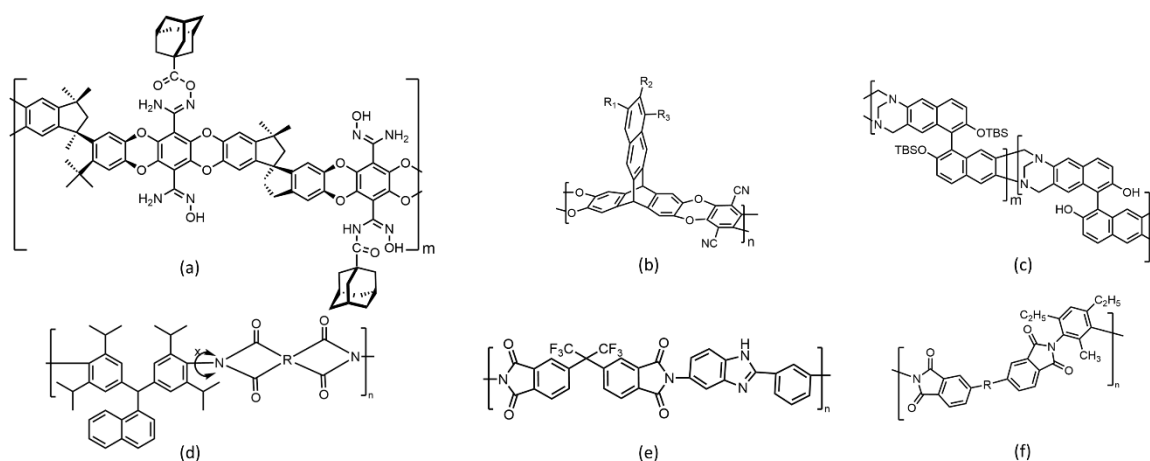
Figure 6.2 Representative structures of PIMs (a-c) and polyimides(d,e) in the test set. (a) Adamantane-grafted PIM;[126] (b) Benzotriptycene-based PIM;[36] (c) OH-functionalized Tröger's base-based PIM;[127] (d) Microporous polyimides containing bulky tetra-o-isopropyl and naphthalene groups; [128] (e) Imidazole containing polyimide;[133] (f) Polyimides based on the diethyltoluenediamine isomer mixture.[129]

According to Table 6.2, the BLR model is more accurate in the predictions for the gas permeability of PIMs than the ERT model, while the performance of the two models are comparable for polyimides, except that the ERT model had significantly larger errors for the H_2 permeability. The BLR model is more accurate than the ERT model in general on the test set with "dense features" (where the permeability of one gas was predicted using the permeabilities of all other gases). Correlation of the experimentally reported gas permeability and the BLR model predictions is shown in Figure 6.3. According to Table 6.2 and Figure 6.3, the BLR model had the largest error in predicting the CH_4 and CO_2 permeability, and the smallest in O_2 permeability. From Figure 6.3 it can be seen

that the BLR model systematically underestimated the CO_2 permeability for almost all the entries in the test set, while no obvious systematic error is observed for CH_4 permeability.

Table 6.2 RMSE between the BLR and ERT predicted gas permeability and experimental results in logarithm Barrer. The smaller RMSE values among the two models are in bold.

	He	H_2	O_2	N_2	CH_4	CO_2
BLR/PIMs	**0.04**	**0.05**	**0.03**	**0.07**	**0.10**	**0.12**
ERT/PIMs	0.08	0.14	0.04	0.11	0.15	0.13
BLR/polyimides	**0.11**	**0.10**	**0.07**	0.09	0.17	0.11
ERT/polyimides	0.13	0.19	0.08	0.09	**0.16**	**0.10**
BLR/average	**0.06**	**0.07**	**0.05**	**0.08**	**0.13**	0.12
ERT/average	0.10	0.16	0.06	0.10	0.16	0.12
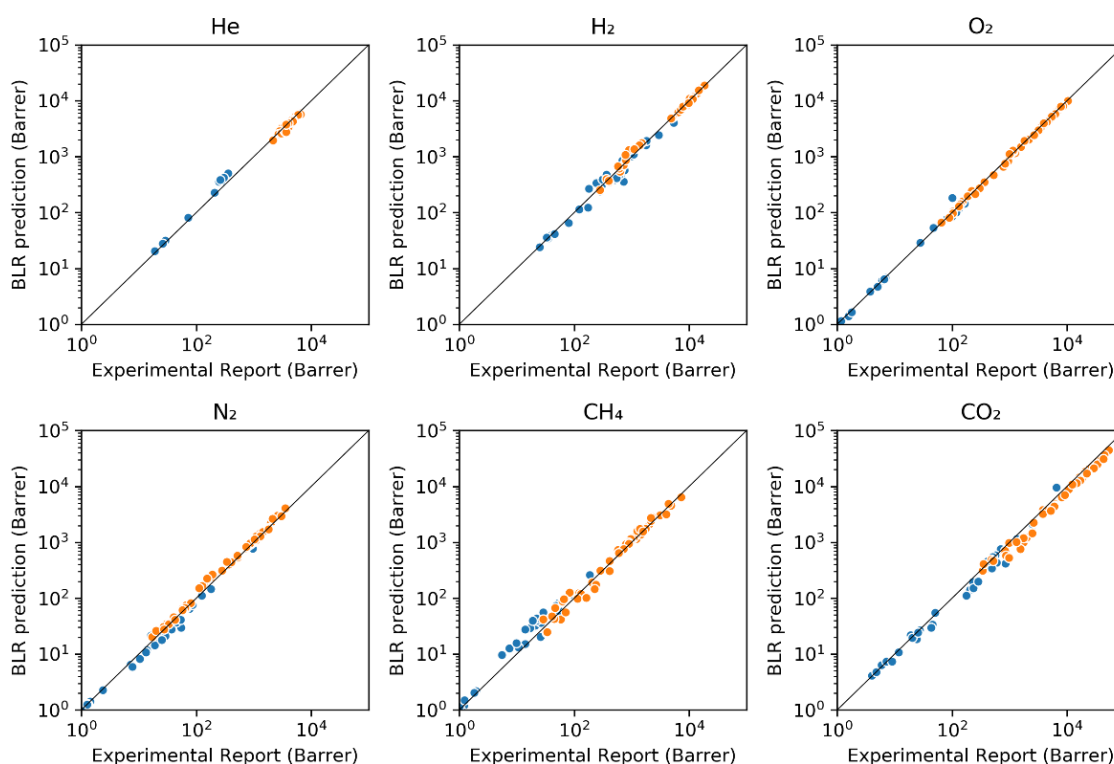
Figure 6.3 Correlation of BLR prediction and the experimental report of the gas permeability of PIMs (orange data points) and polyimides (blue data points) in the test set.

For the design of new membranes, the most important objective is to have a high permeability in combination with a high selectivity for the gas pair of interest, which can be examined from the Robeson diagram. The performance of the imputation models was measured using the two-class classification task described in section 6.2: polymers with gas selectivity above the Robeson 2008 upper bound were regarded as "positive", and those below the Robeson 2008 upper bound were

regarded as "negative". For both the BLR and ERT model, the gas permeabilities of interest were calculated using the permeability of all available gases, and the positions of the calculated values in the Robeson diagram were computed. The accuracy, precision and recall scores for the BLR and ERT prediction were calculated using equations Eq. 6.2, Eq. 6.3 and Eq. 6.4.

Two of the most reported gas pairs, CO_2/CH_4 and CO_2/N_2, were considered, and three cases of gas permeability missing for each gas pair were simulated. For the CO_2/CH_4 selectivity, for example, it was applied the imputation model to the test set under three parallel assumptions: the permeability for both CO_2 and CH_4 are missing; only the permeability for CH_4 is missing; and only the permeability of CO_2 is missing. For all three cases, it was evaluated the missing gas permeabilities using the permeabilities of all other gases (dense features), and the accuracy, precision and recall scores for the BLR and ERT prediction of CO_2/CH_4 and CO_2/N_2 selectivity are shown in Table 6.3,

Table 6.3 Accuracy, precision, and recall score for the BLR and ERT model in predicting the polymers with gas selectivity above the 2008 Robeson upper bound with permeabilities of different gases missing: the accuracy, precision and recall scores are in the range of 0-1, where the closer a number is to 1, the better the model.

Model	Gas Pair	Missing Permeability	Accuracy	Precision	Recall
BLR	CO_2/CH_4	CH_4 and CO_2	0.89	1.00	0.76
		CH_4	0.95	1.00	0.90
		CO_2	0.91	1.00	0.81
	CO_2/N_2	N_2 and CO_2	0.83	1.00	0.59
		N_2	1.00	1.00	1.00
		CO_2	0.92	1.00	0.81
ERT	CO_2/CH_4	CH_4 and CO_2	0.79	1.00	0.57
		CH_4	**0.94**	**1.00**	**0.88**
		CO_2	0.93	1.00	0.86
	CO_2/N_2	N_2 and CO_2	0.77	0.95	0.49
		N_2	**0.90**	**0.97**	**0.78**
		CO_2	0.85	1.00	0.65

The accuracy scores of the BLR model for both gas pairs in all three cases are higher than 0.8. It should be noted, however, for cases where the permeability for both CO_2 and CH_4 (similarly for both CO_2 and N_2) are missing, the precision scores and recall scores are rather imbalanced: the precision for almost all predictions in Table 6.3 is close to perfect, while the recall score were 0.76 and 0.59 for CO_2/CH_4 and CO_2/N_2, respectively. Such an imbalance indicates that the imputation models are

"useful" but not "complete" for cases where the permeability data for both gases of interest is missing: polymers predicted to have good gas selectivity are highly likely to be gas selective following experimental measurements, however, a considerable percentage of the polymers with good gas selectivity are misclassified as "negative" by the BLR model.
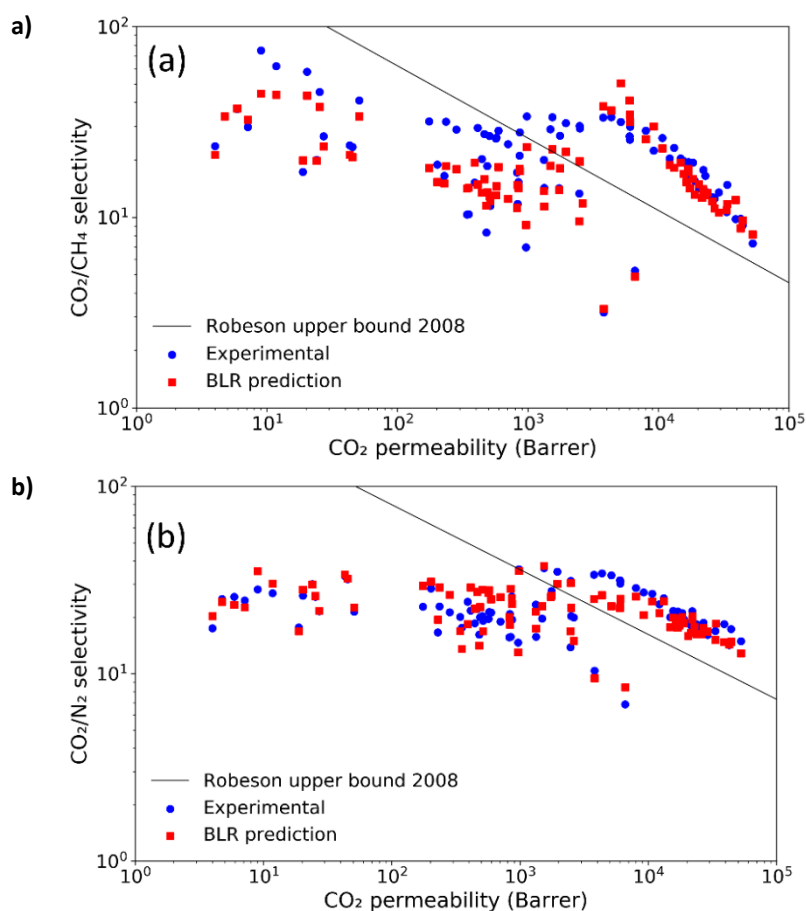
Figure 6.4 BLR prediction and experimental reports of the CO_2/CH_4 and CO_2/N_2 selectivity in the Robeson diagram, with the cases for (a) permeability data of CH_4 missing; (b) permeability data of N_2 missing.

For cases where the permeability of one gas (CO_2 or CH_4 for the selectivity of CO_2/CH_4) is missing, the BLR model is much more robust compared to the cases where permeability data of both gases is missing, where the accuracy, precision and recall scores ranged from 0.80 to 1.00. It should also be noted that in Table 6.3, for CO_2/CH_4 and CO_2/N_2, the accuracy, precision and recall scores were all higher than 0.90 for cases when the only missing data was the CH_4 or N_2 permeability. For such cases, the imputation models are both "useful" and "complete": robust predictions about the gas selectivity can be made if the permeability for only CH_4 or N_2 is missing. The experimentally

measured and BLR predicted positions of data points in the test set for cases where only the CH_4 or N_2 permeability is missing are shown in Figure 6.4.

The data cloud of the BLR prediction for both CO_2/CH_4 and CO_2/N_2 overlapped with the experimental reports greatly, which is in agreement with the high accuracy, precision and recall scores for the corresponding cases. It is thus possible to identify the future polymers with high gas selectivity when not all the gas permeability data is available, or to evaluate the gas selectivity of a previously reported polymer when the gas permeability data is missing for one or more gases. The CO_2/CH_4 and CO_2/N_2 selectivity for polymers has been studied extensively, and it is believed that mobility and sorption both favour the permeation of CO_2 and so making predictions with this pair is probably relatively easy. It was also investigated the selectivity of H_2/CO_2 using the test set, where sorption and mobility selectivity are opposed for this gas pair. The accuracy, precision and recall scores for identifying polymers against the Robeson 2008 upper bound are shown in Table 6.4. These scores were all above 0.83 for prediction when H_2 permeability is missing, while for cases when CO_2 or both CO_2 and H_2 permeability data is missing, the precision of the imputation model decreased considerably. Therefore, our imputation model can be used to evaluate the H_2/CO_2 selectivity without experimentally measuring the H_2 permeability.

Table 6.4 Accuracy, precision, and recall score for the BLR in predicting the polymers with H_2/CO_2 selectivity above the 2008 Robeson upper bound with permeabilities of different gases missing: the accuracy, precision and recall scores are in the range of 0-1, where the closer a number is to 1, the better the model.

Model	Gas Pair	Missing Permeability	Accuracy	Precision	Recall
		H_2 and CO_2	0.88	0.52	1.00
BLR	H_2/CO_2	H_2	0.96	0.83	0.90
		CO_2	0.85	0.45	1.00

6.4 Prediction of gas permeability from a single measurement

During the experimental testing of gas selectivity of new polymers, the gas permeability is usually measured sequentially, and these measurements take considerable time and effort. As described in section 2.2, the minimum duration of an experiment depends mainly on the time needed to reach steady state permeation (see for instance Figure 2.2) and this, in turn, depends on the membrane thickness and on the diffusion coefficient of the gas because the time lag increases with the square of the membrane thickness and with the reciprocal of the diffusion coefficient (see Eq. 2.9). For

highly size-selective polymers, the measurement time may become extremely long for relatively large gas molecules like CH_4, because of their low diffusion coefficient,[42] and it may become attractive to predict rather than measure the permeability of the slowest gases. Thus, to simulate the scenario where the permeability of CO_2 has been experimentally measured and one needs primary insight into the CO_2/CH_4 and CO_2/N_2 selectivity, the BLR and ERT predictors were used to impute the test set with sparse features, in which the gas permeability data of all are removed but one gas and the permeability of that one gas is used to predict the permeability for all the other gases. The correlation between gas permeability of pairs of gases can be observed from the RMSE results in Table 6.5.

Table 6.5 RMSE of the BLR and ERT predicted gas permeability in logarithm Barrer against the experimental reports in the test set. Each column corresponds to a completed imputation using the permeability of only the gas in that column as input. The RMSE values in bold shows the best 'feature' in predicting the gas permeability of the corresponding 'target'.

		Feature					
		He	H_2	O_2	N_2	CH_4	CO_2
BLR Target	He	-	**0.05**	0.26	0.43	0.59	0.27
	H_2	0.62	-	**0.23**	0.41	0.58	**0.23**
	O_2	0.82	0.24	-	0.23	0.46	**0.10**
	N_2	0.93	0.46	**0.24**	-	0.31	0.28
	CH_4	1.05	0.63	0.42	**0.19**	-	0.47
	CO_2	0.89	0.23	**0.11**	0.3	0.51	-
	Average	0.86	0.32	**0.25**	0.31	0.49	0.27
ERT Target	He	-	**0.10**	0.26	0.65	0.91	0.29
	H_2	0.41	-	**0.27**	0.64	0.93	0.29
	O_2	0.47	0.26	-	0.36	0.62	**0.13**
	N_2	0.46	0.43	0.24	-	0.39	**0.15**
	CH_4	0.58	0.55	0.50	0.33	-	**0.30**
	CO_2	0.76	0.32	**0.11**	0.39	0.67	-
	Average	0.54	0.33	0.28	0.47	0.70	**0.23**

For example, it can be observed that the permeability of H_2 and He are strongly correlated, since the permeability of H_2 solely is a strong feature in predicting the permeability of He, with RMSE of 0.05 and 0.10 for the BLR and ERT model, respectively. The permeability of He, on the other hand, is a rather weak feature in predicting the permeability of other gases. This is mostly due to the lack of sufficient experimental data for He permeability in the membrane database, and therefore in our

test set. Indeed, 48% of the polymers in the test set lack the experimental He permeability, thus permeability of He is a weak feature for a machine learning model. With more data points for the permeability of He experimentally measured and reported in the future, it would be possible to improve the predictive power using He. With the imputation using sparse features, O_2 and CO_2 permeability was the strongest indicator of the permeability of the other gases. According to Table 6.5, the average RMSE of the BLR model for predicting permeability of other gases using data for O_2 and CO_2 are 0.25 and 0.27; and the RMSE of the ERT model using data for O_2 and CO_2 are 0.28 and 0.23, respectively. The order of reliability of prediction from permeability of a single gas for the BLR model is $O_2 > CO_2 > N_2 > CH_4 > He$, and the order of reliability for the ERT model is $CO_2 > O_2 > H_2 > N_2 > He > CH_4$.

To simulate the scenario where the experimental permeability of a new polymer for only one gas has been measured and one wants to evaluate the gas selectivity of the polymer without experimentally measuring the gas permeability of the other gases. It was examined specifically the performance of CO_2 permeability in predicting whether the polymer is above the Robeson 2008 upper bound for CO_2/CH_4 and CO_2/N_2. The accuracy, precision and recall scores for the BLR and ERT prediction of CO_2/CH_4 and CO_2/N_2 selectivity using only CO_2 permeability are shown in Table 6.6.

Table 6.6 Accuracy, precision, and recall score for the BLR and ERT model in predicting the polymers with gas selectivity above the 2008 Robeson upper bound using only the permeability of CO_2, the "sparse feature": the accuracy, precision and recall scores are in the range of 0-1, where the closer a number is to 1, the better the model.

Model	Gases	Accuracy	Precision	Recall
BLR	CO_2/CH_4	0.52	0.00	0.00
	CO_2/N_2	0.64	1.00	0.16
ERT	CO_2/CH_4	0.84	1.00	0.66
	CO_2/N_2	0.89	0.90	0.81

The ERT model outperformed the BLR model for both the selectivity of CO_2/CH_4 and CO_2/N_2 in the "sparse feature" case. It should be noted that for the BLR model, the recall scores are very low, and the precision and recall for CO_2/CH_4 are both 0.00, which indicates that according to the BLR model, all polymers in the test set are "negative". The ERT model, on the other hand, yields robust prediction scores for both the CO_2/CH_4 and CO_2/N_2 selectivity, except that the recall score for

CO_2/CH_4 selectivity is moderate. The reason for the ERT model in outperforming the BLR model in the "sparse feature" case might be that the linear BLR model learned a stricter relationship between the pairwise gas permeability from the *Polymer Gas Separation Membrane Database*. This enabled accurate prediction of gas permeability in the "dense feature" case, however limited the generalizability of the model in the "sparse feature" case.

It should be noted that the ERT model is not deterministic and might give slightly varied results from different runs if different random seeds are used. In this study, the ERT model was built using the combination of 100 decision trees, which reduced the probability of high variance in the predictions. In addition, parallel ERT tests with different random seeds were performed and the RMSE across the ERT models with different seeds with "sparse feature" were smaller than 0.02. Thus, the ERT model is robust in predicting the CO_2/CH_4 and CO_2/N_2 selectivity from the permeability of CO_2. This suggests that once the permeability of CO_2 for some polymer has been measured, researchers can quantitatively estimate the permeability of N_2 and CH_4 to gain primary insight on the CO_2/CH_4 and CO_2/N_2 selectivity of that polymer using the ERT model. Similarly, if only one gas pair (CO_2/CH_4 or CO_2/N_2) is tested, this method is of high predictive value for the other gas pair. This may save time for future work, because less experiments will be needed to screen the potential performance of new materials, but it may be particularly helpful also in the evaluation of existing materials outside the application field for which they were originally developed. For instance, many polymers were studied for carbon capture from flue gas, where CO_2/N_2 separation is relevant, but they may be equally interesting for the strongly emerging new application field of biogas upgrading, where CO_2/CH_4 separation is important.

6.5 PIMs Database construction

The previous section provides a method to anticipate the permeability of a gas if the permeability of at least one other gas is already known for that polymer. As discussed, this may be useful to extend the application field of a given polymer. However, for the development of completely new polymers, better predictive methods are needed, for instance models which are able to correlate the gas transport properties of a polymer with its chemical structure. Models that are able to 'synthesize' hypothetical new polymers can then predict their transport properties. Several

approaches have been reported in the literature, for different polymers. [116,134] Here the construction of a database is initiated with the relevant properties of all PIMs reported in the database of the Australasian Membrane Society [22] and a number of recently published and unpublished PIMs, anticipating the future construction of a ML model that will be able to predict promising new polymer structures with the desired gas transport properties. This PIMs Database includes structures, gas transport parameters, physical (BET surface area, Density, VdW volume, FFV Calculated, FFV measured and d-spacing), mechanical properties (Young's modulus, Tensile stress at break and tensile strain at break) and energetic parameters (activation energy of permeability (E_p), heat of sorption (H_s) and activation energy of diffusion (E_d)). It contains data of ~300 PIMs results of 67 unique PIMs structures for the transport parameters of 6 gases: He, H_2, O_2, N_2, CO_2 and CH_4. The research and data collection revealed that not every polymer in the database contains the experimentally reported values for every gas, Table 6.7.

Table 6.7 Number of missing permeability values in the PIMs Database of each gas.
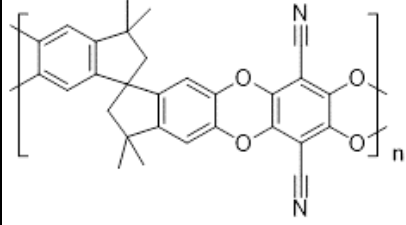
Gas	He	H_2	O_2	N_2	CO_2	CH_4
Number and percentage of missing values	148 (73%)	58 (29%)	7 (3%)	0 (0%)	9 (4%)	63 (3%)

Two excerpts from the database are shown in Table 6.8 and Table 6.9. The first two database columns *A* and *B* contain the category of the polymer and its name. Columns *C-J* report the chemical structures in a format that can be read by machine learning programs, namely the SMILE notation (A selection is shown in Table 6.8). These columns list the smaller fragments in which the polymers can be divided (usually their repeating units) and the complete structures. It is important to identify the fragments that are typical for the PIM structures, and their bonds with the neighbouring units; in this case they are represented by building blocks with 4 bonds, two at either side. The development of a new polymer with specific gas transport properties should be achieved by the combination of the different blocks and their linkages, and by the subsequent modelling of effect of the different groups on the gas transport. As anticipated, all the structures reported in the database are matched by their respective SMILE codes (Table 6.8).

For each structure, there are two SMILE codes: the first one with end-asterisks, and the second one without it. Asterisks are used in the SMILE code to indicate the binding site, unless specifically

mentioned otherwise, and this avoids that the structure is automatically completed with protons on the 'open' bond.

Table 6.8 Section of the PIMs database with smaller fragments (repeating units) and with the complete chemical structures of the polymers. For each structure, the SMILE structures are also reported.

B	D	G	J
Name	**Unit 1**	**Unit 2**	**Polymer Structure**
PIM-1	"[*]OC(C(C#N)=C(O[*])C(O[*])=C1C#N)=C1O[*] COC(C(C#N)=C(OC)C(OC)=C1C#N)=C1OC"	CC1(C)CC2(CC(C)(C)C3=C2C=C([*])C([*])=C3)C4=C1C=C([*])C([*])=C4 CC1(C)CC2(CC(C)(C)C3=C2C=C(C)C(C)=C3)C4=C1C=C(C)C(C)=C4	

As already described in Chapter 4, a complication of PIMs is that their transport parameters depend heavily on various experimental conditions such as the post-synthesis treatments with methanol or in temperature, the vacuum before each measurement, or the physical aging. Columns *K-O* report the different treatments in methanol, at elevated temperature and aging, when data are available (Table 6.9).
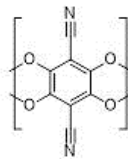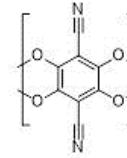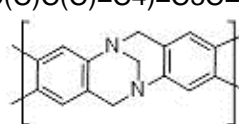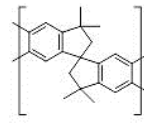
Table 6.9 PIMs database section with the different post-synthesis treatments and permeability data.

K	L	M	N	O	U	V	W	X	Y	Z
Treatment in MeOH	**Treatment in temp**	**T**	**time**	**AGE**	**Permeability [Barrer]**					
[No=0 ; Yes=1]	[No=0 ; Yes=1]	[K]	[h]	(days)	He	H_2	O_2	N_2	CO_2	CH_4
1	0			1	3826	1556	1579	506,1	9.65	913,5
1	0			2219	2825	1220	916,6	226,7	5.00	302,5
1	1	140	4	1	3675	1604	1309	397,6	7.44	621,9

If there has been no treatment, the corresponding cell value is 0 and otherwise it is 1. The columns *S* to *AQ* (transposed to rows in Table 6.10 for clarity), report the experimental parameters of the gas

permeation measurements and the values of permeability, diffusivity, solubility and permselectivity (ratio between different permeability). In the further columns of the file there are some physical, mechanical and energetic parameters. These comprise the BET (Brunauer, Emmett and Teller) specific surface area of the materials, the density, the free volume and the d-spacing (the distance between planes of atoms), The Young's modulus and the Tensile stress and strain at break. The final columns list the activation energy of permeability (E_p), the heat of sorption (H_s) and the activation energy of diffusion (E_d), Table 6.10. These parameters were added in order to have a complete and up-to-date easily accessible PIMs database for future studies.

Table 6.10 Example of the information inserted in the database (rows and columns transposed for more convenient plotting)

Col.	Property							
A		Category: polymer	PIMs	PIMs	PIMs	PIMs	PIMs	PIMs
B		Brief Description:	TBPIM33	TBPIM25	PIM-Btrip	PIM-Btrip	PIM-Btrip	PIM-Btrip
C		monomer unit 1						
D			[*]OC(C(C#N)=C(O[*])C(O[*])=C1C#N)=C1O[*] COC(C(C#N)=C(OC)C(OC)=C1C#N)=C1OC		[*]OC(C(C#N)=C(O[*])C(O[*])=C1C#N)=C1O[*] COC(C(C#N)=C(OC)C(OC)=C1C#N)=C1O			
E		copolymers (mon. Unit 1)	[*]C1=CC(N(CN2C3)CC4=C2C=C([*])C([*])=C4)=C3C=C1[*] CC1=CC(N(CN2C3)CC4=C2C=C(C)C(C)=C4)=C3C=C1C					
F		copolymers (mon. Unit 2)						
G		monomer unit 2	CC1(C)CC2(CC(C)(C)C3=C2C=C([*])C([*])=C3)C4=C1C=C([*])C([*])=C4 CC1(C)CC2(CC(C)(C)C3=C2C=C(C)C(C)=C3)C4=C1C=C(C)C(C)=C4		C[C@@]12C3=C(C=C([*])C([*])=C3)[C@@](C4=C2C=C([*])C([*])=C4)(C)C5=C1C=C(C=CC=C6)C6=C5 C[C@@]12C3=C(C=C(C)C(C)=C3)[C@@](C4=C2C=C(C)C(C)=C4)(C)C5=C1C=C(C=CC=C6)C6=C5			

113

H		**PI(Dan)**					
I		**PI(DAm)**					
J		**Structure Polymer**					
K		**Treatment in MeOH [No=0 ; Yes=1]**			1	1	1	1
L		**Temp. Treatment [No=0 ; Yes=1]**			0	0	0	0
M		**T [K]**						
N		**time [h]**						
O		**AGE (days)**			250	250	250	250
P		**Extended Description:**						
Q		**Reference Name:**	Wang, 2014	Wang, 2014	Fuoco 2018	Fuoco 2018	Fuoco 2018	Fuoco 2018
R		**Reference URL:**	10.1039/c3py01608k	10.1039/c3py01608k	10.1021/acsami.8b13634	10.1021/acsami.8b13634	10.1021/acsami.8b13634	10.1021/acsami.8b13634
S		**T perm [°C]**			25	35	45	55
T		**pressure perm [bar]**			1	1	1	1
U	**Permea**	**He**			3401.4	3392.3	3428.9	3458.5
V	**bility**	**H_2**			8929.3	8796.7	8730.2	8649.9
W	**[Barrer]**	**O_2**	864	917	2167.7	2368.5	2573.3	2710.2
X		**N_2**	240	262	401.4	505	638.2	774.7
Y		**CO_2**	4353	4441	10679.1	11292.2	11950.9	12188.3
Z		**CH_4**	353	726	410.8	536.1	724.9	945.6
AA	**Diffusivi**	**He**			8934.9	10519.1	10630	10933.9
AB	**ty [10^{-12}**	**H_2**			8041.4	7482.5	8062.9	8658.7
AC	**$m^2 s^{-1}$]**	**O_2**			254.6	331.1	429.2	534.9
AD		**N_2**	110	115	48.5	72.5	107.5	150.1
AE		**CO_2**	90	120	94.1	123.9	165.2	212.9
AF		**CH_4**			13.6	20.9	33.8	51
AG	**Solubilit**	**He**			0.29	0.24	0.24	0.24
AH	**y [cm^3**	**H_2**			0.83	0.88	0.81	0.75
AI	**$cm^{-3} bar^{-1}$]**	**O_2**			6.39	5.37	4.5	3.8
AJ		**N_2**	1.581395349	1.710427607	6.21	5.23	4.45	3.87
AK		**CO_2**	36.23	27.78	85.14	68.35	54.27	42.93
AL		**CH_4**			22.62	19.25	16.11	13.92
AM	**Permsel**	**O_2/N_2**	3.6	3.5	5.4	4.7	4.0	3.5
AN	**ectivity**	**H_2/N_2**			22.2	17.4	13.7	11.2
AO	**[-]**	**CO_2/N_2**	18.1	17.0	26.6	22.4	18.7	15.7
AP		**CO_2/CH_4**	12.3	6.1	26.0	21.1	16.5	12.9
AQ		**He/CH_4**			8.3	6.3	4.7	3.7
AR	**Physical**	**BET SA [$m^2 g^{-1}$]**	698	760	911	911	911	911
AS	**paramet**	**Density [$g\ cm^{-3}$]**	1.14	1.13				
AT	**ers**	**VdW volume [$cm^3 mol^{-1}$]**	232.7	236.1				
AU		**FFV Calculated [-]**	0.21	0.22				

AV		FFV measured						
AW		d-spacing						
AX	Mechanical	Young's modulus [Mpa]						
AY	properties	Stress at break [Mpa]						
AZ		Strain at break [%]						
BA	Ep [kCal mol^{-1}]	He			0.12	0.12	0.12	0.12
BB		H$_2$			-0.21	-0.21	-0.21	-0.21
BC		O$_2$			1.49	1.49	1.49	1.49
BD		N$_2$			4.34	4.34	4.34	4.34
BE		CO$_2$			0.9	0.9	0.9	0.9
BF		CH$_4$			5.55	5.55	5.55	5.55
BG	Ed [kCal mol^{-1}]	He			1.26	1.26	1.26	1.26
BH		H$_2$			0.57	0.57	0.57	0.57
BI		O$_2$			4.9	4.9	4.9	4.9
BJ		N$_2$			7.45	7.45	7.45	7.45
BK		CO$_2$			5.4	5.4	5.4	5.4
BL		CH$_4$			8.78	8.78	8.78	8.78
BM	Hs [kCal mol^{-1}]	He			-1.14	-1.14	-1.14	-1.14
BN		H$_2$			-0.77	-0.77	-0.77	-0.77
BO		O$_2$			-3.41	-3.41	-3.41	-3.41
BP		N$_2$			-3.11	-3.11	-3.11	-3.11
BQ		CO$_2$			-4.5	-4.5	-4.5	-4.5
BZ		CH$_4$			-3.24	-3.24	-3.24	-3.24

6.6 Conclusions

Machine learning proved extremely useful in the prediction of gas permeability of polymers from the literature, for which only a limited number of gases had been tested. The missing values for the permeability of He, H$_2$, O$_2$, N$_2$, CH$_4$ and CO$_2$ in the online *Polymer Gas Separation Membrane Database* of the Membrane Society of Australasia were imputed using the MICE algorithm combined with Bayesian Linear Regression and Extremely Randomized Trees models. Validation of the imputation model against unseen data suggests that the gas permeability can be modelled with reasonable accuracy. The models result using "sparse features" suggest that permeability of He, H$_2$, O$_2$, N$_2$ and CH$_4$ can be quantitatively estimated using the gas permeability of O$_2$ and/or CO$_2$. Specifically, the ERT model is robust in predicting the CO$_2$/CH$_4$ and CO$_2$/N$_2$ selectivity from the permeability of CO$_2$. It is suggested that for cases with "dense features", where the permeability data of multiple gases is already measured, the BLR model can provide accurate imputation results to the remaining gas permeability. For cases with "sparse features", on the other hand, the ERT

model is recommended for making quantitative predictions to the permeability of untested gases given that the CO_2 permeability has been measured.

This fast and versatile approach enables a rapid screening of the gas permeability at the initial stage of experimental measurements. This is of considerable interest especially in the case of newly synthesized polymers, such as PIMs discussed in previous chapters, especially when the measurements are long and costly. The imputed database can be used as the training set for the prediction of the full range of gas permeability from a single rapid measurement using the ML models. Such models rely purely on the experimental measurement data of the gas permeability of one or more gases, they are applicable against different experimental conditions (such as aging and post-synthesis treatments discussed in chapter 0 and do not require any knowledge about the polymer structures.

Chapter 7

Concluding remarks

The main purpose of this thesis work was study different polymeric membranes type for gas separation processes in order to understand their advantages and applicability as well as their limits through a detailed analysis of their structure-properties relationships. The main idea was to realise membranes by combining good transport and separation properties with a good mechanical stability.

7.1 Key Outcomes

One of the important results achieved in this thesis was the demonstration that AFM force spectroscopy is an excellent alternative to tensile tests for the analysis of the Young's modulus of membranes, even in the case of complex systems such as MMMs. In the proposed Pebax®/IL membranes, presented in chapter 3, the IL causes an exponential decrease of Young's modulus with increasing percentage of IL. The permeability and diffusion coefficients increase with increasing IL content, as a consequence of the lower crystallinity and the increased mobility of the polymer chains in the blend, in which the crystal domains serve as physical cross-links of the microphase-separated thermoplastic elastomer. The complex multiphase system of MMMs, from a mechanical point of view, can be studied with a tip having dimensions comparable with the polymer domains. In this study, it was demonstrated that the nanometric tip is able to probe the local properties of the individual polyether and polyamide phases. Instead, a larger micrometric tip is able to probe the average bulk properties of the polymer/IL blend. The good match found between the mechanical properties measured by traditional tensile tests and by AFM force spectroscopy on the micro scale, ensures the reliability of the force spectroscopy method for the characterization small scale membrane samples.

The AFM force spectroscopy was used to measure the mechanical properties of membranes of a series of different PIMs (chapter 4), and this study revealed a strong correlation between the stiffness of the polymer films and their transport parameters. It was found that the decrease of the diffusion coefficients during aging is associated with a simultaneous increase in the Young's modulus, suggesting that the size-selectivity is strongly correlated with the stiffness of the material. Structurally similar samples with different history follow a nearly universal trend, independent of the specific sample, confirming the importance of the sample rigidity in determining the transport

properties. Thermal treatment accelerates the physical aging of the samples in terms of transport parameters, causing a distinct drop in permeability and diffusivity, while the further aging as a function of time slightly slows down. Also in terms of mechanical properties, after an initial increase in Young's modulus upon thermal conditioning of the sample, there is a slower further increase with time. These results indicate that the high temperature stabilizes the sample properties, which could be used to reduce the effect of undesired aging as a function of time. The high elastic modulus in the studied fluorinated PIMs is a result of the rigid ladder-like polymer backbone in combination with the halogen bonds occurring within the polymer matrix. The gas permeability and diffusivity systematically decrease with Young's modulus in PIMs, in a somehow universal trend, regardless of sample history. Some sample-to-sample differences indicate that the correlation is not perfect, and that other independent factors play a role, such as differences in pore size distribution and fractional free volume.

The additional permeation analysis as a function of temperature on PIM-TMN-Trip and PIM-BTrip revealed that the enhanced gas-separation performances for O2/N2, H2/N2, and He/N2 are driven by strong energetic selectivity, with extremely high values demonstrated for PIM-BTrip. Hence, when the penetrant gas diffuses though a well-packed region of the polymer, the opening of motion-enabled zones in PIM-TMN-Trip and PIM-BTrip requires a displacement of the very rigid polymer chains, which leads to high energetic selectivity as a function of the penetrant dimensions. The application of membranes derived from triptycene-based PIMs at low temperatures may help to achieve commercially interesting separation factors for several gas pairs. This is especially valid for the gas pairs CO2/N2 and CO2/CH4 where the enhanced selectivity is accompanied by the enhanced permeability of CO2 due to its strong increase in solubility.

Newly developed Matrimid®5218/AO-PIM-1 blend membranes were designed to combine the synergistic properties of a PIM and a glassy polymer into a new composite with targeted performance and to overcome the limits of the individual components (chapter 5). Indeed, the diffusion coefficients increased with the PIM content in the blend, and in all cases the blend membranes exhibited a higher permselectivity then the pure AO-PIM-1. The best-performing membrane is the one with the smallest amount of PIM (Matrimid®5218_AO-PIM-1_80_20). In this membrane the permselectivity remains the same as in Matrimid®5218 and the permeability increases. Therefore, the AO-PIM-1 offers the possibility to increase the permeability of

Matrimid®5218 maintaining an attractive selectivity. On the other hand, the increase in permeability is much smaller than that observed in blends of other PIMs with Matrimid®, like PIM-1 [91] and PIM-EA(H2)-TB [94]. This this may be due to specific interactions of the functional groups in Matrimid® and the polar AO group in our PIM, and a relatively strong decrease in the diffusion coefficient, apparently due to a significant loss of the intrinsic microporosity.

A computational approach enables the prediction of missing permeability values of the online Polymer Gas Separation Membrane Database starting with an existing permeability data set for other polymers (chapter 6). With this fast and versatile machine learning approach, one can gain insight into the gas permeability by a rapid screening at the initial stage of experimental measurements. This is of considerable interest especially in the case of newly synthesized polymers, such as PIMs, or in the case of slow-diffusing gases, for which experimental measurements are long and costly. The imputed database can be used as the training set for the prediction of the full range of gas permeability from a single rapid measurement using the ML models. Such models rely purely on the experimental measurement data of the gas permeability of one or more gases, they are applicable against different experimental conditions and do not require any knowledge about the polymer structures.

7.2 Outlook

In conclusion, it can be said that the force spectroscopy can be used as an alternative for tensile tests for analysis of Young's modulus in polymers samples. This technique may offer also interesting perspectives for the analysis of the mechanical properties of samples that cannot be measured otherwise, such as thin film composite membranes, where the presence of a nonwoven fibre support makes the traditional tensile tests unsuitable. The study opens for further investigation and validation on different materials to explore the full potential and the limits of the method.

The permeability and mechanical studies on PIMs confirm how promising PIMs are for gas separation applications. The strong correlation between the polymer stiffness and the size-selectivity suggests designing even more size-selective PIMs by aiming at more rigid structures than those already available. The thermal treatment of PIMs may be a successful approach for mitigating

aging that causes undesired changes of the transport properties with time and is one of the main reasons why PIMs have not found practical application in spite of their exceptional performance.

Polymer blends offer the possibility to tailor the transport properties of membranes between the values of the individual components. The design of PIM/polymer blends should aim at polymer pairs with a good compatibility, for instance by weak polar interactions or acid-base interactions, and may produce membranes of which the permeability can be varied over a wide range.

Finally, the application of machine learning models that can impute missing permeability data for existing polymers is extremely helpful, but for an efficient development of new membranes it is desirable to design a Machine learning model, which correlates structural parameters of the polymer with the permeability in order to achieve real predictability and a tool to develop novel polymers with enhanced properties.

Definitely, membrane technology offers a potentially successful alternative to the traditional techniques of gas separation from various points of view. The knowledge promoted in the present work indicates the direction for further investigation, including the validation of the performance under real operating conditions.

Bibliography

[1]   D.S. Sholl, R.P. Lively, Seven chemical separations to change the world, Nature. 532 (2016) 435–437. https://doi.org/10.1038/532435a.

[2]   R.W. Baker, Z.P. Smith, B.D. Freeman, W.S. Chi, T.C. Merkel, M. Galizia, 50th Anniversary Perspective : Polymers and Mixed Matrix Membranes for Gas and Vapor Separation: A Review and Prospective Opportunities , Macromolecules. 50 (2017) 7809–7843. https://doi.org/10.1021/acs.macromol.7b01718.

[3]   E. Esposito, L. Dellamuzia, U. Moretti, A. Fuoco, L. Giorno, J.C. Jansen, Simultaneous production of biomethane and food grade CO2 from biogas: An industrial case study, Energy Environ. Sci. 12 (2019) 281–289. https://doi.org/10.1039/c8ee02897d.

[4]   P. Izák, Z. Sedláková, S. Curcio, F. Tasselli, B. de Cindio, G. Clarizia, J.C. Jansen, E. Esposito, P. Bernardo, Pebax®/PAN hollow fiber membranes for CO2/CH4 separation, Chem. Eng. Process. - Process Intensif. 94 (2015) 53–61. https://doi.org/10.1016/j.cep.2015.03.016.

[5]   M. Longo, M.P. De Santo, E. Esposito, A. Fuoco, M. Monteleone, L. Giorno, J.C. Jansen, Force spectroscopy determination of Young's modulus in mixed matrix membranes, Polymer (Guildf). 156 (2018) 22–29. https://doi.org/10.1016/J.POLYMER.2018.09.043.

[6]   R.D. Noble, Perspectives on mixed matrix membranes, J. Memb. Sci. 378 (2011) 393–397. https://doi.org/10.1016/j.memsci.2011.05.031.

[7]   M. Vinoba, M. Bhagiyalakshmi, Y. Alqaheem, A.A. Alomair, A. Pérez, M.S. Rana, Recent progress of fillers in mixed matrix membranes for CO2 separation: A review, Sep. Purif. Technol. 188 (2017) 431–450. https://doi.org/10.1016/j.seppur.2017.07.051.

[8]   S. Meshkat, S. Kaliaguine, D. Rodrigue, Mixed matrix membranes based on amine and non-amine MIL-53(Al) in Pebax® MH-1657 for CO2separation, Sep. Purif. Technol. 200 (2018) 177–190. https://doi.org/10.1016/j.seppur.2018.02.038.

[9]   A. Bandyopadhyay, Amine versus ammonia absorption of CO2 as a measure of reducing ghg emission: A critical analysis, Carbon Capture Storage CO2 Manag. Technol. (2014) 1–54. https://doi.org/10.1201/b16845.

[10]   Z. Dai, R.D. Noble, D.L. Gin, X. Zhang, L. Deng, Combination of ionic liquids with membrane technology: A new approach for CO2 separation, J. Memb. Sci. 497 (2016) 1–20. https://doi.org/10.1016/j.memsci.2015.08.060.

[11]   P. Bernardo, J.C. Jansen, F. Bazzarelli, F. Tasselli, A. Fuoco, K. Friess, P. Izák, V. Jarmarová, M. Kačírková, G. Clarizia, Gas transport properties of Pebax®/room temperature ionic liquid gel membranes, Sep. Purif. Technol. 97 (2012) 73–82. https://doi.org/10.1016/J.SEPPUR.2012.02.041.

[12]   M. Kohoutová, A. Sikora, Š. Hovorka, A. Randová, J. Schauer, M. Tišma, K. Setničková, R. Petričkovič, S. Guernik, N. Greenspoon, P. Izák, Influence of ionic liquid content on properties of dense polymer membranes, Eur. Polym. J. 45 (2009) 813–819. https://doi.org/10.1016/j.eurpolymj.2008.11.043.

[13]   R.W. Baker, B.T. Low, Gas separation membrane materials: A perspective, Macromolecules. 47 (2014) 6999–7013. https://doi.org/10.1021/ma501488s.

[14]   B.D. Freeman, Basis of permeability/selectivity tradeoff relations in polymeric gas separation membranes, Macromolecules. 32 (1999) 375–380. https://doi.org/10.1021/ma9814548.

[15]   P.M. Budd, B.S. Ghanem, S. Makhseed, N.B. McKeown, K.J. Msayib, C.E. Tattershall, Polymers of intrinsic microporosity (PIMs): robust, solution-processable, organic nanoporous materials, Chem. Commun. 4 (2004) 230–231. https://doi.org/10.1039/b311764b.

[16]   C. Ma, J.J. Urban, Polymers of Intrinsic Microporosity (PIMs) Gas Separation Membranes: A mini Review, Proc. Nat. Res. Soc. 2 (2018). https://doi.org/10.11605/j.pnrs.201802002.

[17]   Z.P. Smith, R.R. Tiwari, M.E. Dose, K.L. Gleason, T.M. Murphy, D.F. Sanders, G. Gunawan, L.M. Robeson, D.R. Paul, B.D. Freeman, Influence of Diffusivity and Sorption on Helium and Hydrogen Separations in Hydrocarbon, Silicon, and Fluorocarbon-Based Polymers, Macromolecules. 47 (2014) 3170–3184. https://doi.org/10.1021/ma402521h.

[18]   J. Duan, M. Higuchi, R. Krishna, T. Kiyonaga, Y. Tsutsumi, Y. Sato, Y. Kubota, M. Takata, S. Kitagawa, High CO2/N2/O2/CO separation in a chemically robust porous coordination polymer with low binding energy, Chem. Sci. 5 (2014) 660–666. https://doi.org/10.1039/C3SC52177J.

[19]   A. Fuoco, B. Comesaña-Gándara, M. Longo, E. Esposito, M. Monteleone, I. Rose, C.G. Bezzu, M. Carta, N.B. McKeown, J.C. Jansen, Temperature Dependence of Gas Permeation and Diffusion in Triptycene-Based Ultrapermeable Polymers of Intrinsic Microporosity, ACS Appl. Mater. Interfaces. 10 (2018) 36475–36482. https://doi.org/10.1021/acsami.8b13634.

[20]   C.H. Lau, P.T. Nguyen, M.R. Hill, A.W. Thornton, K. Konstas, C.M. Doherty, R.J. Mulder, L. Bourgeois, A.C.Y. Liu, D.J. Sprouster, J.P. Sullivan, T.J. Bastow, A.J. Hill, D.L. Gin, R.D. Noble, Ending aging in super glassy polymer membranes, Angew. Chemie - Int. Ed. 53 (2014) 5322–5326. https://doi.org/10.1002/anie.201402234.

[21]   M. Longo, M.P. De Santo, E. Esposito, A. Fuoco, M. Monteleone, L. Giorno, B. Comesaña-Gándara, J. Chen, C.G. Bezzu, M. Carta, I. Rose, N.B. McKeown, J.C. Jansen, Correlating Gas Permeability and Young's Modulus during the Physical Aging of Polymers of Intrinsic Microporosity Using Atomic Force Microscopy, Ind. Eng. Chem. Res. 59 (2020) 5381–5391. https://doi.org/10.1021/acs.iecr.9b04881.

[22]   L.M. Thornton, A.W., Freeman, B.D., and Robeson, Polymer Gas Separation Membrane Database, (2012). https://membrane-australasia.org/msa-activities/polymer-gas-separation-membrane-database/.

[23]   Z.-X.X. Low, P.M. Budd, N.B. McKeown, D.A. Patterson, Gas Permeation Properties, Physical Aging,

and Its Mitigation in High Free Volume Glassy Polymers, American Chemical Society, 2018. https://doi.org/10.1021/acs.chemrev.7b00629.

[24] K. Friess, P. Izák, M. Kárászová, M. Pasichnyk, M. Lanč, D. Nikolaeva, P. Luis, J.C. Jansen, A review on ionic liquid gas separation membranes, Membranes (Basel). 11 (2021). https://doi.org/10.3390/membranes11020097.

[25] J. Schauer, G. Clarizia, K. Friess, P. Izák, J.C. Jansen, High Ionic Liquid Content Polymeric Gel Membranes: Preparation and Performance, Macromolecules. 44 (2010) 39–45. https://doi.org/10.1021/ma102438k.

[26] B. Cappella, G. Dietler, Force-distance curves by atomic force microscopy, Surf. Sci. Rep. 34 (1999) 1–3. https://doi.org/10.1016/S0167-5729(99)00003-5.

[27] H.J. Butt, B. Cappella, M. Kappl, Force measurements with the atomic force microscope: Technique, interpretation and applications, Surf. Sci. Rep. 59 (2005) 1–152. https://doi.org/10.1016/j.surfrep.2005.08.003.

[28] J.P. Sheth, J. Xu, G.L. Wilkes, Solid state structure-property behavior of semicrystalline poly(ether-block-amide) PEBAX® thermoplastic elastomers, Polymer (Guildf). 44 (2002) 743–756. https://doi.org/10.1016/S0032-3861(02)00798-X.

[29] B.B. Sauer, R.S. McLean, R.R. Thomas, Nanometer resolution of crystalline morphology using scanning probe microscopy, Polym. Int. 49 (2000) 449–452. https://doi.org/10.1002/(SICI)1097-0126(200005)49:5<449::AID-PI351>3.0.CO;2-F.

[30] R. Knoll, K. Magerle, G. Krausch, Tapping Mode atomic force microscopy on polymers: Where is the true sample surface?, Macromolecules. 34 (2001) 4159–4165. https://doi.org/10.1021/ma001311x.

[31] G. Moeller, AFM Nanoindentation of viscoelastic materials with large end-Radius probes, J. Polym. Sci. Part B Polym. Phys. 47 (2009) 1573–1587. https://doi.org/10.1002/polb.21758.

[32] D. Wang, T.P. Russell, Advances in Atomic Force Microscopy for Probing Polymer Structure and Properties, Macromolecules. 51 (2018) 3–24. https://doi.org/10.1021/acs.macromol.7b01459.

[33] L.M. Robeson, Correlation of separation factor versus permeability for polymeric membranes, J. Memb. Sci. 62 (1991) 165–185. https://doi.org/10.1016/0376-7388(91)80060-J.

[34] L.M. Robeson, The upper bound revisited, J. Memb. Sci. 320 (2008) 390–400. https://doi.org/10.1016/j.memsci.2008.04.030.

[35] R. Swaidan, B. Ghanem, I. Pinnau, Fine-Tuned Intrinsically Ultramicroporous Polymers Redefine the Permeability/Selectivity Upper Bounds of Membrane-Based Air and Hydrogen Separations, ACS Macro Lett. 4 (2015) 947–951. https://doi.org/10.1021/acsmacrolett.5b00512.

[36] B. Comesaña-Gándara, J. Chen, C.G. Bezzu, M. Carta, I. Rose, M.-C. Ferrari, E. Esposito, A. Fuoco, J.C. Jansen, N.B. McKeown, Redefining the Robeson upper bounds for CO_2/CH_4 and CO_2/N_2

separations using a series of ultrapermeable benzotriptycene-based polymers of intrinsic microporosity, Energy Environ. Sci. 12 (2019) 2733–2740. https://doi.org/10.1039/C9EE01384A.

[37] S. Bandehali, A. Ebadi Amooghin, H. Sanaeepur, R. Ahmadi, A. Fuoco, J.C. Jansen, S. Shirazian, Polymers of intrinsic microporosity and thermally rearranged polymer membranes for highly efficient gas separation, Sep. Purif. Technol. 278 (n.d.) 119513.

[38] S. Wu, Y. Kondo, M. Kakimoto, B. Yang, H. Yamada, I. Kuwajima, G. Lambard, K. Hongo, Y. Xu, J. Shiomi, C. Schick, J. Morikawa, R. Yoshida, Machine-learning-assisted discovery of polymers with high thermal conductivity using a molecular design algorithm, Npj Comput. Mater. 5 (2019) 66. https://doi.org/10.1038/s41524-019-0203-2.

[39] L.M. Robeson, C.D. Smith, M. Langsam, A group contribution approach to predict permeability and permselectivity of aromatic polymers, J. Memb. Sci. 132 (1997) 33–54. https://doi.org/10.1016/S0376-7388(97)00031-8.

[40] J.Y.Y. Park, D.R.R. Paul, Correlation and prediction of gas permeability in glassy polymer membrane materials via a modified free volume based group contribution method, J. Memb. Sci. 125 (1997) 23–39. https://doi.org/10.1016/S0376-7388(96)00061-0.

[41] H. Hasnaoui, M. Krea, D. Roizard, Neural networks for the prediction of polymer permeability to gases, J. Memb. Sci. 541 (2017) 541–549. https://doi.org/10.1016/J.MEMSCI.2017.07.031.

[42] A. Fuoco, C. Rizzuto, E. Tocci, M. Monteleone, E. Esposito, P.M. Budd, M. Carta, B. Comesaña-Gándara, N.B. McKeown, J.C. Jansen, The origin of size-selective gas transport through polymers of intrinsic microporosity, J. Mater. Chem. A. 7 (2019) 20121–20126. https://doi.org/10.1039/C9TA07159H.

[43] J.G. Wijmans, R.W. Baker, The solution-diffusion model: a review, J. Memb. Sci. 107 (1995) 1–21. https://doi.org/10.1016/0376-7388(95)00102-I.

[44] J.G.H. Wijmans, R.W. Baker, The Solution-Diffusion Model: A Unified Approach to Membrane Permeation, 2006. https://doi.org/10.1002/047002903X.ch5.

[45] Y. Yampolskii, I. Pinnau, B.D. Freeman, Materials Science of Membranes for Gas and Vapor Separation, 2006. https://doi.org/10.1002/047002903X.

[46] M.M.R. Williams, The mathematics of diffusion, 2nd ed., Clarendon Press, Oxford, 1977. https://doi.org/10.1016/0306-4549(77)90072-X.

[47] A. Singh-Ghosal, W.J. Koros, Energetic and entropic contributions to mobility selectivity in glassy polymers for gas separation membranes, Ind. Eng. Chem. Res. 38 (1999) 3647–3654. https://doi.org/10.1021/ie990070i.

[48] V. Teplyakov, P. Meares, Correlation aspects of the selective gas permeabilities of polymeric materials and membranes, Gas Sep. Purif. 4 (1990) 66–74. https://doi.org/10.1016/0950-4214(90)80030-O.

[49] A. Singh, W.J. Koros, Significance of Entropic Selectivity for Advanced Gas Separation Membranes, Ind. Eng. Chem. Res. 35 (1996) 1231–1234. https://doi.org/10.1021/ie950559l.

[50] C.M. Zimmerman, W.J. Koros, Entropic selectivity analysis of a series of polypyrrolones for gas separation membranes, Macromolecules. 32 (1999) 3341–3346. https://doi.org/10.1021/ma981411r.

[51] W.J. Koros, C. Zhang, Materials for next-generation molecularly selective synthetic membranes, Nat. Mater. 16 (2017) 289–297. https://doi.org/10.1038/nmat4805.

[52] J. Israelachvili, Intermolecular and Surface Forces, 2011. https://doi.org/10.1016/C2009-0-21560-1.

[53] H.C. Hamaker, The London-van der Waals attraction between spherical particles, Physica. 4 (1937). https://doi.org/10.1016/S0031-8914(37)80203-7.

[54] B. Derjaguin, Range of action of surface forces [12], Nature. 138 (1936). https://doi.org/10.1038/138330c0.

[55] S.N. Magonov, V. Elings, M.H. Whangbo, Phase imaging and stiffness in tapping-mode atomic force microscopy, Surf. Sci. 375 (1997) L385–L391. https://doi.org/10.1016/S0039-6028(96)01591-9.

[56] H. Hertz, Ueber die Berührung fester elastischer Körper., J. Für Die Reine Und Angew. Math. (Crelle's Journal). 1882 (2009) 156–171. https://doi.org/10.1515/crll.1882.92.156.

[57] I.N. Sneddon, The relation between load and penetration in the axisymmetric boussinesq problem for a punch of arbitrary profile, Int. J. Eng. Sci. 3 (1965) 47–57. https://doi.org/10.1016/0020-7225(65)90019-4.

[58] G.N. Greaves, A.L. Greer, R.S. Lakes, T. Rouxel, Poisson's ratio and modern materials, Nat. Mater. 10 (2011) 823–837. https://doi.org/10.1038/nmat3134.

[59] S. Lian, C. Song, Q. Liu, E. Duan, H. Ren, Y. Kitamura, Recent advances in ionic liquids-based hybrid processes for CO2 capture and utilization, J. Environ. Sci. (China). 99 (2021). https://doi.org/10.1016/j.jes.2020.06.034.

[60] L.A. Blanchard, D. Hancu, E.J. Beckman, J.F. Brennecke, Green processing using ionic liquids and CO2, Nature. 399 (1999) 28–29. https://doi.org/10.1038/19887.

[61] H. Lin, B.D. Freeman, Materials selection guidelines for membranes that remove CO2 from gas mixtures, J. Mol. Struct. 739 (2005) 57–74. https://doi.org/10.1016/j.molstruc.2004.07.045.

[62] C. Cadena, J.L. Anthony, J.K. Shah, T.I. Morrow, J.F. Brennecke, E.J. Maginn, Why is CO2 so Soluble in Imidazolium-Based Ionic Liquids?, J. Am. Chem. Soc. 126 (2004) 5300–5308. https://doi.org/10.1021/ja039615x.

[63] M.J. Muldoon, S.N.V.K. Aki, J.L. Anderson, J.K. Dixon, J.F. Brennecke, Improving carbon dioxide solubility in ionic liquids, J. Phys. Chem. B. 111 (2007) 9001–9009. https://doi.org/10.1021/jp071897q.

[64] M. Lombardo, G. Lombardo, G. Carbone, M.P. de Santo, R. Barberi, S. Serrao, Biomechanics of the anterior human corneal tissue investigated with atomic force microscopy, Investig. Ophthalmol. Vis. Sci. 53 (2012) 1050–1057. https://doi.org/10.1167/iovs.11-8720.

[65] C. Labate, M. Lombardo, M.P. De Santo, J. Dias, N.M. Ziebarth, G. Lombardo, Multiscale investigation of the depth-dependent mechanical anisotropy of the human corneal stroma, Investig. Ophthalmol. Vis. Sci. 56 (2015) 4053–4060. https://doi.org/10.1167/iovs.15-16875.

[66] P.M. Budd, E.S. Elabas, B.S. Ghanem, S. Makhseed, N.B. McKeown, K.J. Msayib, C.E. Tattershall, D. Wang, Solution-Processed, Organophilic Membrane Derived from a Polymer of Intrinsic Microporosity, Adv. Mater. 16 (2004) 456–459. https://doi.org/10.1002/adma.200306053.

[67] N.B. McKeown, P.M. Budd, Exploitation of intrinsic microporosity in polymer-based materials, Macromolecules. 43 (2010). https://doi.org/10.1021/ma1006396.

[68] Y. Huang, D.R. Paul, Physical aging of thin glassy polymer films monitored by gas permeability, Polymer (Guildf). 45 (2004) 8377–8393. https://doi.org/10.1016/j.polymer.2004.10.019.

[69] K. Polak-Kraśna, C. Fuhrhop, S. Rochat, A.D.D. Burrows, A. Georgiadis, C.R.R. Bowen, T.J.J. Mays, AFM imaging and nanoindentation of polymer of intrinsic microporosity PIM-1, Int. J. Hydrogen Energy. 42 (2017) 23915–23919. https://doi.org/10.1016/j.ijhydene.2017.04.081.

[70] A. Fuoco, B. Satilmis, T. Uyar, M. Monteleone, E. Esposito, C. Muzzi, E. Tocci, M. Longo, M.P. De Santo, M. Lanč, K. Friess, O. Vopička, P. Izák, J.C. Jansen, Comparison of pure and mixed gas permeation of the highly fluorinated polymer of intrinsic microporosity PIM-2 under dry and humid conditions: Experiment and modelling, J. Memb. Sci. 594 (2020) 117460. https://doi.org/10.1016/j.memsci.2019.117460.

[71] I. Rose, C.G. Bezzu, M. Carta, B. Comesaña-Gándara, E. Lasseuguette, M.C. Ferrari, P. Bernardo, G. Clarizia, A. Fuoco, J.C. Jansen, K.E. Hart, T.P. Liyana-Arachchi, C.M. Colina, N.B. McKeown, Polymer ultrapermeability from the inefficient packing of 2D chains, Nat. Mater. 16 (2017) 932–937. https://doi.org/10.1038/nmat4939.

[72] N.M. C.G. Bezzu, A. Fuoco, E. Esposito, M. Longo, M. Monteleone, J.C. Jansen, G. Nichol, Ultrapermeable polymers of intrinsic microporosity derived from a spirocyclic monomer containing fused triptycenes, Adv. Mater. (2021).

[73] S. Harms, K. Rätzke, F. Faupel, N. Chaukura, P.M. Budd, W. Egger, L. Ravelli, Aging and free volume in a polymer of intrinsic microporosity (PIM-1), J. Adhes. 88 (2012) 608–619. https://doi.org/10.1080/00218464.2012.682902.

[74] A.J. Hill, S.J. Pas, T.J. Bastow, M.I.I. Burgar, K. Nagai, L.G. Toy, B.D. Freeman, Influence of methanol conditioning and physical aging on carbon spin-lattice relaxation times of poly(1-trimethylsilyl-1-propyne), J. Memb. Sci. 243 (2004) 37–44. https://doi.org/10.1016/j.memsci.2004.06.007.

[75] J.G. Seong, Y. Zhuang, S. Kim, Y.S. Do, W.H. Lee, M.D. Guiver, Y.M. Lee, Effect of methanol treatment on gas sorption and transport behavior of intrinsically microporous polyimide membranes incorporating Tröger's base, J. Memb. Sci. 480 (2015) 104–114. https://doi.org/10.1016/J.MEMSCI.2015.01.022.

[76]   R. Swaidan, B. Ghanem, E. Litwiller, I. Pinnau, Physical Aging, Plasticization and Their Effects on Gas Permeation in "rigid" Polymers of Intrinsic Microporosity, Macromolecules. 48 (2015) 6553–6561. https://doi.org/10.1021/acs.macromol.5b01581.

[77]   S. Rochat, K. Polak-Kraśna, M. Tian, T.J. Mays, C.R. Bowen, A.D. Burrows, Assessment of the long-term stability of the polymer of intrinsic microporosity PIM-1 for hydrogen storage applications, Int. J. Hydrogen Energy. 44 (2019) 332–337. https://doi.org/10.1016/J.IJHYDENE.2018.02.175.

[78]   M. Alberto, R. Bhavsar, J.M. Luque-Alled, A. Vijayaraghavan, P.M. Budd, P. Gorgojo, Impeded physical aging in PIM-1 membranes containing graphene-like fillers, J. Memb. Sci. 563 (2018) 513–520. https://doi.org/10.1016/J.MEMSCI.2018.06.026.

[79]   K. Polak-Kraśna, R. Dawson, L.T. Holyfield, C.R. Bowen, A.D. Burrows, T.J. Mays, Mechanical characterisation of polymer of intrinsic microporosity PIM-1 for hydrogen storage applications, J. Mater. Sci. 52 (2017) 3862–3875. https://doi.org/10.1007/s10853-016-0647-4.

[80]   Q. Song, S. Cao, R.H. Pritchard, B. Ghalei, S.A. Al-Muhtaseb, E.M. Terentjev, A.K. Cheetham, E. Sivaniah, Controlled thermal oxidative crosslinking of polymers of intrinsic microporosity towards tunable molecular sieve membranes, Nat. Commun. 5 (2014) 4813. https://doi.org/10.1038/ncomms5813.

[81]   H.B. Park, C.H. Jung, Y.M. Lee, A.J. Hill, S.J. Pas, S.T. Mudie, E. Van Wagner, B.D. Freeman, D.J. Cookson, Polymers with cavities tuned for fast selective transport of small molecules and ions, Science (80-.). 318 (2007) 254–258. https://doi.org/10.1126/science.1146744.

[82]   P. Bernardo, F. Bazzarelli, F. Tasselli, G. Clarizia, C.R. Mason, L. Maynard-Atem, P.M. Budd, M. Lanč, K. Pilnáček, O. Vopička, K. Friess, D. Fritsch, Y.P. Yampolskii, V. Shantarovich, J.C. Jansen, Effect of physical aging on the gas transport and sorption in PIM-1 membranes, Polymer (Guildf). 113 (2017) 283–294. https://doi.org/10.1016/J.POLYMER.2016.10.040.

[83]   K. Pilnáček, O. Vopička, M. Lanč, M. Dendisová, M. Zgažar, P.M. Budd, M. Carta, R. Malpass-Evans, N.B. McKeown, K. Friess, Aging of polymers of intrinsic microporosity tracked by methanol vapour permeation, J. Memb. Sci. 520 (2016) 895–906. https://doi.org/10.1016/j.memsci.2016.08.054.

[84]   B.W. Rowe, B.D. Freeman, D.R. Paul, Physical aging of ultrathin glassy polymer films tracked by gas permeability, Polymer (Guildf). 50 (2009) 5565–5575. https://www.sciencedirect.com/science/article/pii/S0032386109007940 (accessed October 8, 2019).

[85]   Y. Huang, D.R. Paul, Effect of film thickness on the gas-permeation characteristics of glassy polymer membranes, Ind. Eng. Chem. Res. 46 (2007) 2342–2347. https://doi.org/10.1021/ie0610804.

[86]   B.W. Rowe, S.J. Pas, A.J. Hill, R. Suzuki, B.D. Freeman, D.R. Paul, A variable energy positron annihilation lifetime spectroscopy study of physical aging in thin glassy polymer films, Polymer (Guildf). 50 (2009) 6149–6156. https://doi.org/10.1016/j.polymer.2009.10.045.

[87]   T. Emmler, K. Heinrich, D. Fritsch, P.M. Budd, N. Chaukura, D. Ehlers, K. Rätzke, F. Faupel, Free volume investigation of polymers of intrinsic microporosity (PIMs): PIM-1 and PIM1 copolymers incorporating ethanoanthracene units, Macromolecules. 43 (2010) 6075–6084. https://doi.org/10.1021/ma1008786.

[88]   T. Koschine, K. Rätzke, F. Faupel, M.M. Khan, T. Emmler, V. Filiz, V. Abetz, L. Ravelli, W. Egger, Correlation of gas permeation and free volume in new and used high free volume thin film composite membranes, J. Polym. Sci. Part B Polym. Phys. 53 (2015) 213–217. https://doi.org/10.1002/polb.23616.

[89]   X. Ma, I. Pinnau, Effect of Film Thickness and Physical Aging on "Intrinsic" Gas Permeation Properties of Microporous Ethanoanthracene-Based Polyimides, Macromolecules. 51 (2018) 1069–1076. https://doi.org/10.1021/acs.macromol.7b02556.

[90]   R.M. BARRER, Nature of the Diffusion Process in Rubber, Nature. 140 (1937) 106.

[91]   P. Li, T.S. Chung, D.R. Paul, Temperature dependence of gas sorption and permeation in PIM-1, J. Memb. Sci. 450 (2014) 380–388. https://doi.org/10.1016/j.memsci.2013.09.030.

[92]   T. Masuda, Y. Iguchi, B.Z. Tang, T. Higashimura, Diffusion and solution of gases in substituted polyacetylene membranes, Polymer (Guildf). 29 (1988) 2041–2049. https://doi.org/10.1016/0032-3861(88)90178-4.

[93]   M. Calle, Y.M. Lee, Thermally Rearranged (TR) Poly(ether–benzoxazole) Membranes for Gas Separation, Macromolecules. 44 (2011) 1156–1165. https://doi.org/10.1021/ma102878z.

[94]   H.B. Park, S.H. Han, C.H. Jung, Y.M. Lee, A.J. Hill, Thermally rearranged (TR) polymer membranes for CO2 separation, J. Memb. Sci. 359 (2010) 11–24. https://www.sciencedirect.com/science/article/pii/S0376738809006942?via%3Dihub (accessed September 12, 2019).

[95]   N.B. McKeown, Polymers of Intrinsic Microporosity (PIMs), Polymer (Guildf). 202 (2020) 122736. https://doi.org/10.1016/j.polymer.2020.122736.

[96]   H.A. Mannan, H. Mukhtar, T. Murugesan, R. Nasir, D.F. Mohshim, A. Mushtaq, Recent Applications of Polymer Blends in Gas Separation Membranes, Chem. Eng. Technol. 36 (2013) 1838–1846. https://doi.org/10.1002/ceat.201300342.

[97]   L.M. Robeson, Polymer Blends in Membrane Transport Processes, Ind. Eng. Chem. Res. 49 (2010) 11859–11865. https://doi.org/10.1021/ie100153q.

[98]   R. Mahajan, W.J. Koros, Factors Controlling Successful Formation of Mixed-Matrix Gas Separation Materials, Ndustrial Eng. Chem. Res. 39 (2000) 2692–2696. https://doi.org/10.1021/ie990799r.

[99]   S.A. Hashemifard, A.F. Ismail, T. Matsuura, A new theoretical gas permeability model using resistance modeling for mixed matrix membrane systems, J. Memb. Sci. 350 (2010) 259–268. https://doi.org/10.1016/j.memsci.2009.12.036.

[100] B. Shimekit, H. Mukhtar, T. Murugesan, Prediction of the relative permeability of gases in mixed matrix membranes, J. Memb. Sci. 373 (2011) 152–159. https://doi.org/10.1016/j.memsci.2011.02.038.

[101] T.-S. Chung, L.Y. Jiang, Y. Li, S. Kulprathipanja, Mixed matrix membranes (MMMs) comprising organic polymers with dispersed inorganic fillers for gas separation, Prog. Polym. Sci. 32 (2007) 483–507. https://doi.org/10.1016/j.progpolymsci.2007.01.008.

[102] T.T. Moore, W.J. Koros, Non-ideal effects in organic-inorganic materials for gas separation membranes, J. Mol. Struct. 739 (2005) 87–98. https://doi.org/10.1016/j.molstruc.2004.05.043.

[103] E. Esposito, I. Mazzei, M. Monteleone, A. Fuoco, M. Carta, N. McKeown, R. Malpass-Evans, J.C. Jansen, Highly Permeable Matrimid®/PIM-EA(H2)-TB Blend Membrane for Gas Separation, Polymers (Basel). 11 (2018) 46. https://doi.org/10.3390/polym11010046.

[104] W.F. Yong, F.Y. Li, Y.C. Xiao, P. Li, K.P. Pramoda, Y.W. Tong, T.S. Chung, Molecular engineering of PIM-1/Matrimid blend membranes for gas separation, J. Memb. Sci. 407–408 (2012) 47–57. https://doi.org/10.1016/j.memsci.2012.03.038.

[105] W.F. Yong, F.Y. Li, Y.C. Xiao, T.S. Chung, Y.W. Tong, High performance PIM-1/Matrimid hollow fiber membranes for CO2/CH4, O2/N2 and CO2/N2 separation, J. Memb. Sci. 443 (2013) 156–169. https://doi.org/10.1016/j.memsci.2013.04.037.

[106] M.L. Jue, V. Breedveld, R.P. Lively, Defect-free PIM-1 hollow fiber membranes, J. Memb. Sci. 530 (2017) 33–41. https://doi.org/10.1016/j.memsci.2017.02.012.

[107] R. Swaidan, B.S. Ghanem, E. Litwiller, I. Pinnau, Pure- and mixed-gas CO2/CH4 separation properties of PIM-1 and an amidoxime-functionalized PIM-1, J. Memb. Sci. 457 (2014) 95–102. https://doi.org/https://doi.org/10.1016/j.memsci.2014.01.055.

[108] H.A. Patel, C.T. Yavuz, Noninvasive functionalization of polymers of intrinsic microporosity for enhanced CO2 capture, Chem. Commun. 48 (2012) 9989–9991. https://doi.org/10.1039/C2CC35392J.

[109] D. Nikolaeva, I. Azcune, E. Sheridan, M. Sandru, A. Genua, M. Tanczyk, M. Jaschik, K. Warmuzinski, J.C. Jansen, I.F.J. Vankelecom, Poly(vinylbenzyl chloride)-based poly(ionic liquids) as membranes for CO2 capture from flue gas, J. Mater. Chem. A. 5 (2017) 19808–19818. https://doi.org/10.1039/C7TA05171A.

[110] J.M.S. Henis, M.K. Tripodi, Composite hollow fiber membranes for gas separation: the resistance model approach, J. Memb. Sci. 8 (1981) 233–246. https://doi.org/10.1016/S0376-7388(00)82312-1.

[111] S. Keskin, S.A. Alsoy Altinkaya, A Review on Computational Modeling Tools for MOF-Based Mixed Matrix Membranes, Computation. 7 (2019) 36. https://doi.org/10.3390/computation7030036.

[112] I.N. Beckman, V.V. Teplyakov, Selective gas transfer through binary polymeric systems based on block-copolymers, Adv. Colloid Interface Sci. 222 (2015) 70–78. https://doi.org/10.1016/j.cis.2014.10.004.

[113] F. Weigelt, P. Georgopanos, S. Shishatskiy, V. Filiz, T. Brinkmann, V. Abetz, Development and

Characterization of Defect-Free Matrimid® Mixed-Matrix Membranes Containing Activated Carbon Particles for Gas Separation, Polymers (Basel). 10 (2018) 51. https://doi.org/10.3390/polym10010051.

[114] S. Yi, B. Ghanem, Y. Liu, I. Pinnau, W.J. Koros, Ultraselective glassy polymer membranes with unprecedented performance for energy-efficient sour gas separation, Sci. Adv. 5 (2019) eaaw5459. https://doi.org/10.1126/sciadv.aaw5459.

[115] J.W. Barnett, C.R. Bilchak, Y. Wang, B.C. Benicewicz, L.A. Murdock, T. Bereau, S.K. Kumar, Designing exceptional gas-separation polymer membranes using machine learning, Sci. Adv. 6 (2020) eaaz4301. https://doi.org/10.1126/sciadv.aaz4301.

[116] A.Y. Alentiev, K.A. Loza, Y.P. Yampolskii, Development of the methods for prediction of gas permeation parameters of glassy polymers: polyimides as alternating co-polymers, J. Memb. Sci. 167 (2000) 91–106. https://doi.org/10.1016/S0376-7388(99)00271-9.

[117] Y. Yampolskii, S. Shishatskii, A. Alentiev, K. Loza, Group contribution method for transport property predictions of glassy polymers: focus on polyimides and polynorbornenes, J. Memb. Sci. 149 (1998) 203–220. https://doi.org/10.1016/S0376-7388(98)00152-5.

[118] Y. Yampolskii, S. Shishatskii, A. Alentiev, K. Loza, Correlations with and prediction of activation energies of gas permeation and diffusion in glassy polymers, J. Memb. Sci. 148 (1998) 59–69. https://doi.org/https://doi.org/10.1016/S0376-7388(98)00130-6.

[119] A. Alentiev, Y. Yampolskii, Correlation of gas permeability and diffusivity with selectivity: Orientations of the clouds of the data points and the effects of temperature, Ind. Eng. Chem. Res. 52 (2013) 8864–8874. https://doi.org/10.1021/ie302680r.

[120] O. V Malykh, A.Y. Golub, V. V Teplyakov, Polymeric membrane materials: new aspects of empirical approaches to prediction of gas permeability parameters in relation to permanent gases, linear lower hydrocarbons and some toxic gases., Adv. Colloid Interface Sci. 164 (2011) 89–99. https://doi.org/10.1016/j.cis.2010.10.004.

[121] Q. Yuan, M. Longo, A.W. Thornton, N.B. McKeown, B. Comesaña-Gándara, J.C. Jansen, K.E. Jelfs, Imputation of missing gas permeability data for polymer membranes using machine learning, J. Memb. Sci. 627 (2021) 119207. https://doi.org/10.1016/j.memsci.2021.119207.

[122] S. van Buuren, K. Groothuis-Oudshoorn, mice: Multivariate imputation by chained equations in R, J. Stat. Softw. (2010) 1–68.

[123] D.J.C. MacKay, Bayesian interpolation, Neural Comput. 4 (1992) 415–447.

[124] P. Geurts, D. Ernst, L. Wehenkel, Extremely randomized trees, Mach. Learn. 63 (2006) 3–42. https://doi.org/10.1007/s10994-006-6226-1.

[125] F. Pedregosa, G. Varoquaux, A. Gramfort, V. Michel, B. Thirion, O. Grisel, M. Blondel, P. Prettenhofer, R. Weiss, V. Dubourg, J. Vanderplas, A. Passos, D. Cournapeau, M. Brucher, M. Perrot, E. Duchesnay,

Scikit-learn: Machine Learning in Python, J. Mach. Learn. Res. 12 (2011) 2825–2830.

[126] Z. Wang, Q. Shen, J. Liang, Y. Zhang, J. Jin, Adamantane-grafted polymer of intrinsic microporosity with finely tuned interchain spacing for improved CO2 separation performance, Sep. Purif. Technol. 233 (2020) 116008. https://doi.org/10.1016/j.seppur.2019.116008.

[127] S.-L. Li, Z. Zhu, J. Li, Y. Hu, X. Ma, Synthesis and gas separation properties of OH-functionalized Tröger's base-based PIMs derived from 1,1'-binaphthalene-2,2'-OH, Polymer (Guildf). 193 (2020) 122369. https://doi.org/https://doi.org/10.1016/j.polymer.2020.122369.

[128] T. Li, J. Liu, S. Zhao, Z. Chen, H. Huang, R. Guo, Y. Chen, Microporous polyimides containing bulky tetra-o-isopropyl and naphthalene groups for gas separation membranes, J. Memb. Sci. 585 (2019) 282–288. https://doi.org/10.1016/j.memsci.2019.05.003.

[129] A.A. Kuznetsov, A.Y. Tsegelskaya, A.M. Orlova, N.A. Belov, S. V. Chirkov, R.Y. Nikiforov, A.Y. Alentiev, Polyimides Based on the Diethyltoluenediamine Isomer Mixture: Synthesis and Gas Transport Properties, Membr. Membr. Technol. 1 (2019) 316–322. https://doi.org/10.1134/s2517751619050044.

[130] C. Ma, J.J. Urban, Hydrogen-Bonded Polyimide/Metal-Organic Framework Hybrid Membranes for Ultrafast Separations of Multiple Gas Pairs, Adv. Funct. Mater. 29 (2019) 1–9. https://doi.org/10.1002/adfm.201903243.

[131] S. Wang, S. Ma, H. He, W. Ai, D. Wang, X. Zhao, C. Chen, Aromatic polyimides containing pyridine and spirocyclic units: Preparation, thermal and gas separation properties, Polymer (Guildf). 168 (2019) 199–208. https://doi.org/10.1016/j.polymer.2019.02.046.

[132] X. Hu, W.H. Lee, J. Zhao, J.Y. Bae, J.S. Kim, Z. Wang, J. Yan, Y. Zhuang, Y.M. Lee, Tröger's Base (TB)-containing polyimide membranes derived from bio-based dianhydrides for gas separations, J. Memb. Sci. (2020) 118255. https://doi.org/https://doi.org/10.1016/j.memsci.2020.118255.

[133] Y. Fan, H. Yu, S. Xu, Q. Shen, H. Ye, N. Li, Zn(II)-modified imidazole containing polyimide/ZIF-8 mixed matrix membranes for gas separations, J. Memb. Sci. 597 (2020) 117775. https://doi.org/10.1016/j.memsci.2019.117775.

[134] S. Velioğlu, S.B. Tantekin-Ersolmaz, J.W. Chew, Towards the generalization of membrane structure-property relationship of polyimides and copolyimides: A group contribution study, J. Memb. Sci. 543 (2017) 233–254. https://doi.org/10.1016/j.memsci.2017.08.042.

[135] M. Longo, B. Comesana-Gandara, M. Monteleone, E. Esposito, A. Fuoco, L. GIORNO, N.B. McKeown, J.C. Jansen, Matrimid®5218/AO-PIM-1 Blend Membranes for Gas Separation, J. Membr. Sci. Res. 0 (2021). https://doi.org/10.22079/JMSR.2021.540493.1504.

[136] Q. Yuan, M. Longo, A. Thornton, N.B. McKeown, B. Comesana-Gandara, J.C. Jansen, K. Jelfs, Imputation of Missing Gas Permeability Data for Polymer Membranes using Machine Learning,

ChemRxiv. (2020). https://doi.org/10.26434/chemrxiv.13124993.v1.

Acknowledgements

Annex: Publications and Presentations

Publications leading to this thesis

1. Fuoco, B. Comesaña-Gándara, **M. Longo**, E. Esposito, M. Monteleone, I. Rose, C. G. Bezzu, M. Carta, N.B. McKeown, J.C. Jansen. *Temperature dependence of gas permeation and diffusion in triptycene-based ultrapermeable polymers of intrinsic microporosity* ACS Applied Materials & Interfaces 2018, 10 (42),36475-36482. DOI: 10.1021/acsami.8b13634

2. **M. Longo**, M.P. De Santo, E. Esposito, A. Fuoco, M. Monteleone, L. Giorno, J. C. Jansen, *Force spectroscopy determination of young's modulus in mixed matrix membranes*, Polymer (Guildf). 2018, 156, 22–29. DOI: 10.1016/j.polymer.2018.09.043

3. **M. Longo**, M. P. De Santo, E. Esposito, A. Fuoco, M. Monteleone, L. Giorno, B. Comesaña-Gándara, J. Chen, G. Bezzu, M. Carta, I. Rose, N. McKeown, J. C. Jansen; *Correlating gas permeability and rigidity during the physical aging of polymers of intrinsic microporosity using atomic force microscopy*, Industrial & Engineering Chemistry Research, 2019. DOI:10.1021/acs.iecr.9b04881

4. Q. Yuan, **M. Longo**, A.W. Thornton, N.B. McKeown, B. Comesaña-Gándara, J.C. Jansen, K.E. Jelfs, Imputation of missing gas permeability data for polymer membranes using machine learning, J. Memb. Sci. 627 (2021) 119207. doi:10.1016/j.memsci.2021.119207. (Preprint from ChemRxiv, 22 Oct 2020. DOI: 10.26434/chemrxiv.13124993.v1)

5. **M. Longo**, B. Comesaña-Gándara, M. Monteleone, E. Esposito, A. Fuoco, L. Giorno, N.B. McKeown, J.C. Jansen, Matrimid®5218/AO-PIM-1 Blend Membranes for Gas Separation, J. Membr. Sci. Res., *in press*. https://doi.org/10.22079/JMSR.2021.540493.1504

Presentations leading to this thesis

1. **M. Longo**, M. P. De Santo, E. Esposito, A. Fuoco, M. Monteleone, L. Giorno, J. C. Jansen, *Analysis of the mechanical properties of polymeric membranes by AFM and tensile tests* Macrogiovani 2018 – Associazione Italiana Macromolecole – Salerno 14-15/06/2018;

2. **M. Longo**, M.P. De Santo, E. Esposito, A. Fuoco, M. Monteleone, L. Giorno, J.C. Jansen*, Force spectroscopy determination of Young's modulus in mixed matrix membranes and PIMs*, ITM Seminar days, 19-20 December 2018;

3. **M. Longo**, *Membrane Technology for gas separation*, Meeting of Former UNICAL Students, 19 December 2019.

4. **M. Longo**, M. P. De Santo, E. Esposito, A. Fuoco, M. Monteleone, L. Giorno, B. Comesaña-Gandara, J. Chen, C. G. Bezzu, M. Carta, N.B. McKeown, J. C. Jansen, *Correlating Gas Permeability and Young's Modulus during the Physical Aging of PIMs*, ICOM2020, 07-12 December 2020

5. **M. Longo**, M. Monteleone, E. Esposito, A. Fuoco, L. Giorno, J. C. Jansen, *Matrimid®5218/AO-PIM-1 blend membranes for gas separation, ITM SEMINARDAY 2021,* 21 December 2021

Co-authored other publications

1. A. Iulianelli, J.C. Jansen, E. Esposito, **M. Longo**, F. Dalena, A. Basile, *Hydrogen permeation and separation characteristics of a thin Pd-Au/Al2O3 membrane: The effect of the intermediate layer absence*, Catalysis Today, 2019, 330, 32-38. DOI: 10.1016/j.cattod.2018.04.029

2. A. Fuoco, B. Satilmis, T. Uyar, M. Monteleone, E. Esposito, C. Muzzi, E. Tocci, **M. Longo**, M. P. De Santo, M. Lanč, K. Friess, O. Vopicka, P. Izak, J. C. Jansen; *Comparison of pure and mixed gas permeation of the highly fluorinated polymer of intrinsic microporosity PIM-2 under dry and humid conditions: experiment and modelling*, Journal of Membrane Science, 2020, 594, 117460. DOI:10.1016/j.memsci.2019.117460

3. C.G. Bezzu, E. Esposito, A. Fuoco, **M. Longo**, M. Monteleone, J.C. Jansen, N.B. McKeown, *Ultrapermeable polymers of intrinsic microporosity (PIMs) containing spirocyclic units with fused triptycenes*, in preparation.

Co-authored other presentations

1. Alessio Fuoco*, B. Comesaña-Gándara, **M. Longo**, E. Esposito, M. Monteleone, I. Rose, C. G. Bezzu, M. Carta, N.B. McKeown, J.C. Jansen *Gas transport analysis in the ultrapermeable polymer of intrinsic microporosity*, PIM-TMN-Trip. Euromembrane 2018 Valencia, Spain, 9-13 July 2018.